KINEMATICS OF MASSIVE STAR FORMATION

THE GAS KINEMATICS OF HIGH MASS STAR FORMING REGIONS.

By

PAMELA D. KLAASSEN, B.Sc.,M.Sc.

A Thesis
Submitted to the School of Graduate Studies
in Partial Fulfillment of the Requirements
for the Degree
Doctor of Philosophy

McMaster University

DOCTOR OF PHILOSOPHY (2008) McMaster University
(Astrophysics) Hamilton, Ontario

TITLE: The Gas Kinematics of High Mass Star Forming Regions.

AUTHOR: Pamela D. Klaassen, B.Sc.,M.Sc.(University of Calgary)

SUPERVISOR: Dr. C. D. Wilson

NUMBER OF PAGES: xiv, 144

Abstract

The mechanism by which massive stars form is not nearly as well understood as it is for lower mass stars. For instance, at the onset of massive star formation, it is still not clear whether the mass for a given massive star comes from the turbulent collapse of a dense core (i.e McKee & Tan, 2003) or whether the star continues to accrete material from the cores environment as it grows (i.e. Bonnell et al., 1998). From this point, it is suggested that the cold, massive core (an Infrared Dar Cloud) begins to heat up and form a Hot Core. Later in its protostellar evolution, an HII region forms from the ionizing radiation being produced by the massive star. How, or even whether, accretion onto the massive protostar can continue in the presence of the large outward thermal and radiation pressures from the star is also quite uncertain. Can the star continue to accrete ionized gas (i.e. Keto & Wood, 2006)? Are the accretion rates high enough early on to account for the final observed masses (i.e. Klaassen et al., 2006)? Or, is there some way of minimizing the radiation pressure affecting the infalling gas (i.e. McKee & Ostriker, 2007, and references therein).

Here, we present observations which suggest that there is a statistically significant, although short, period in which rotation and infall of molecular gas (which powers a bipolar outflow) continue after the formation of an HII region. This continued infall of material is seen on both large and small scales, and appears to be continuing to produce outflows in many of the sources observed in this study. That it is not seen in all sources suggests that this stage is short lived.

Preface

Chapters 2 - 5 of this thesis reflect original work completed primarily by P. Klaassen. I either am, or will be, first author on each of the four papers included here (as shown in bold text at the beginning of each chapter).

Chapters 2 and 3 were completed in consultation with my supervisor, Dr. Christine Wilson. The original ideas for these papers were mine, I was the principal investigator for the James Clerk Maxwell Telescope (JCMT) observing proposals, and went to the telescope to make the observations (accompanied once by Dr. Wilson). I did the data reduction and analysis in consultation with Dr. Wilson, and I wrote the papers and she edited drafts before and after submission to the Astrophysical Journal.

Chapters 4 and 5 were completed primarily in consultation with my thesis supervisor, Dr. Christine Wilson, as well as in consultation with my Smithsonian Astrophysical Observatory Pre-Doctoral Fellowship supervisor, Dr. Eric Keto and another Astrophysicist at the Harvard-Smithsonian Center for Astrophysics, Dr. Qizhou Zhang. Dr. Keto was the principal investigator for the Submillimeter Array (SMA) observing proposal (discussed in both chapters), and I was the principal investigator for the JCMT proposal (discussed in chapter 5). Drs. Keto and Zhang were primarily interested in the radio recombination line observed at the SMA, and I was given permission to use the rest of the data that was simultaneously observed by the SMA. I completed the molecular line, and continuum emission data reduction and analysis of these datasets in frequent consultation with Drs. Wilson, Keto and Zhang. I have written the paper drafts presented here. Dr. Wilson has edited a few drafts and Drs. Keto and Zhang have edited one draft.

Acknowledgements

No thesis should ever be completed in isolation, and mine certainly wasn't.

To my supervisor, Christine Wilson. To this day, you still manage to surprise and impress me with your knowledge, skills, wit, and amazing support. To my 'sabbatical supervisor' Eric Keto, for showing me the ropes, and trying to keep me on course. I would also like to thank Qizhou Zhang, who always made time for me. Special thanks also go to Mike Fich, Doug Johnstone, Phil Myers, and Ralph Pudritz for their guidance along the way.

To the physics office staff - Tina, Cheryl, Rose, Mara, Liz and Daphne. Because you're awesome, and I know you're reading this.

To my friends, for sticking with me, and trying to keep me somewhat sane - you may have failed, but it's the attempt that matters. Adam "Housemate" Raegan, Ali "Newspaper" Abel, Alison "Pam's bum is wet" Peck, Alyssa "Weekend in New York" Moldowan, Becky "Petsmart" Larson, Bonnie "Snorkel Buddy" Larson, Brad "Stars are Bright" Warren, Charles-Philippe "Weil's Bakery" Lajoie, Dave "Programming" Cooke, Elaine "Fat on the Inside" Winston, Emma "Pepsi Run" Spanswick, Kristin "Amarter than Pam" Woodley, Laura "We're facebook Friends" Parker, Lindsay "Farce of the Penguins" Oaster (and Zach), Marie-Josee "Don't mess with MJ" Colbert (and Nadi), Mike "Because he's Nice and you're Pam" Reid (and Clayton), Nathan "Pink Office" Leigh, Nicholas "Take Everything Off" Petitclerc, Paula "Holland vs. Portugal" Teixeira, Rene "I Need to Pick your Grad Students" Plume, Rob "Pain in the Arse" Cockcroft, Rob "You'll Like This Cheese" Gutermuth, Sijing "(Insert Raspberry Noise Here)" Shen, Steve "Swing Dance" Bickerton, and the CfA Poets. Thank you all for believing in me, and for being there when I wanted or needed you.

To my family, for loving me, believing in me, and even packing me up, and helping me get to wherever this adventure has taken me. For late night chats, spa trips or just a bike ride. And for thinking that I'm smart - even if that only lasts until the age of seven. Thank you for being there, I love you.

Contents

List of Figures

List of Tables

Chapter 1

Introduction

It has only been within the last 100 years that we have determined how, and why, stars shine. Understanding the processes of stellar nucleo-synthesis has since led to greater insights into such fundamental concepts as the origins of the heavy elements, and why we can use Type Ia supernovae as distance markers to gage the size of the visible universe.

The one single parameter that best describes what will happen during the main sequence and post-main sequence lifetime of a star is its mass. Through an understanding of the life cycle of stars, astronomers have shown that stellar lifetimes are limited, and that the more massive a star is, the shorter its lifetime. Gravitational pressure from the outer layers of a star dictates how much nucleo-synthesis must and can happen during a stellar lifetime in order to keep a star stable against collapse. For more massive stars, there is more gravitational pressure pushing in on the core, forcing the star to fuse hydrogen atoms together more frequently, raising the thermal pressure within the core, to balance gravity. In this manner, more massive stars burn through their mass much more quickly than lower mass stars. While stars like the Sun will live for approximately ten billion years, stars 15 times more massive will only live for approximately ten million years (Iben, 1967).

Results from experiments such as WMAP show that the universe is 13.7 billion years old (Spergel et al., 2007). It is old enough that stars like the Sun would have burned through their nuclear material already had they formed during the Big Bang. Yet, we still see stars with masses in excess of 60 solar masses ($M_{\odot}$). These observations require that the process of star formation has been ongoing through cosmic history.

The interstellar medium (ISM) is a large reservoir of material from which stars can build up enough mass to begin burning hydrogen in their cores. However, the conditions in much of the ISM are not conducive to the formation of stars. In order for a fragment of the ISM to shrink to a size scale on which gravity can begin to play an important role, it must lose much of its

thermal support. Rotational transitions of molecules are an excellent cooling mechanism in the ISM (Tielens, 2005, Section 2.6.2). In a diffuse atomic gas cloud, however, the pervasive high energy (far ultraviolet) photons present in the interstellar radiation field (ISRF) act to dissociate molecules (such as H_2, the most abundant molecule in the ISM) at a faster rate than they can be produced. If H_2 is allowed to build up, it can begin to self shield at column densities of $\sim 10^{14}$ cm^{-2} (Tielens, 2005, Section 8.7.1).

Once H_2 begins self shielding, the various atomic species present in the cloud can begin forming simple molecules (like H_2 or CO), which are no longer photodissociated by the ISRF at a significant rate. At this point, the gas cloud can begin to cool very efficiently. The transition from an atomic gas cloud to a molecular one is not very well understood; however, there is evidence to suggest that what appear to be cold atomic gas clouds with little or no molecular emission are such transition clouds and are already primarily molecular (Goldsmith et al., 2007; Klaassen et al., 2005).

Once molecules are formed more often than they are dissociated, a molecular cloud contains an efficient cooling mechanism, and much of the thermal support for these clouds is radiated away. This 'phase' of the ISM must still remain in pressure equilibrium with the rest of the interstellar medium for it not to dissipate due to pressure gradients. Thus, as the temperature of the cloud decreases, the density increases (Field et al., 1969). It is in the coldest, densest regions of these molecular clouds (often called Giant Molecular Clouds due to their sizes) that stars form.

Giant Molecular Clouds (GMCs) are cold dusty places, where photons at visible wavelengths are rare, and most thermal photons are emitted in the radio, millimeter, and sub-millimeter wavelength ranges. This makes radio, millimeter and sub-millimeter telescopes the perfect instruments for studying the interstellar medium and the processes involved in the formation of stars. As the technologies involved in long wavelength astronomy have evolved, so has our understanding of the ISM and the processes involved in forming stars out of it.

In the late 1960's and early 1970's, models for the collapse of an over-density of material in a GMC were being created (i.e. Penston, 1969; Larson, 1972). Up until about 20 years ago, however, the processes involved in forming stars like the Sun were not very well constrained. Since that time, an evolutionary sequence showing the progression from a cold over density of molecular gas in the interstellar medium (ISM) to a core hydrogen burning (main sequence) star has developed (i.e. Shu et al., 1987; Andre et al., 1993). For reasons discussed later, the same cannot quite yet be said for the formation of more massive stars.

Below, we describe how we can observe the ISM using radio astronomy (Section 1.1) as well as the techniques involved in obtaining high resolution

observations using interferometers. We then describe the processes involved in star formation (Section 1.2), focusing on the formation of low mass stars (i.e. stars like the Sun) in Section 1.2.2 and the formation of high mass stars in Section 1.2.3. We conclude this Chapter with an outline of the following chapters and how they attempt to address the still poorly constrained formation mechanisms of massive stars (Section 1.3).

1.1 Radio Astronomy

Analogously to photometry (employing CCD cameras) and spectrometry (employing spectrographs) used in optical astronomy to observe stars and gas, in radio astronomy we can observe both continuum (using bolometers) and spectral line (using spectrometers) emission from the cold dust and gas in the interstellar medium.

In general, bodies have a characteristic temperature, and according to Wien's law ($T = 2.898(\text{mm K})/\lambda$), given the temperature of the peak of the black-body emission of an object, we can determine the wavelength at which it emits the most radiation. For the cold objects in the ISM, this characteristic temperature is of order 30 K, resulting in a characteristic wavelength of 100 μm. For comparison, at 37°C (310 K), the human body has a characteristic wavelength of 9 μm, which corresponds to infrared (IR) wavelengths, and is the reason why people glow in night vision (IR) goggles.

This characteristic wavelength is not the only wavelength at which a body emits radiation, and on both the high and low energy sides of this wavelength, the body also emits, but at lower intensities. The intensity emitted by a body of a given characteristic temperature at a given wavelength can be described using the Planck black body function:

$$B(\nu, T) = \frac{2hc^2}{\nu^3} \frac{1}{e^{h\nu/kT} - 1} \tag{1.1}$$

where $B(\nu, T)$ is the intensity at a given frequency (ν) and temperature (T), h is Planck's constant, c is the speed of light, and k is the Boltzmann constant. By using bolometers to observe the intensity of the emission (i.e. its flux) of a body at a few different wavelengths, we can determine the slope of the emission as a function of wavelength (or frequency), and from that determine the peak of the Planck black body function, or Spectral Energy Distribution (SED).

As described further in Section 4.3.3, we can also use the intensity of the emission at a single frequency (assuming a characteristic temperature, and a single emission process, such as optically thin thermal dust emission) to estimate *how much* material is producing that emission.

This type of observation is known as a continuum observation (since we are observing a portion of a continuum of emission from the specific object being studied), and is quite useful for constraining the dust mass and/or temperature of a region. However, this type of observation cannot be used to describe the kinematics of the gas in the interstellar medium (see, for instance Section 1.2.1). In order to complement continuum observations with the kinematics of the gas in the interstellar medium, we require spectral line observations of the same regions.

For molecular species, within each electronic state, there are much lower energy vibrational and rotational transitions. Using the Born-Oppenheimer approximation, we can separate the components of the electronic, vibrational and rotational transitions of a molecule (See, for instance, Rholfs & Wilson, 2004). The energies required for the electronic transitions correspond to optical and ultraviolet wavelengths, and those required for the vibrational transitions exist in the IR. In the later stages of massive star formation, it is not uncommon to see emission nebulae associated with star formation in an atomic electronic transition (Hα). The low energies present in the cold regions in which stars form are, however, unfavorable for electronic transitions. Rotational transitions of molecules occur at millimeter and submillimeter wavelengths, and the energies required to excite molecules into higher rotational states *do* exist within the cold cores of GMCs. These transitions are observable with spectrometers on millimeter and submillimeter telescopes assuming they fall within a transparent atmospheric window, or are observed from space.

Rotational transitions of molecules occur at specific wavelengths. The frequency of a rotational transition of a linear molecule (i.e. CO, SiO or HCO^+) can be determined using $\nu = 2B_e(J_{\rm up}+1)$, where B_e is the rotational constant for that molecule[1], and $J_{\rm up}$ is the upper level of the transition. For example, the J=2-1 transition of CO occurs at 230.538 GHz.

Spectral lines, while centered at their calculated frequencies, are inherently not delta functions at that frequency. A number of processes are responsible for broadening these lines, the smallest of which are natural broadening and thermal broadening. Natural broadening is due to the inherent uncertainty in the energy of a state that is occupied for a period of time (Heisenberg Uncertainty), and broadens a line by $\Delta\nu_{\rm nat} \propto A_{u\ell}/4\pi$ where $A_{u\ell}$ is the Einstein A coefficient for a given transition and is a measure of the spontaneous emission probability from that level (see for instance Dyson & Williams, 1997). Thermal broadening is due to the random thermal motions of the gas within an emitting region. This broadening Doppler shifts the emitting photons, and a thermal distribution of emission line frequencies results. Thermal broadening takes the form:

[1]Rotation constants can be found online on websites such as http://spec.jpl.nasa.gov/

$$\Delta\nu_{\rm therm} = \frac{\nu}{c}\sqrt{\frac{2kT}{m}\ln 2} \tag{1.2}$$

where k is the Boltzmann constant, T is the ambient temperature, and m is the mass of the molecule (Townes & Schawlow, 1975).

In general, radio astronomers do not discuss these frequency shifts in terms of frequency offsets from the expected line frequency, but in terms of velocity offsets, since

$$\frac{\Delta\nu}{\nu} = \frac{\Delta V}{c} \tag{1.3}$$

where ν is the rest frequency of the line, V is the velocity of the gas ($V \ll c$), and c is the speed of light, and positive velocity offsets correspond to lowering the frequency or increasing the wavelength of the emission (redshifting). Spectral line profiles are generally shown as a function of velocity instead of frequency since this method directly gives information about the kinematics of the gas - how fast it is moving with respect to the ambient gas. Because of the differential rotation of the Galaxy, gas in different parts of the Galaxy will generally be in motion with respect to the Sun, and the observed frequency of a line becomes red or blue shifted from the emission frequency by calculable amount. The velocity of the observed body with respect to the average velocity of objects in the Solar neighborhood[2] is generally known as the "local standard of rest" velocity, and expressed as $V_{\rm LSR}$.

In addition to the thermal motions of the gas, there is usually significant non-thermal motion of the gas in a star forming region as well. These motions include, but are not limited to, turbulent motions of the gas, separation of ionic and neutral species via ambi-polar diffusion along magnetic field lines, and bulk flows such as infall, outflow and rotation in the gas. These later processes (bulk flows) are described further in Section 1.2.1. While velocity shifts in the gas are inherently three dimensional, in our observed spectra we can only distinguish Doppler shifts in the line of sight component of the velocity. Shifts in the two orthogonal directions in the plane of the sky do not translate into velocity shifts in the spectra. In order for bulk motions to be observable, some component of the motion must be along the line of sight.

Critical to observing the kinematics of the gas in the ISM is being able to see structures at high enough resolution to see changes in the spectral line profiles from position to position. Below, we describe how we can observe at high spatial resolution at long wavelengths.

The James Clerk Maxwell Telescope (JCMT) can observe both line and continuum emission around 345 and 230 GHz, and with a diameter of 15 m,

[2]Note that the Sun has a peculiar velocity with respect to the local standard of rest velocity of approximately 20 km s^{-1} (Jaschek & Valbousquet, 1993).

achieves resolutions of 14″ and 20″ (respectively). The JCMT is the largest single dish submillimeter telescope, and in order to obtain higher resolution observations at these wavelengths, we have to resort to interferometry.

1.1.1 Interferometry

The best resolution possible with a telescope observing at any wavelength is proportional to both the diameter of the telescope's aperture, and the wavelength of light being observed: $\theta \propto \lambda/D$, where θ is the resolution of the telescope, λ is the wavelength of light being observed, and D is the diameter of the telescope. This assumes no blurring from the atmosphere or other processes along the optical path. Because optical light has wavelengths of order 600 nm, in order to reach sub-arcsecond resolution, telescopes need to be of order 1 m across. Submillimeter light has wavelengths of order 1 mm, and so, to achieve the same resolution, a submillimeter telescope must be of order 2 km across. Building and maintaining a single antenna of this size is prohibitively expensive and it would be extremely hard to ensure sufficient surface accuracy on an antenna of this size (the surface accuracy[3] of the JCMT, for instance, is $\sim 33\mu$m).

Radio interferometers employ a number of individual antennae at very precisely known positions. The separation between any two antennae is known as a 'baseline'. Each antenna points towards a location known as the 'pointing center', which is the position on the sky along the direction s_o in Figure 1.1. Structures within the primary beam of the telescope (the size of which is determined by the size of the individual antennae) are then measured with respect to the pointing center via changes in the u and v components of the baseline vector (see Figure 1.1). Using a Fourier transform, the 'visibilities' in the uv plane are translated to intensities within each synthesized beam (of solid angle $d\Omega$) at positions defined by the vector σ from the pointing center (Thompson et al., 1986; Rholfs & Wilson, 2004). The primary beam of this type of observation is the field of view of the observations, while the synthesized beam is the resolution element within the primary beam.

The largest of these baselines sets the small scale resolution limit of an interferometer. Physically, there are limits to how closely the individual antennae of an interferometer can be placed. This shortest baseline effectively sets the largest scale structures to which the interferometer is sensitive (as described later in Chapters 4 and 5). This means that the center of the uv plane cannot be filled in by an interferometer alone.

[3]This value was obtained at www.jach.hawaii.edu/JCMT/telescope/surface

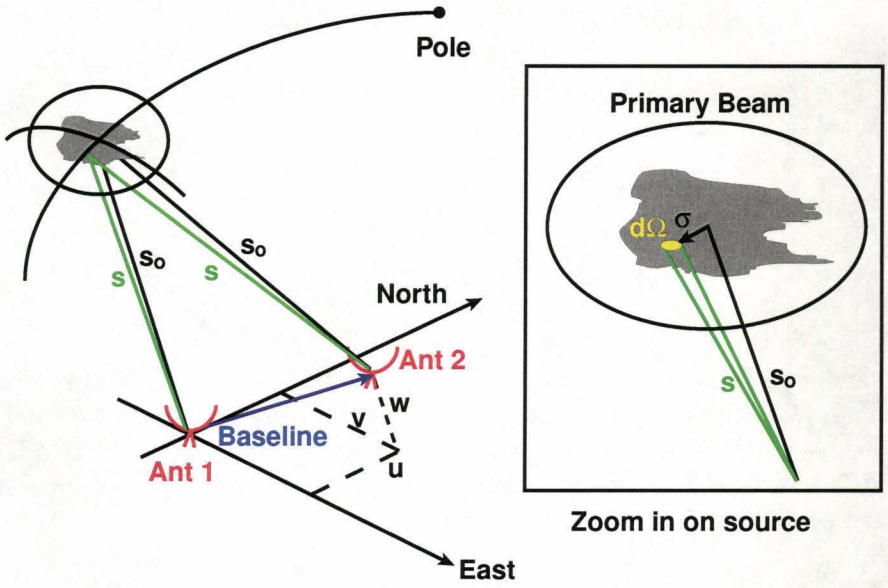

Figure 1.1: A two element interferometer pointing at a source centered at a position along the vector s_o. This point marks the center of the observable field (phase center), and all points within the primary beam of the observations (shown as a circle around the source) are observed as offsets from the phase center (using the vector σ as shown in the right hand panel). Differences in the u and v components of the baseline (projected distance of the two antennae) between the phase center and the position along the vector s are measured by the interferometer. The intensity at each point in this uv plane is then recorded as a 'visibility'. These uv plane visibilities are then Fourier transformed into intensities along the position vector σ. Small displacements in the uv plane correspond to large scale displacements in the observed plane. Multiple antenna result in better simultaneous coverage of the uv plane. Figure modified from Thompson et al. (1986).

1.2 Star Formation

When studies of the mass distribution of stars in a given stellar cluster or galaxy as a whole are conducted, the same scaling relation is found universally. The Initial Mass Function (IMF) shows that the most common stellar mass is approximately 0.3 $M_{\odot}$ (Kroupa, 2001), and that the more massive stars form very rarely. In very low mass star forming regions, individual low mass stars can form; however, in regions with enough mass to form high mass stars, they tend to form along with a large number of lower mass stars, with the mass distribution following the IMF. This does not imply that the lower mass regions do not follow the mass distribution of the IMF, only that they are unable to fully sample the high mass end of the distribution.

Because stars can be characterized by their masses, they can be broken down into three broad categories, based on their masses. Low mass stars consist of stars with masses less than $M_* \sim 2M_{\odot}$, intermediate mass stars have masses in the range of $2M_{\odot} < M_* < 8M_{\odot}$ and high mass stars are those with masses greater than $\sim 8M_{\odot}$. The first cutoff is the upper mass limit for which a star can undergo a helium flash at the end of its main sequence lifetime (Chiosi et al., 1992), and the second cutoff occurs because it is at approximately $8M_{\odot}$ that a star burns hydrogen hot enough to ionize its surroundings and form an HII (ionized hydrogen) region around itself. It is also the minimum main sequence stellar mass required for a star to undergo a core collapse supernova at the end of its lifetime (Zinnecker & Yorke, 2007).

Below, we describe the bulk gas kinematics used to observe star formation on all mass scales (infall, rotation and outflow). We then proceed to describe the processes involved in the formation of low (and intermediate) mass stars and the evolutionary sequence which they follow in order to arrive at the main sequence. We finish this section by describing the models currently suggested for the formation of massive stars, and discuss what questions still need to be addressed in this field.

1.2.1 ISM Gas Kinematics Associated with Star Formation

For much of the lifetime of a low mass protostar, and the entire period prior to core hydrogen burning of a high mass protostar, it accretes material from its dense surroundings. The highly embedded processes involved in star formation affect, and are affected by, the local environment.

In broad terms, the processes involved in low mass star formation begin when an over-density in a GMC begins to collapse due to the effects of self gravity. Due to the inherent angular momentum present in the cloud, this infalling material does not directly fall into the center, but falls onto the mid-

plane where a rotating toroid of material builds up. This rotating structure can then form a Keplerian disk, through which the infalling material can accrete onto the forming protostar.

The angular momentum ($L = mvr$) present in the material in the disk must be conserved and so, as r decreases, v must increase. The conservation of angular momentum could act to halt accretion onto the protostar at very low masses if there were no release mechanism for the angular momentum. However, high velocity bipolar outflows are observed in star forming regions of all mass scales and the high velocities with which material is ejected from the star forming region provide the release of angular momentum which allows the star formation process to continue.

The infall, rotation and outflows produced by star formation happen on scales much larger than the stellar radius, and we can resolve the kinematics of these bulk flows, and from them, deduce the properties of the forming stars, and constrain the processes involved. These bulk flows each have unique spectral line profiles, and below, we describe the physical reasons for these observable line profiles.

Early on, the collapse of a Bonner-Ebert sphere begins in the outer (i.e. outside-in collapse) regions (Larson, 1972, i.e.). As the collapse progresses, a protostar begins forming in the center, and the support of the outer layers is removed. This begins the phase of inside-out collapse (Shu, 1977, i.e.). If we consider the large scale, inside-out, collapse of a core (like that shown in Figure 1.2), there is high velocity infall closer to the central object. As the distance from the center increases, the infall velocity decreases, to the point where the gas joins the static (and cold) envelope. The highest velocity gas at the center contributes the line wing (high velocity) emission to the spectrum. Moving outwards in concentric shells, there is more gas moving at lower velocities, and thus the line intensity at velocities closer to the rest velocity are higher. The cold static envelope absorbs some of the photons at the rest velocity of the gas, which produces the dip in intensity near the rest velocity (a so called 'self-absorption' feature). The redshifted portion of this profile is not as bright as the blue shifted portion because it is on the side of the source closest to the observer, as is the portion of the cold envelope producing the observable self-absorption profile. More of the redshifted photons get absorbed by the static envelope than the further away (and radiatively decoupled) blue shifted photons.

As the source in the center of the infall region heats up, the continuum emission becomes stronger, and the absorption of material between the continuum source and the observer becomes stronger. Since the material between the observer and the bright continuum source is redshifted with respect to the observer, a blue shifted emission peak with a red shifted absorption trough is a spectral feature indicative of infall against a bright continuum source (like an

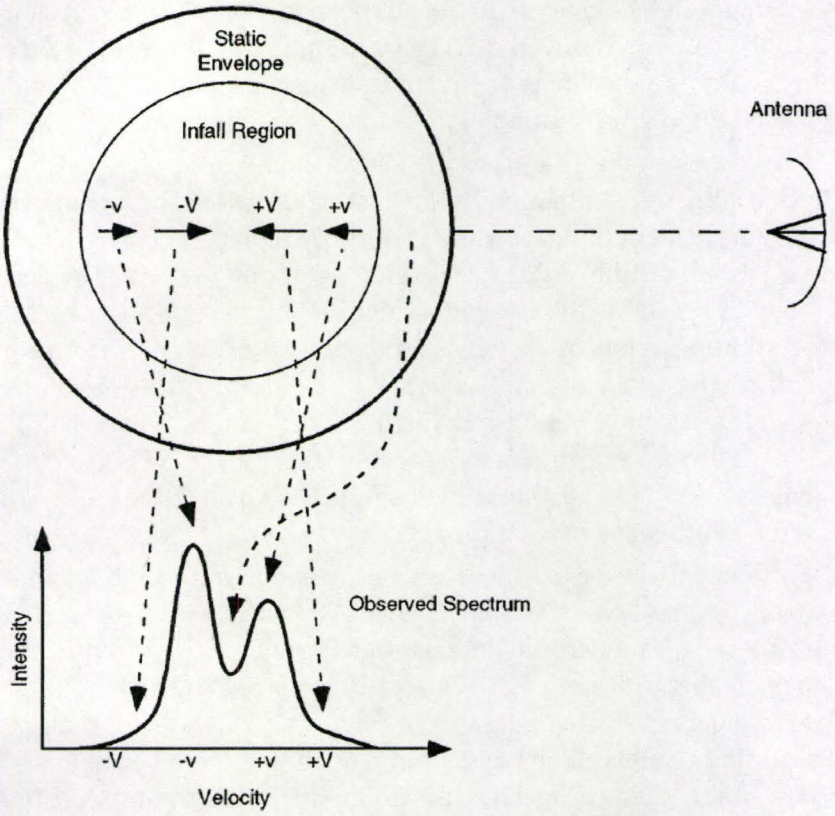

Figure 1.2: If a cloud is undergoing bulk contraction, the velocities of the different components of the gas shift along the line of sight, producing a double peaked, asymmetric line profile. In general, a double peaked profile is indicative of infall if the blue shifted (negative velocity) peak is higher (has a greater intensity) than the red shifted (positive velocity) peak. This asymmetric line profile is seen in molecular line tracers which are shielded from the central continuum source. This type of line profile is often seen in high density tracers (such as HCO^+) which can be used to trace infall (see, for instance Gregersen et al., 1997; Fuller et al., 2005). In Chapters 2 and 3 we observe this double peaked line profile in HCO^+ towards a number of high mass star forming regions. Figure reproduced from Evans (1999).

HII region). This 'inverse P-cygni profile' can be observed in both low mass (Di Francesco et al., 2001) and high mass (Rudolph et al., 1990) star forming regions.

Infall can be detected with a single spectrum on a source (regardless of whether that source is resolved). Bulk rotation of the gas on the other hand, cannot be observed in a single spectrum, and in order to detect rotation, the motion must be resolved spatially.

For a resolved source (like the one shown in Figure 1.3), the material on one side is highly redshifted, and the material on the other side is highly blueshifted since the bulk motions are primarily along the line of sight and are therefore observable. Shifting the observing position closer to the center of the source, there is less of a line of sight velocity component to the rotation, and the spectrum appears at, or very close to, the rest velocity. This gradual shift in the peak brightness across the source can be shown in a velocity weighted integrated intensity map (discussed further in Chapters 3 and 4). This type of map (also known as a first moment map) shows the velocity of the peak intensity at each point, and would look similar to the color scale shown in the bottom right hand corner of Figure 1.3.

The outflows produced in these regions are generally bipolar and are observed to be perpendicular to the rotating structures (i.e. disks) observed around protostars. They are the largest scale structures involved in the formation of a single stellar system (i.e. up to 4 pc across, Wu et al., 2004), and are often observable with single dish telescopes even at the large distances to massive star forming regions. They were first classified by Snell et al. in 1980, and models describing their properties soon emerged (Hartmann & MacGregor, 1982; Konigl, 1982; Lada, 1985; Pudritz & Norman, 1986). A number of outflow properties are discussed in Shepherd (2003), and are reproduced here as Table 1.1. In this table, the first column shows the spectral types of the different mass regimes, the second shows the mass loss rates in the outflow, the third shows the momentum rates in the flows, while the last two columns show the mechanical luminosity in the flow and the bolometric luminosity of the source. Many authors claim that the large scale molecular outflows consist of material which is entrained from the surrounding material by a highly collimated jet produced somewhere in the circumstellar disk (Shepherd & Churchwell, 1996; Bachiller, 1996; Eisloffel et al., 2000; Beuther & Shepherd, 2005; Shepherd, 2005; Ray et al., 2007; McKee & Ostriker, 2007). The bipolar nature of an outflow arises from the jet material being launched from both sides of the disk.

The spectral signature of an outflow appears in the high velocity line wing emission, as does the high velocity infall described earlier. The spectral signature for outflows however, can occur on much larger spatial scales, and can generally be separated into two lobes; a bulk blueshift on one side of the source, and a bulk redshift on the other (as shown in Figure 1.4). There is no a-priori

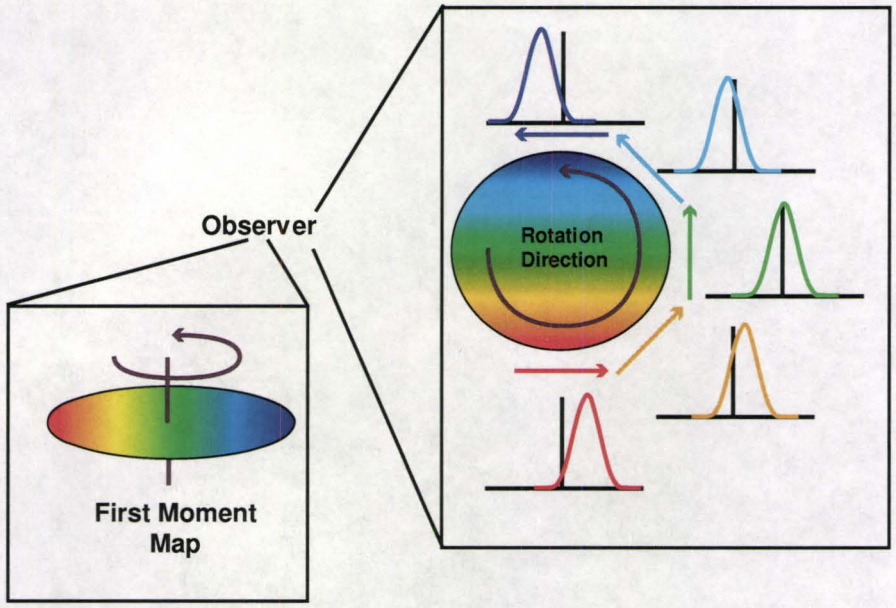

Figure 1.3: We can only observe Doppler shifts along the line of sight, and not in the plane of the sky. For a source undergoing bulk rotation, the observed spectra at various positions on the source appear as shown here. The gas on one side of the source (shown here towards the bottom) is redshifted away from the observer, while on the other side of the source (shown here towards the top), the gas is blueshifted towards the observer. At the edges of the rotating body, the Doppler shift (whether red or blue) is most pronounced, with a gradual shift towards the LSR velocity closer to the center of rotation. In each example spectrum the black vertical line shows the LSR velocity, and thus the bottom most spectrum is the most redshifted from the LSR velocity. The shift in velocity of the line peak across the source can be seen in velocity weighted integrated intensity maps, also known as first moment maps (which should look somewhat like the map shown in the bottom right corner).

Spectral Type	$\dot{M}_f$ ($M_\odot$ yr^{-1})	$\dot{P}_f$ ($M_\odot$ km s^{-1} yr^{-1})	L_{mech} ($L_\odot$)	L_{bol} ($L_\odot$)
M-F	$10^{-8} - 10^{-5}$	$10^{-7} - 10^{-4}$	$10^{-3} - 10^{-1}$	$\sim$ few
A-B	$10^{-5} - 10^{-3}$	$10^{-4} - 10^{-2}$	$10^{-1} - 10^{2}$	$\sim$ 10-30
O	?	$> 10^{-2}$	$> 10^{2}$	$> 10^{4}$

Table 1.1: Outflow Properties Described in Shepherd (2003).

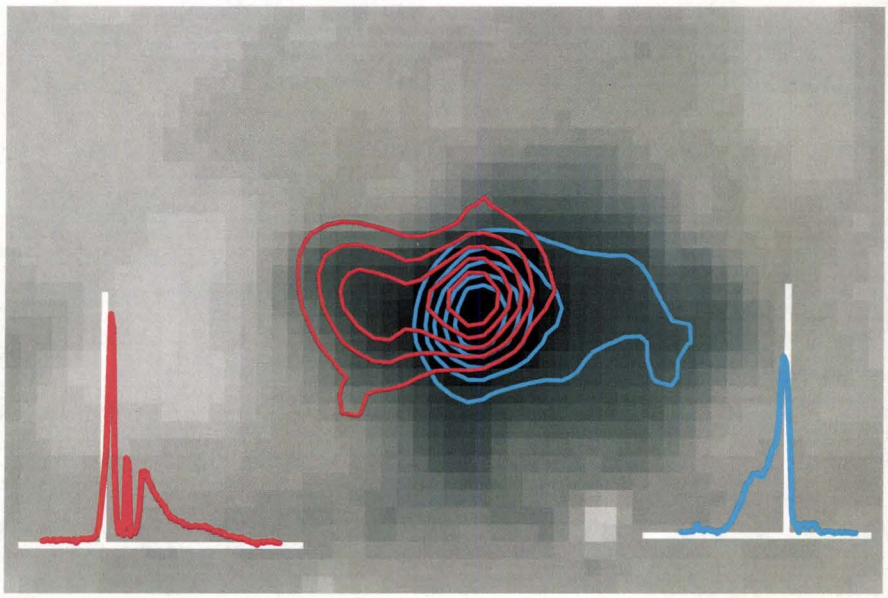

Figure 1.4: If there are bulk outflow motions, the emission spectrum at a given position will be Doppler shifted. Shown here in grayscale, is the integrated intensity of ^{12}CO along the line of sight towards the G5.89-0.39 massive star forming region observed at the JCMT, in which darker pixels have larger integrated intensities. Characteristic spectra from the red shifted and blue shifted parts of the outflow are shown in the bottom left and right hand corners of the map respectively. The white vertical line in each case shows the local standard of rest velocity of the gas. At each point in this map, the integrated intensity of the high velocity gas were determined. The outflowing gas separates into two spatially distinct outflow lobes (as shown in the red and blue contours), which only overlap at the source of the outflow. Figure modified from Klaassen et al. (2006).

reason why an infall signature would show this bipolar structure, or why it would be collimated on large scales. In Figure 1.4, we show the ^{12}CO emission from the G5.89-0.39 massive star forming regions with contours showing the intensity of the redshifted and blue shifted emission in the outflow lobes. No infall signature has yet been observed in this source (see Chapters 2 and 3). The spectra shown in this figure show examples of the emission spectra in the red lobe (bottom left corner) and blue lobe (bottom right corner). In both cases, the local standard of rest velocity is shown by the vertical white bar. From these spectra, we can see that most of the emission in the red lobe is redshifted (and shows absorption features from two line of sight clouds) and most of the emission in the blue lobe is blueshifted.

Maps like this one are two dimensional projections of 3D datacubes which have two position axes and one velocity axis. This means that for each position in the map presented in Figure 1.4, there is a corresponding spectrum which has been integrated to produce this 'integrated intensity' (or zeroth moment) map.

Instead of presenting an image with two position axes, we can produce a map with one position axis, and one velocity axis. In this instance, we do not integrate positions, but we can show the intensity of the emission at a given velocity as a function of position along a line drawn in a zeroth moment map. In this type of 'position-velocity' (PV) diagram, the three types of bulk motions described above (infall, rotation and outflow) have very different morphologies, and PV diagrams can be used as an extra check to ensure that the right motions are attributed to the line profiles. Figure 1.5 shows the profiles expected in a PV diagram for the three types of bulk flows described above. As described later in Chapter 4, infall of gas onto the HII region appears as an arc in a PV diagram due to the projection of the infall velocities on the plane of the sky. Most of the infall along the direct line of sight to the source (at a position offset of 0) has a large line of sight velocity component. At larger position offsets, less of the infall motion is detectable in the line of sight velocity component and appears to be closer to the source velocity in a PV diagram. Both the solid body portion of the rotation and the outflow appear as diagonal lines in the PV diagram since the velocity of the gas is proportional to the radius from source.

1.2.2 The Formation of Low Mass Stars

When interstellar gas and dust clouds become dense enough, their interiors become shielded enough from the background interstellar radiation field (ISRF) that the photodissociation rates of molecules such as H_2 and CO (the two most abundant molecules in the ISM) drop below the formation rates, and molecular gas clouds form (see for instance Hollenbach & Tielens, 1997). Because

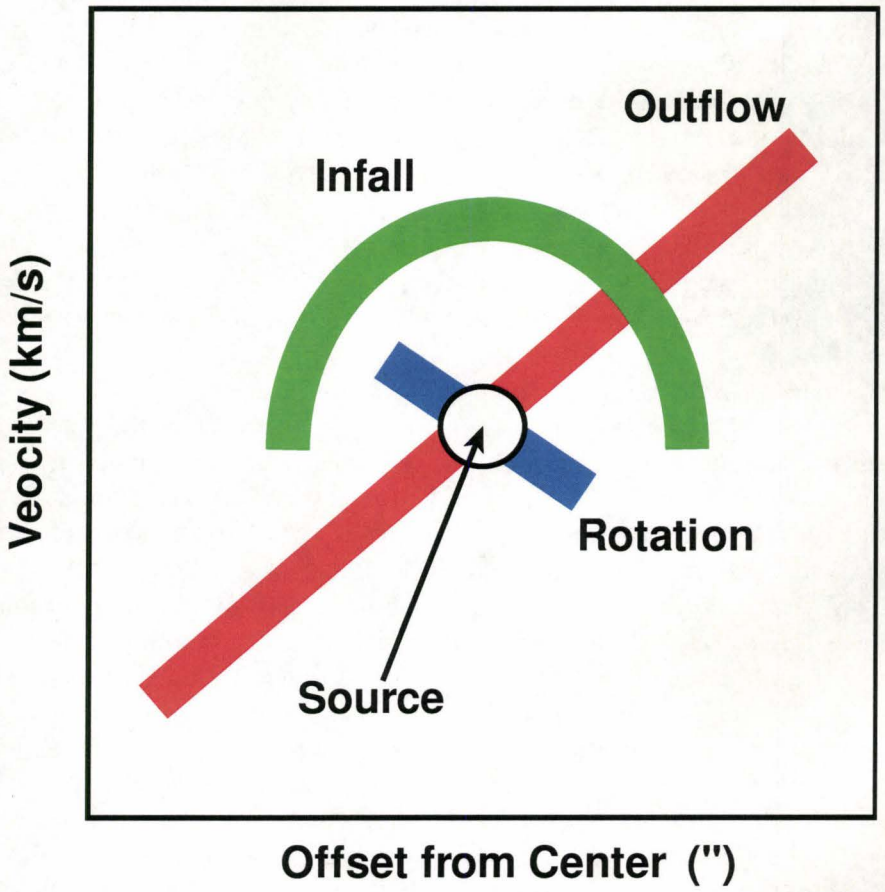

Figure 1.5: In a position-velocity (PV) diagram, infall (shown here in green) looks like a semi circle centered on the source (shown as a white circle), while rotation (shown here in blue) takes on a profile with solid body rotation in the center, and outflow (shown here in red) has a steeper slope since $V \propto r$ for an accelerating outflow.

these clouds are somewhat opaque to heating mechanisms such as the ISRF and high energy cosmic rays, and there are a large number of radiative spectral lines which can act as cooling mechanisms for these clouds, the temperatures in some of these cold cores of material can drop down to temperatures of 10 K. If these cold cores have enough material, they can become gravitationally unstable (Jeans unstable), and begin to collapse due to the lack of thermal support.

The initial angular momentum present in this cloud causes it to spin up as it collapses, and this spinning tends to flatten material into a disk perpendicular to the axis of rotation. Approximately 30% of the material in this envelope of collapsing molecular gas will eventually become part of the star (or stars) that is (are) forming at the center of the potential well (McKee & Ostriker, 2007).

As a protostar begins to form within the collapsing envelope, it begins to heat up, as well as heating up its surroundings. This changes the spectral energy distribution (SED) of the protostellar core, as the blackbody spectrum of the warm protostar overlaps with the blackbody spectrum of its colder surroundings. The stages of low mass star formation can be broken down into four general stages based on the shape of the spectral energy distribution between wavelengths of 2 and 20μm, and whether the cold envelope material or hot protostar dominates the spectrum.

As it evolves, the slope of the spectral energy distribution in the near infrared (NIR) changes (see for instance Andre et al., 1993). Figure 1.6 shows the spectral energy distributions for protostars in the four different stages ascribed to low mass star formation (Class 0 - III). For the earliest stages, most of the emission is at millimeter and submillimeter wavelengths, but as the forming star ages, it heats up, and the SED shifts to higher energies. The slope of the SEDs can be used to distinguish between the different classes of low mass protostars, and is defined by:

$$n = \frac{d(\log \nu F_\nu)}{d(\log \nu)} = -\frac{d(\log \lambda F_\lambda)}{d(\log \lambda)} \tag{1.4}$$

where λ is the wavelength of the light being observed, and F_λ is the flux (energy density) at that wavelength (Shu et al., 1987). Originally, the first class of protostar (Class I) was characterized by a rising slope of $n > 0$, meaning that most of the emission from these sources occurs at longer wavelengths (lower energies). Class II sources, characterized with slopes in the range $0 > n > -1.5$, do have most of their emission occurring at NIR wavelengths; however, there is still a lot of emission in the mid infrared due to cool circumstellar material that has not yet been removed from the envelope of the forming star. Class III sources, characterized with SED slopes of $n < -1.5$, are the most revealed sources, and the SED is generally characteristic of the pre-stellar photosphere (Shirley et al., 2000). Since the original classification scheme was developed

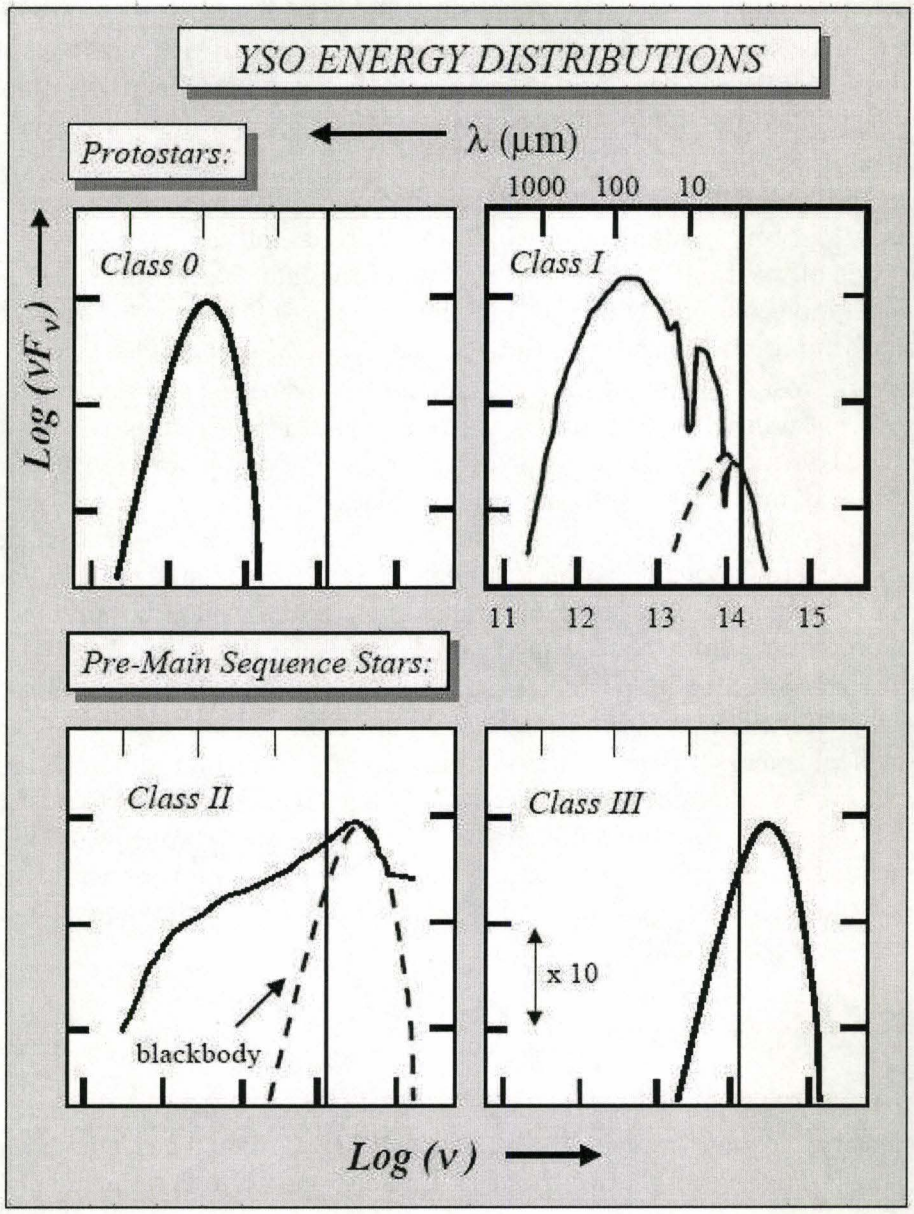

Figure 1.6: The Spectral Energy Distributions (SEDs) of regions forming low mass stars shift to higher and higher energies as the central protostar/pre-main-sequence star becomes hotter and less embedded. Figure reproduced from Lada (1999).

(Shu et al., 1987), astronomers found that by the time a Class I object was detectable in the MIR, it had already accreted most of its final mass. Thus, a Class 0 phase was added to the evolutionary scheme (see for instance Andre et al., 1993), which has no detectable emission in the NIR since its SED is still dominated by the emission from the cold envelope in which the protostar is embedded.

A contracting core of material becomes a protostar when it becomes a dynamically stable accreting object whose luminosity is dominated by accretion (Stahler & Palla, 2005). Early on (in the Class 0 stage), the SED is dominated by the black body emission from the cold envelope of material from which the protostar will form (as seen in the top left hand corner of Figure 1.6). It is during this stage that bipolar molecular outflows form. These outflows, seen in molecular line tracers such as CO and SiO, act as a release mechanism for the buildup of angular momentum in the disk as material flows onto a forming star.

In the Class I phase, much of the emission producing the SED is still coming from the envelope of gas surrounding the protostar (as seen in the top right hand panel of Figure 1.6), yet, at the high energy end of the SED, there is the beginnings of the emission from a pre-stellar photosphere (as indicated by the dashed line in the same panel of Figure 1.6).

Somewhere between the Class I and Class II phases marks the end of the protostellar evolution and the beginning of the pre main sequence evolution of the forming star. Pre main sequence stars can be placed on so-called 'Hayashi tracks' on a Hertzsprung-Russell (HR) diagram. By the time a protostar becomes a pre-main sequence star, most of the envelope has dissipated either through accretion onto or through the protostellar disk, has been entrained into the molecular outflow and been blown out of the region, or has been blown out by the forming stellar winds.

Class II sources, often also known as Classical T-Tauri Stars, show strong emission from the pre-stellar photosphere; however, there is still emission from what is left of the protostellar disk. During the last stage (Class III), the emission in the SED is from the pre main sequence star, since most of the cold envelope has been blown away. These pre main sequence stars are also referred to as Weak Lined T-Tauri Stars.

The processes involved in the formation of low mass stars can take of order 10^7 years or more, from the Class 0 stage to a main sequence star. For higher (final) mass stars, the formation timescale decreases, and at approximately $8M_\odot$, the Kelvin-Helmholtz contraction timescale ($T_{\rm KH} \propto M_*/R_*L_*$) becomes shorter than the formation timescale ($t_{\rm form} = M_*/\dot{M}_{\rm acc}$), and the forming star will no longer go through a phase of quasi-static contraction onto the main sequence (there is no pre main sequence phase for high mass stars).

The shorter formation timescales for high mass stars mean that we cannot

classify the various stages of high mass star formation in terms of the spectral energy distribution like in the lower mass case, since the high mass protostar is going through the various stages much more rapidly than the lower mass forming stars, and the spectral energy distribution moves quite quickly (of order 10^4 years, Wood & Churchwell (1989)) from the submillimeter into the ultraviolet, where massive stars radiate most of their energy. The highly embedded nature of massive star formation also makes SED modeling quite challenging (see for instance, Robitaille, 2008). For instance, Robitaille (2008), discuss how there are a large number of parameter sets which can each fit the same SED.

1.2.3 The Formation of High Mass Stars

The short protostellar lifetimes and relatively infrequent formation of high mass stars mean that the closest examples of high mass star formation are further away than the closest examples of low mass star formation. Some nearby examples of low mass star forming regions include the Taurus (147 pc Loinard et al., 2007) and Ophiuchus (140 pc Mamajek, 2008) clouds, while the closest example of high mass star formation is in Orion (414 pc Menten et al., 2007). Thus, we cannot achieve the same spatial resolution of the gas and dust in high mass star forming regions as we can in their lower mass counterparts, further hampering efforts to understand how they form.

For low mass stars, classifying the evolutionary stage with respect to changes in the spectral energy distribution makes sense since the processes involved take a long time (of order 10^7 yr, Andre et al., 2000), and the protostar becomes less embedded with time. The same does not hold for massive stars.

In the higher mass case, there is no revealed formation phase; the protostar joins the main sequence while till accreting material from its natal core (Keto & Wood, 2006). The timescales involved in the formation of massive stars are also comparatively short ($\sim 10^5$ yr, McKee & Ostriker, 2007), and the SED would change from peaking in the radio to peaking in the UV in a shorter time than the entire lifetime of the pre-stellar core phase of low mass star formation (Andre et al., 2000).

Another problem for classifying massive stars using the lower mass evolutionary scheme is the presence of high energy photons produced by the rapid core hydrogen fusion. The ionizing photons can act to photoevaporate a circumstellar disk and far UV photons can dissociate the ambient molecular gas (McKee & Ostriker, 2007). Thus, a different evolutionary sequence must be explored.

In recent years, a sequence for massive star formation has been suggested (see, for instance, Beuther & Shepherd, 2005; Zinnecker & Yorke, 2007; McKee & Ostriker, 2007). The column densities required to form massive stars are of order 10^{23}-10^{24} cm^{-2} (McKee & Ostriker, 2007), and the corresponding volume

densities ($\gtrsim 10^6$ cm^{-3} Plume et al., 1997) are such that these massive cores are very dense and very cold. These High Mass Starless Cores (HMSCs Evans et al., 2002) are so cold that they can absorb the background emission along the line of sight, and can appear as IR Dark Clouds (IRDCs Egan et al., 1998; Pillai et al., 2006). Once the protostar begins heating its environment, the core in which the protostar is embedded becomes visible at sub millimeter and IR wavelengths and the rise in temperature opens a large number of molecular reaction pathways. This stage of high mass star formation (the Hot Core phase) is generally characterized by rich chemical signatures (i.e. van der Tak, 2005).

Throughout the hot core phase, the protostar is gaining mass and its temperature is increasing. Eventually, at approximately 8 $M_\odot$, the protostar becomes hot enough to start ionizing its surroundings, and a hypercompact HII (HCHII) region forms. As this HCHII region ages, it expands and becomes an ultracompact HII (UCHII) region, and then later goes on to become a classical HII region. Hereafter, when we refer to HII regions, we are using this term as a short form for HC/UCHII regions unless explicitly stated otherwise.

One parallel that can be drawn with the low mass case, and is often used as a line of reasoning for the formation processes being the same, is the presence of bipolar molecular outflows. In each of the phases described above, there are examples of sources shown to have associated outflow activity. The IRDC 18223-3 has been shown by Beuther et al. (2005) to have a molecular outflow indicating that, as for the low mass case, outflows are present in even the earliest phases of star formation. Examples of hot cores with outflow detections include those in the survey of Sridharan et al. (2002), and outflows have been detected surrounding numerous HC/UCHII region as well (see, for instance, Beuther et al., 2002). The presence of outflows early on in the formation of a high mass star suggests that at least parts of the observed outflows must be due to centrifugally driven (i.e. disk driven) winds or jets since a radiatively driven wind could not occur in the lower temperature environment of an IRDC.

The outflows associated with the highest mass stars do appear to be systematically less collimated than those from lower mass protostars (Beuther & Shepherd, 2005). This phenomenon can be qualitatively understood in terms of a massive protostar which continued to accrete and evolve despite already being on, or very close to, the main sequence. If a protostar reaches the main sequence as a mid/early B star, it may still be deeply embedded enough in its natal core to continue accreting material. If this is the case, then as the star ages, it evolves to earlier spectral types (i.e. Keto & Wood, 2006). Thus, the lack of collimation in the outflows from the most massive stars may be due to age and not an underlying difference in driving mechanism (Beuther & Shepherd, 2005).

That there may be a different driving mechanism for the outflows from the

highest mass stars has been suggested for a number of reasons. The first is that the outflows from these stars are not as collimated as those from lower mass stars (which was discussed above), and the second is that radiation driven winds may be able to explain both the energetics of, and lack of collimation in, these outflows. The third reason is the lack of observed disks around O stars. However, photoevaporative winds, and very short formation timescales make observing dynamically stable disks around these stars highly unlikely.

Banerjee & Pudritz (2007) found that, when magnetic field are included in their code, their massive cores can produce outflows in a manner similar to that suggested for lower mass star forming regions. Krumholz et al. (2005a) have shown that the outflows from massive stars (50 $M_{\odot}$ in their simulations) can act to funnel the radiation pressure from the massive star, and lower the temperature in the equatorial region, allowing for material to continue to accrete onto the massive star. It appears as though outflows play a major role in the formation of stars on all mass scales.

Returning to the proposed evolutionary sequence, we find that how HMSCs form, whether via turbulent collapse and disk accretion (McKee & Tan, 2002, 2003), or competitive accretion and stellar collisions (Bonnell et al., 1998, 2003) is still not clear.

In the first model, a single, turbulent dense core begins to collapse, and the mass infall rate is determined through the surface density of the collapsing core. The infalling material can then form an accretion disk as is the case for lower mass stars. Assumptions inherent to this model are that the stars form from pre assembled cores (which has been shown by Beuther et al., 2005, to be a valid assumption), that these collapsing cores start off near virial equilibrium with their surroundings, and that they are magnetically super critical (i.e., magnetic fields alone cannot prevent collapse, McKee & Ostriker, 2007). A major criticism of this model is that the massive collapsing core could fragment into a number of lower mass stars instead of forming a massive star (Dobbs et al., 2005).

The second model suggests that collapse can begin in a number of regions within a star forming environment. Each of these protostellar 'seeds' is able to draw mass from its surroundings, and the size of this region is limited by how massive the seed is (i.e. the radius within which material is gravitationally bound to the seed). Nearby protostellar seeds then begin competing for material to accrete as their accretion domains begin to overlap. Assuming low angular momentum, and therefore minimal turbulent motions (Bate & Bonnell, 2005), the interaction cross section of two seeds becomes the edges of their accretion domains (Stahler et al., 2000), and the seeds can be drawn in towards each other and merge/collide and form a more massive protostar. Criticisms for this model include the extremely high stellar densities (10^8 pc^{-3}, Bonnell et al., 1998) required for this mechanism to form the most massive stars. For

comparison, the densest star forming region observed in the Milky Way (W3 IRS5, Megeath et al., 2005) has a stellar density of order 10^5 pc^{-3}.

The biggest difference between these two models (as suggested by Zinnecker & Yorke, 2007) is that the turbulent collapse model requires all of the final mass to have built up before star formation starts, while competitive accretion allows for mass to build up during star formation.

McKee & Ostriker (2007) suggest a number of observational tests which could be used to distinguish between these models. These tests include determining whether the core mass function maps to the IMF (which would suggest that mass is built up before star formation starts), observing the properties of disks and winds and the distribution of circumstellar material (through SED modeling) as well as chemical signatures which could reveal the ages of these regions (see Shirley, 2007, for how this can be done for lower mass regions).

Regardless of which of these two scenarios is responsible for the earliest stages of massive star formation, we know that something causes IRDCs to form, and that these regions heat up and become Hot Cores. What is not as clear is how (or whether) accretion can be responsible for the formation of the most massive stars when strong radiation pressures begin pushing outward when the protostar reaches approximately $8M_{\odot}$.

In a spherically symmetric scenario, the outward ionizing radiation from a forming star should be high enough to halt infall and accretion of material onto the protostar, yet somehow, stars much more massive than $8M_{\odot}$ are observed, and therefore must be able to form despite these outward forces.

High accretion rates (Edgar & Clarke, 2003), those above a certain critical value (i.e. $\dot{M}_{\rm crit} = 2\sqrt{\pi}\mu m_H \sqrt{N_u G M_*/\alpha_B}$ Garay & Lizano, 1999) may delay the formation of an HII region; however it cannot quench an HII region completely.

Some authors suggest accretion can continue by reducing the effective outward radiation pressure. These models include reducing the dust opacity (Wolfire & Cassinelli, 1987), rotating collapse (Terebey et al., 1984), or the outflow models discussed earlier (Krumholz et al., 2005a, i.e.). Krumholz & Bonnell (2007) suggest that if there were a disk present, it could shield material falling through the disk against the strong radiation pressures which would be funneled away from the plane of the disk. Conversely, other authors have suggested that instead of overcoming the ionizing radiation of the source, that material can either cross the ionization boundary, become ionized itself and continue to accrete onto the forming star (Keto, 2003; Keto & Wood, 2006), or accretion can cease when the high accretion rate is no longer sufficient to quench the formation of the HII region (Klaassen et al., 2006).

These last two models (ionized and halted accretion) are both supported by observational evidence, as described below.

G10.62-0.38 (hereafter G10.6) is a well studied ultracompact HII (UCHII)

region (Ho et al. 1981, Keto et al. 1988, etc) through which the surrounding gas falls in, becoming ionized, and continuing to fall in towards the central star. The high resolution observations of Keto & Wood (2006) show an infall signature in ionized gas, and the observations of Sollins et al. (2005) show an infall signature of molecular gas onto the HII region (see also Chapter 3). It thus appears as though accretion onto the protostar is, in this case, ionized and is continuing beyond the formation of the UCHII region.

G5.89-0.39 (hereafter G5.89) is another well studied UCHII region (the archetypal shell UHCII region from Wood & Churchwell 1989) and has been shown to have a number of outflows, depending on the molecular tracer observed. This region appears to be the formation site for a number of massive stars including the O5V star which is believed to power the HII region (Feldt et al. 2003) and a 1.3 mm continuum source believed to be powering the SiO outflow detected by Sollins et al. (2004). To date, there are no published CO maps of this region at high enough resolution to determine which of these sources (each separated by $\sim 2''$) lies at the center of the large scale decelerating outflow observed by Klaassen et al. (2006) and Watson et al. (2007). Klaassen et al. (2006) suggested that accretion onto the source powering the large scale outflow may have halted at the onset of the HII region.

These studies of G10.6 and G5.89 suggest that high neutral accretion rates (up to 10^{-2} $M_{\odot}$/yr, Edgar & Clarke 2003) and continued ionized accretion can both account for the formation of massive stars. Yet, these conclusions are based on the in depth studies of two individual regions, and from these two regions, we cannot make conclusive statements about the general nature of massive star formation. In order to determine whether there is a preferred method, we need to observe these processes in a number of regions, and build up statistics about whether/how accretion onto a massive protostar occurs beyond the onset of dynamical expansion in the UCHII regions.

1.3 Outline of Thesis

Here, we present observations aimed at addressing the question about infall and outflow activity in massive star forming regions once an HII region (whether hypercompact or ultracompact) has formed. For instance, we address whether large scale infall and outflow are observable from UCHII regions, and we determine the small scale gas kinematics of a smaller sample of massive star forming regions to see whether infall is ongoing, whether small scale rotation exists, and whether the large scale outflows ascribed to massive star forming regions do originate from the HII region, or some other, nearby source.

With these studies of the molecular gas kinematics surrounding regions forming massive stars, we can determine properties of the gas which can be used to constrain model predictions (i.e. how much energy must be released

by the forming star to shock its surroundings, as described in Chapter 3).

In Chapter 2, we present our initial survey of 23 massive star forming regions which were each previously known to have UCHII regions as well as molecular outflows. We find that only approximately 60% of the sources observed had active outflow signatures, suggesting that the source powering the other outflows (i.e. active accretion onto the massive stars) has ceased. Of the sources with active outflow sources, 50% show evidence for infall.

In Chapter 3, we present followup maps in which we observed six of the sources from Chapter 2, as well as G10.6 (the ionized accretion source described above). We find similar results to Chapter 2, but have also been able to quantify the amount of energy required to power the shocks in these regions, and mass infall rates onto the sources with infall detections.

In Chapter 4, we present much higher resolution observations of infall and rotation towards five massive star forming regions. All but one of these sources shows evidence for infall onto the HII region, suggesting a long period of continued infall after the formation of the HII region. We also find that the warm gas directly outside of the HII region is rotating. While this is not a detection of disks around the highest mass stars, it does suggest that large scale rotation may play a role in massive star formation, and the observed molecular outflows.

In Chapter 5, we present high resolution observations of the gas towards the same five HII regions; however, in this chapter, we focus on the large scale structures associated with the outflowing gas from these regions. Towards three of these sources, we detect collimated outflows which appear to be produced either in, or at the surface of the HII regions. The data presented here are incomplete, but the gas kinematics and morphology implied so far suggest that these outflows are powered by massive stars.

In Chapter 6 we summarize our results, discuss their implications for models of massive star formation, and introduce future work.

Chapter 2

Outflow and Infall in a Sample of Massive Star Forming Regions.

This chapter has previously been published by the Astrophysical Journal as an article titled "Outflow and Infall in a Sample of Massive Star-forming Regions." by P.D. Klaassen, and C.D Wilson (The Astrophysical Journal, Volume 663, Issue 2, pp. 1092-1102). Reproduced with permission of the American Astronomical Society.

An erratum to this paper has also been published by the Astrophysical Journal. It is to appear in the September 1, 2008, v684n1 issue. The errata related to the column density values presented in Table 2.3, and figures 2.5, 2.6 and 2.9. The results presented here incorporate the corrected values and figures.

2.1 Introduction

The dynamics in massive star forming regions are, in general, much more complex than in regions which form only low mass stars. For instance, in the early stages within a low mass star forming region, the dynamics can be understood in terms of a few broad categories: large scale infall, which causes a disk to form, accretion through the disk, and outflow to release angular momentum (see for example Di Francesco et al., 2001; Andre et al., 1993; Muzerolle et al., 2003). In intermediate and high mass star forming regions, turbulence, stellar winds, multiple sites of star formation, and, for regions with massive star formation, the presence of HII regions, all contribute to the dynamics in these regions as well (i.e. Beuther et al., 2007; Shepherd & Churchwell, 1996; McKee & Tan, 2003; Krumholz et al., 2005b). The more complicated source dynamics make the processes involved in the formation of

the most massive stars much more difficult to understand than those involved in the formation of lower mass stars. Adding to the complexity, massive stars do not form as often as their lower mass counterparts and so we must look to larger distances before finding examples of high mass star formation. For instance, the average distance to the 63 sources in Shirley et al. (2003, hereafter S03) is 5.3 kpc.

If we assume massive stars form through accretion, that this accretion occurs in the inner regions of disks (i.e. Pudritz & Norman, 1986; Shu et al., 1994), and that these disks have radii of a few thousand AU (Chini et al., 2004; Beltrán et al., 2004; Cesaroni et al., 2005), we do not yet quite have the resolving power to detect accretion directly at the distances to massive star forming regions (1000 AU at 5.3 kpc is $\sim 0.2''$). Here, we define accretion as the infall motions from the disk onto the forming star, in contrast to the larger scale motions of envelope material falling onto the disk. However, while we cannot observe accretion directly, its presence can be inferred from the presence of accretion tracers such as larger scale infall and outflow. Infall can act to replenish disk material as mass accretes onto a protostar (Nakamura, 2000), while molecular outflows serve as a release mechanism for the angular momentum which builds up during the accretion process (e.g Arce et al., 2007). These large scale motions are seen in star forming regions of all mass scales (see for instance Beuther & Shepherd, 2005).

In massive star forming regions, the accretion rates are orders of magnitude greater than in low mass star forming regions (i.e. Beuther et al., 2002), while the accreted masses are only approximately one order of magnitude greater. These accretion rates and masses result in accretion timescales that are much shorter than in low mass star forming regions, which allows the Kelvin-Helmholtz timescale to become important in the evolution of the protostar (e.g., there is no pre-main sequence stage for massive star formation). The outward radiation and thermal pressure from the forming star becomes strong enough that it can ionize the surrounding medium and a small, highly ionized HII region (either hypercompact (HCHII) or ultracompact (UCHII) region Keto, 2003) can form. It is still unclear whether the outward pressure needed to create the HII region is strong enough to halt accretion, or whether accretion can continue in some form (either through a molecular or ionized disk, or through an ionized accretion flow) after the formation of an HII region. Some models suggest that accretion must halt before the onset of a visible UCHII region (i.e. Garay & Lizano, 1999; Yorke, 2002), while other models suggest that an ionized accretion flow can continue through an HII region (i.e. Keto, 2003, 2007).

There is now also observational evidence which suggests that, once the protostar becomes hot enough to ionize its surroundings, both modes of massive star formation (halted and ionized accretion) are possible. G10.6-0.4 has been

shown to have an ionized accretion flow by Sollins et al. (2005) and Keto & Wood (2006), while accretion in G5.89-0.39 seems to have halted at the onset of the UCHII region (Klaassen et al., 2006). Although sample statistics at this point are still quite small, these two examples pose interesting questions. We do not yet have enough data to determine whether the apparently conflicting models of halted and ionized accretion can both be correct. However, we can begin with a uniform survey of infall and outflow tracers in massive star forming regions in order to constrain massive star formation scenarios.

In this paper, we present a survey of 23 massive star forming regions. Because we are interested in the relationship between accretion and outflow after the formation of an HII region, our source selection criteria include (1) the presence of an UCHII region, which indicates that there is a massive protostar forming, and (2) previous evidence of outflows, which suggests ongoing accretion in most formation scenarios. Sources were selected based on inclusion in the Wood & Churchwell (1989) and Kurtz et al. (1994) catalogs of UCHII regions as well as having molecular outflow signatures in the Plume et al. (1992) survey of massive star forming regions. Additional sources were taken from Hunter (1997) which were shown to have both UCHII regions and molecular outflows.

We describe the observations collected for this survey in Section 2.2, we discuss the results of these observations in Section 2.3, and present our conclusions in Section 2.4.

2.2 Observations

Observations of SiO (J=8-7), HCO^+, and $H^{13}CO^+$ (J=4-3) were taken at the James Clerk Maxwell Telescope (JCMT)[1] in 2005 (as parts of projects M05AC11 and M05BC04). SiO (347.330 GHz) and $H^{13}CO^+$ (346.999 GHz) were observed simultaneously in the same sideband by tuning the receiver to 347.165 GHz. Thirteen or twenty minute observations, depending on the source elevation, were taken towards each source with a velocity resolution of 1.08 km s^{-1}, which resulted in rms noise levels of T_{MB} <0.07 K. Separately, we observed HCO^+ (356.370 GHz) with a velocity resolution of 0.53 km s^{-1} to an rms noise limit of T_{MB} <0.13 K in twenty minute integrations. Both sets of observations were taken in position switching mode with dual mixers and a sideband rejection filter in place. Table 2.1 shows the positions, rms noise limits of both tunings, the local standard of rest velocity, and distances to all sources in this survey. The half power beam width for these observations is

[1]The James Clerk Maxwell Telescope is operated by The Joint Astronomy Centre on behalf of the Particle Physics and Astronomy Research Council of the United Kingdom, the Netherlands Organisation for Scientific Research, and the National Research Council of Canada.

15″, and the main beam efficiency is $\eta_{\rm mb}$=0.62. Data were obtained using the DAS autocorrelator system and reduced using the SPECX software package.

Linear baselines were removed from all spectra except for those towards G10.47. For this source, there were so many different chemical species in the observed spectrum that we were unable to fit a linear baseline over the entire $\sim$ 700 km s^{-1} bandwidth of the 347 GHz observations or the $\sim$ 450 km s^{-1} bandwidth of the 356 GHz observations. In this case, no baseline was removed.

We also present 9 × 9 maps of one source (G45.07) in the same emission lines. These raster maps are sampled every 5" and have rms noise limits of 0.10 and 0.14 K (T_{MB}) for the 347 and 356 GHz tunings, respectively. Note that these values are different than the ones reported in Table 2.1 for the single pointing observations. The DAS autocorrelator was configured with the same tunings as were described above for the single pointing observations, and the maps were centered at the same position.

2.3 Results

This survey of single pointing observations towards 23 massive star forming regions is meant as an initial, uniform survey from which to base future observations. With these observations, we can only comment on the molecular gas component within our beams; we cannot discuss the larger scale molecular dynamics, or the ionized gas components of these regions. For our sources, the selection criteria of having an HII region confirms that these regions are forming massive stars.

Figures 2.1 through 2.4 show the single pointing SiO and $HCO^+/H^{13}CO^+$ spectra towards all sources; the spectra are ordered according to SiO integrated intensity. For each panel in these figures, line brightnesses have been corrected for the JCMT main beam efficiency and centered on the $V_{\rm LSR}$ of the source (Table 2.1). Figures 2.1 and 2.2 show SiO and $HCO^+/H^{13}CO^+$ spectra, respectively, towards the sources with no SiO detections. Figures 2.3 and 2.4 show the SiO and $HCO^+/H^{13}CO^+$ spectra, respectively, towards sources with SiO detections. Peak line strengths and integrated intensities are given for all three lines in Table 2.3.

SiO was only detected in 14 out of our 23 sources, where we define a detection as a minimum of 4 σ in integrated intensity. The rms noise limits in integrated intensity were calculated using $\Delta I = T_{\rm rms}\Delta v\sqrt{N_{\rm chan}}$ where $T_{\rm rms}$ is the rms noise level in K, Δv is the velocity resolution of the observations, and $N_{\rm chan}$ is the number of channels over which the integrated intensity is calculated. HCO^+ was detected in all sources and $H^{13}CO^+$ was detected in all but two sources. Along with HCO^+, we serendipitously observed SO_2 (J=$10_{4,6}$-$10_{3,7}$ at 356.755 GHz) in 17 of our sources. The HCO^+ and SO_2 lines are only separated by 17 km s^{-1} and thus the lines were blended in eight sources.

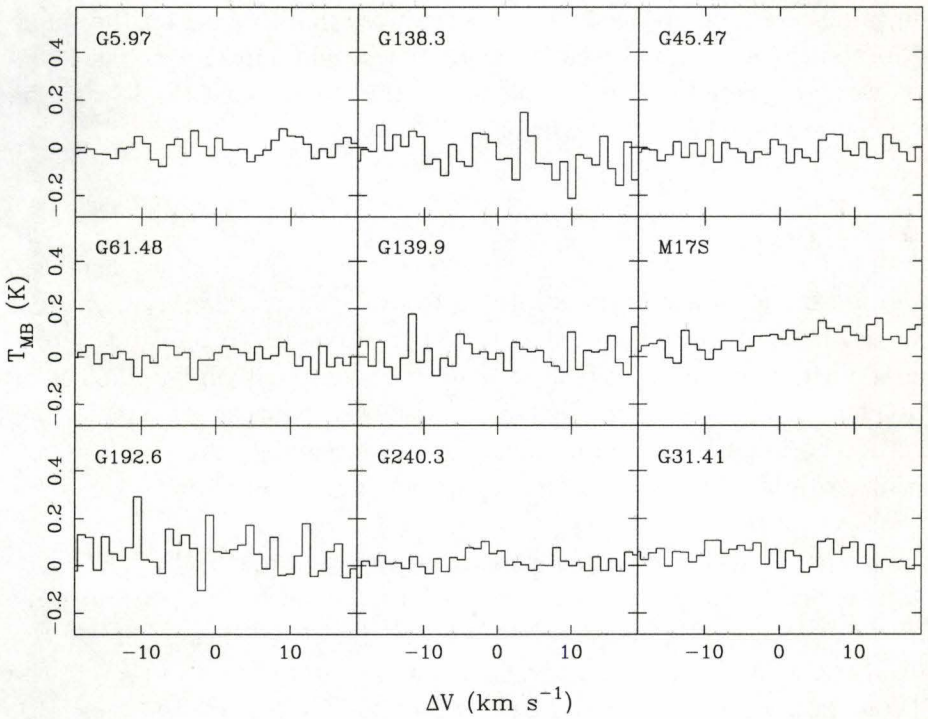

Figure 2.1: Nine sources in which SiO was not detected (to 4 σ limits). The name of each source is given in the top left hand corner of each panel. For each source, the source rest velocity is plotted as $\Delta v = 0$ km s^{-1}.

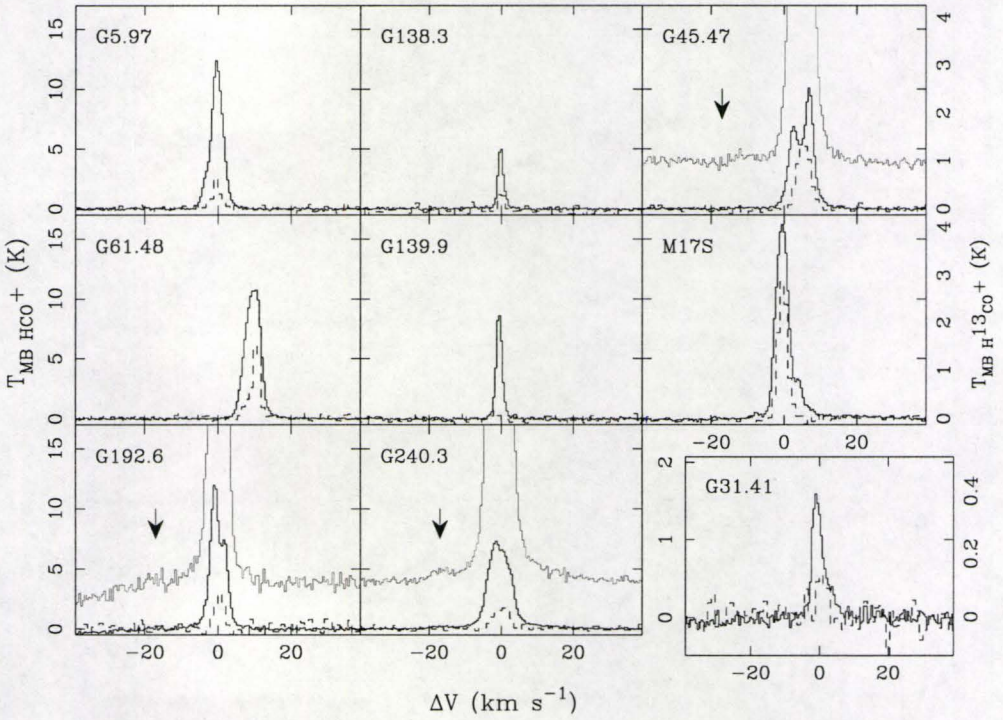

Figure 2.2: HCO^+ and $H^{13}CO^+$ sources with no SiO detections (the same sources as in Figure 2.1). Solid lines show HCO^+ emission, while dashed lines show $H^{13}CO^+$ emission scaled up by a factor of four. The temperature scale on the left hand side of the panels is the scale used for the HCO^+ spectra, and the temperature scale on the right hand side is that used for the $H^{13}CO^+$ spectra. For sources with SO_2 detections, we have re-plotted the HCO^+ spectra on a larger intensity scale (from -1 K to 3 K, in gray) to show the low lying SO_2 emission. The SO_2 emission, when present, is centered at -17 km s^{-1}, and is indicated by an arrow. G31.41 is slightly offset to emphasize that the temperature scale has been magnified to show the emission feature.

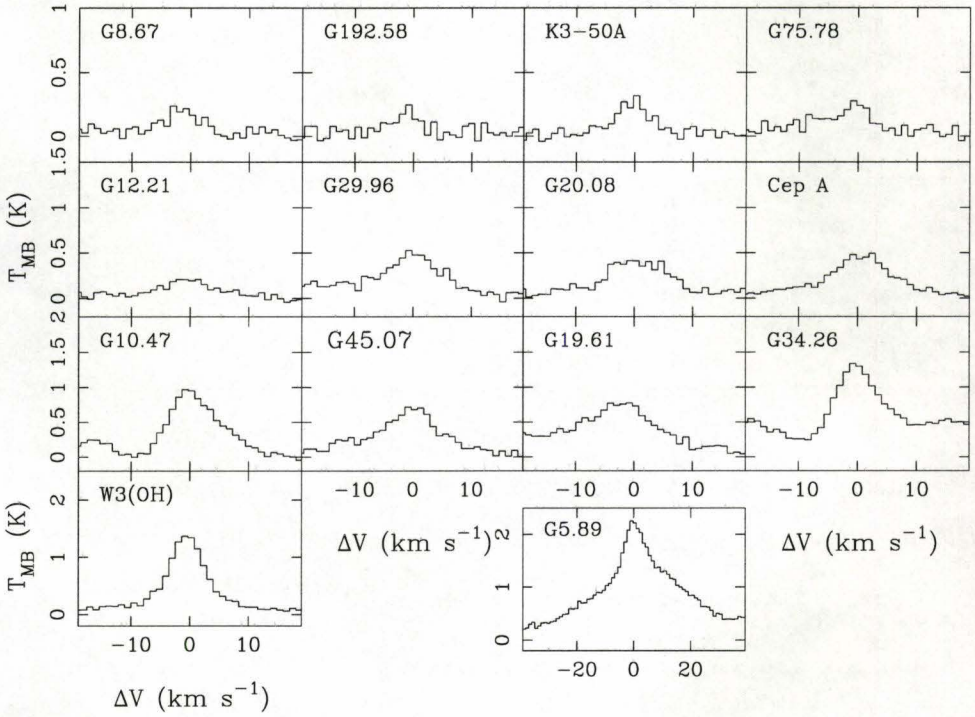

Figure 2.3: SiO spectra for 14 source in which SiO was detected (above 4 σ limits). For this figure only, the range of temperatures plotted increases by row. The plotted temperature ranges for each row increase by 0.5 K per row. The temperature scale in the top row extends from 0.2 to 1 K (in the $T_{\rm MB}$ scale), while the temperature scale in the bottom row extends from 0.2 to 2.5 K. Note that the velocity scale for G5.89 is much wider (a 78 km s^{-1} window as opposed to a 38 km s^{-1} window for the other sources) in order to show the full width of the emission line, but that the temperature scale is the same as that for W3(OH).

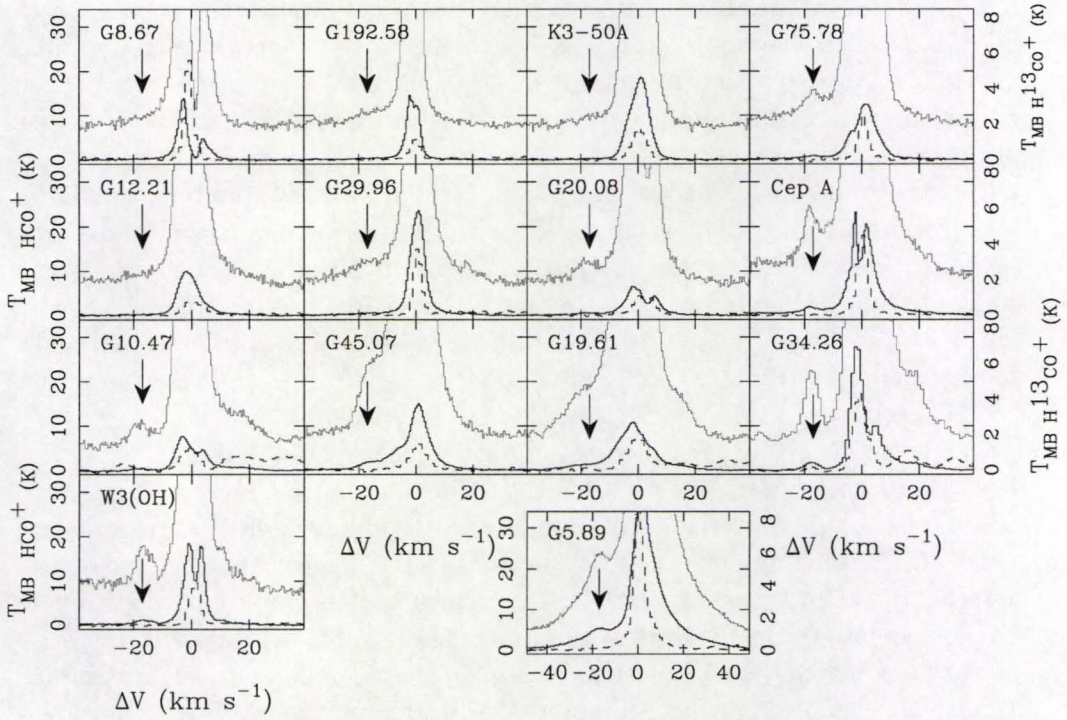

Figure 2.4: HCO^+ and $H^{13}CO^+$ emission from sources with SiO detections (the same sources as in Figure 2.3). The solid, dashed and gray lines are the same as shown in Figure 2.2, as is the placement of the temperature scales. As in Figure 2.3, G5.89 has been plotted separately from the rest of the sources to stress that the velocity scale is larger for this source.

For the sources with SO_2 detections, we have also plotted (in gray) the lower intensity HCO^+ observations in order to highlight the SO_2 emission (Figures 2.2 and 2.4).

Double peaked HCO^+ line profiles were observed towards 10 sources, with nine of them having stronger blue peaks than red. This blue line asymmetry in an optically thick tracer such as HCO^+ is often suggestive of infall (i.e. Myers et al., 1996). We discuss the possibility of our observations tracing large scale infall further in Section 2.3.2.

The distances to our sources, as taken from the literature, are shown in Table 2.1. The average distance is 5.7 $\pm$ 3.8 kpc, where the error quoted reflects the 1 σ dispersion in the distances. Since our observations were taken with a 15″ beam, this resolution corresponds an average linear size of 0.4 pc for our observations.

SiO is a well known outflow tracer, since in the general interstellar medium, Si is frozen out onto dust grains. When the gas in a region is shocked (i.e. the gas through which a protostellar outflow is passing) the dust grains can sublimate and Si is released into the gas phase. After the passage of a shock, the SiO abundance ($[SiO]/[H_2]$) can jump to almost 10^{-6}, whereas the dark cloud abundance of SiO is often closer to 10^{-12} (see for example Schilke et al., 1997; Caselli et al., 1997; van Dishoeck & Blake, 1998).

While SiO is easily identified as an outflow tracer, the emitting region for HCO^+ is much less certain. Many authors suggest that HCO^+ can be used to trace the envelope material surrounding a protostellar region (i.e. Hogerheijde et al., 1997; Rawlings et al., 2004), while others suggest that it traces disk material (i.e. Dutrey et al., 1997). One thing that is apparent, however, is that it becomes optically thick very quickly and readily self absorbs.

We detected SO_2 in 17 of our sources, suggesting that our beam contains at least some molecular gas at temperatures greater than 100 K (see for instance Doty et al., 2002; Charnley, 1997). However, Fontani et al. (2002) have determined the average temperature in twelve massive star forming regions to be 44 K, using observations with beam sizes comparable to those presented here. For seven of our sources, which were observed in the Fontani et al. (2002) sample, the average temperature is also 44 K. Thus, in the following analysis, we adopt an ambient temperature of 44 K for all sources.

Table 2.3 shows the column densities for each region derived for both SiO and $H^{13}CO^+$. The column density was calculated assuming that each tracer is optically thin, in local thermodynamic equilibrium, and at an ambient temperature of 44 K. For optically thin lines, the column density of the observed transition scales directly with the integrated intensity of the line (see for instance Tielens, 2005):

$$N_u = \frac{8k\pi\nu^2}{hc^3}\frac{1}{A_{u\ell}}\int T_{\rm MB}dv \qquad (2.1)$$

where N_u is the column density in the upper state of the transition, $A_{u\ell}$ is the Einstein A coefficient, ν is the frequency of the J=u-ℓ transition, and $\int T_{\rm MB} dv$ is the integrated intensity of the line. The column density of this one state can then be related to the total column density of that molecule through the partition function. It is the total column density for the molecule (not the observed state) that is presented in Table 2.3.

2.3.1 Source Properties Derived from SiO Observations

For each source we determined the column density, or upper limit to the column density, in SiO (Table 2.3) using the methods described above. These column densities can be compared to the column densities of other molecules (i.e. CS) for the same regions in order to determine the fractional abundance of SiO, if the abundance of the other molecule is known. We were able to obtain the CS or $C^{34}S$ column densities for fifteen of our sources from the literature. Column densities for fourteen sources were taken from Plume et al. (1997, hereafter P97), with the column density for one additional source taken from Wang et al. (1993). For those sources with $C^{34}S$ column densities instead of CS column densities, we assumed an abundance ratio of $[CS]/[C^{34}S] = 22$ (Wilson & Rood, 1994) to determine a CS column density. The abundance of CS, relative to H_2, was calculated by S03 for 13 of these sources, and we assume a CS abundance of 1.2×10^{-9} for the other two source for which the CS column density is known, since this was the average CS abundance as calculated by S03. We then compare the column density and abundance of CS to our observed SiO column density, or column density upper limit, to determine the abundance of SiO relative to H_2 in our sources (Table 2.3).

Despite our source selection criteria requiring previous evidence of outflows, we detected SiO towards only 14 of our 23 sources. This raises a number of questions, such as: is the observed SiO in fact tracing outflow if we do not detect it in all sources? Why do we not detect SiO in all sources? Is the signal being beam diluted at large distances? Has the Si evolved into other species? Below we first address whether the detected SiO can be used as an outflow tracer, and then discuss reasons for our non-detections of SiO in nine of our sources.

Si is liberated in shocks, and if these shocks are not due to the outflow, they must be due to the photo dissociation region (PDR) surrounding the UCHII region. Evidence for diffuse (not collimated) SiO can be seen in W75N (Shepherd et al., 2004) suggesting that the SiO may be due to the PDR and not an outflow. Models and observations of SiO in the PDRs around high mass star forming regions suggest moderate SiO enhancement, and that the SiO abundance is independent of the ambient radiation field (i.e. Schilke et al., 2001). Schilke et al. (2001) find SiO column densities of $\sim 10^{12}$ cm^{-2}

in their observed PDRs. This is, admittedly, below our detection threshold; however, we detect average SiO column densities of $\sim 10^{14}$ cm^{-2}. This suggests a possibly higher SiO abundance than found in PDRs.

The enhanced SiO column density alone is not enough to discount the origin of the SiO in our sources as the PDR and so we can consider how our SiO abundance varies with the ambient radiation field. For the gas near an HII region, we can approximate the strength of the ambient radiation field using the Far Infrared (FIR) luminosity of the region. For twelve of our sources with SiO detections and abundance calculations, we obtained the FIR luminosity from either Wood & Churchwell (1989), Kurtz et al. (1994) or Evans et al. (1981). We then scaled their values for the different source distances used in this study (see Table 2.3). Comparing the SiO abundance to the source luminosity (see Figure 2.5), we find that the SiO abundance increases with source luminosity. There is a 10% chance that this relationship could arise from uncorrelated data. Thus, it is possible that our result is contrary to the findings of Schilke et al. (2001), and we suggest that the SiO we observe does come primarily from outflow shocks.

We can also compare our detection rate of SiO to that of the SiO survey towards maser sources of Harju et al. (1998) who observed SiO (J=2-1) and SiO (J=3-2). For comparison to our results, we only consider the sources in Harju et al. which are listed as UCHII regions. Our detection rate is 61%, compared to their rate of 29%. While our detection threshold is slightly lower (our observations have rms noise levels generally below 0.05 K at 347 GHz, while their rms noise levels are generally below 0.08 K), we suggest that the different detection rates are due to differences in the source selection criteria. Although both samples contain UCHII regions, our sample contains sources with previous observations of outflows, while Harju et al. have selected sources based on previous observations of masers. For the 12 sources which overlap between the two studies, we detect SiO towards 9 sources, while they detect SiO towards 10. They detected SiO (J=2-1) in G31.41 while we did not detect it in SiO (J=8-7).

Based on this comparison to SiO observations of UCHII regions *not* selected by outflows, which have a lower SiO detection rate, and that our SiO abundance increases with source luminosity, we suggest that the SiO, in the 14 sources in which it is detected, is being generated in the outflow. Previous, high resolution observations of SiO also suggest that SiO can be enhanced in the outflows from high mass stars (i.e. Beuther et al., 2004a,b) just as it is in the outflows from low mass stars.

The nine non-detections in our sample could be caused by beam dilution if these sources are on average further away. However, if we compare the distances for sources with and without SiO detections, we find average distances of 6.3 ± 4.4 and 4.4 ± 2.5 kpc, respectively. Thus, the non-detections cannot

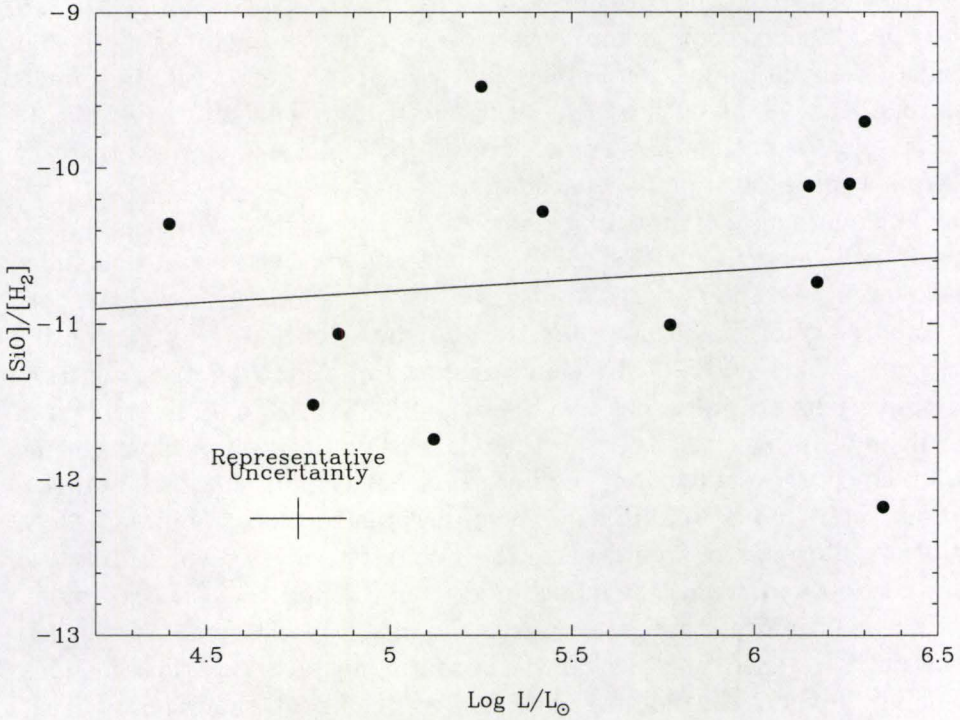

Figure 2.5: SiO abundance plotted as a function of source luminosity. The line of best fit shown is given by ($\log([SiO]/[H_2])=0.14\pm0.06\log(L/L_\odot)-11.5\pm$0.3), and was calculated only for sources detected in SiO. This is contrary to what is expected for SiO produced in PDRs, suggesting the observed SiO is produced in outflows.

be attributed to larger average source distances and so beam dilution can play only a minimal role in the non-detections of SiO.

If these SiO non-detections are not due to distance effects, there must be some local phenomenon which can explain why SiO is not being detected in regions known to contain protostellar outflows. It is possible that the Si is evolving into different species and the SiO abundance is dropping back down to dark cloud values. Pineau des Forets et al. (1997) suggest that a few$\times 10^4$ yr after the Si is liberated from dust grains and forms SiO, it can either freeze out back onto dust grains or oxidize and form SiO_2. Thus, the lack of SiO may be due to silicon moving into other species if it was liberated more than 10^4 yr ago. This interpretation implies that we did not detect SiO in some of our sources because the outflow generating mechanism shut off more than 10^4 years ago, and the outflow observed in HCO^+ (or in other molecules by other authors) is a remnant of previous accretion.

The kinematic ages of nine of our sources are listed in the Wu et al. (2004) catalog of high velocity outflows. Of these nine sources, five were also included in the P97 and S03 studies. This results in five sources for which we have both the kinematic age of the outflow, and the abundance of SiO. The relationship between outflow age and SiO abundance is shown in Figure 2.6 along with the model predictions of Pineau des Forets et al. (1997). With only five points, it is difficult to draw conclusions about the relationship between outflow age and SiO abundance, especially given the uncertain beam filling factor. At higher resolution, these points would likely move upwards to higher abundances. A larger beam filling factor would move the points for the two young outflows (G5.89 and Cep A) towards the model predictions. As for the other three outflows, this would move them further from the model predictions. We suggest that the outflow generating mechanism is continuing to shock these regions, replenishing the SiO. The oldest of these sources (G192.58) shows an infall signature in HCO^+, which also suggests that the outflow is still being powered.

2.3.2 Source Properties Derived from HCO^+ Observations

Given the large average distance to our sources (5.7 kpc), our 15″ beam subtends an average linear distance of 0.4 pc. Thus, it is quite likely that the HCO^+ emitting region does not entirely fill our single JCMT beam. In general we can determine the beam filling factor, f, for each source using

$$T_L = f_{\text{source}} T_s (1 - e^{-\tau}) \tag{2.2}$$

where T_L is the line brightness temperature measured at the telescope (corrected for telescope efficiencies) and T_s is an approximation to the ambient temperature (44 K) which is valid at densities greater than $\sim 10^3$ cm^{-3} Rholfs

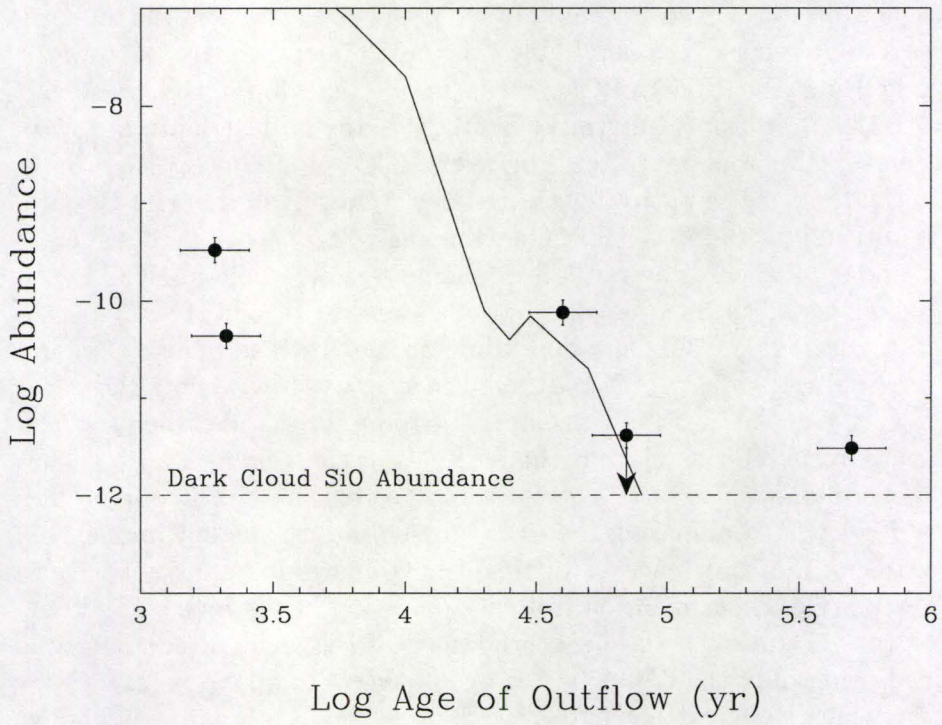

Figure 2.6: SiO abundance plotted as a function of outflow age. The outflow ages were taken from Wu et al. (2004). The solid line shows the model predictions of Pineau des Foréts et al. (1997) for the SiO abundance as a function of age (assuming Si returns to the dust grains), and the dashed line represents the canonical dark cloud abundance of SiO. The source shown with a downwards arrow represents G61.48, a source in which we did not detect SiO, and the value given is an upper limit to the SiO abundance. The error bars represent 30% calibration uncertainty between our observations and those of P97 and S03

& Wilson (2004). In a number of our sources, the HCO^+ is asymmetric, and thus cannot be consistently used to determine a beam filling factor. Instead, we can use the optically thin $H^{13}CO^+$ line, and we can simplify the above equation to $f = T_L/(T_s\tau)$. These values are shown in Table 2.3.

HCO^+ becomes optically thick quite quickly due to its relatively high abundance with respect to H_2 ($[HCO^+]/[H_2] \sim 10^{-8}$), and as such, can be used to roughly trace outflow and to trace infall (i.e. Myers et al., 1996) if the line profile shows a double peak. We determined the optical depth of HCO^+ towards each source using Equation 1 of Choi et al. (1993), and found that in all but one case (G139.9), it is optically thick. In all cases, the optical depth of HCO^+ is less than 77 (the abundance ratio between HCO^+ and $H^{13}CO^+$ Wilson & Rood, 1994), resulting in optically thin $H^{13}CO^+$ towards all sources. Because HCO^+ is optically thick in its line center, the line wings can be used to detect outflows, and so, if there is an outflow, it should be detectable in HCO^+ even if it goes undetected in SiO. Gaussian profiles were fit to our HCO^+ spectra (either single or double Gaussians, depending on the observed line shape), and the fits were subsequently subtracted from the spectra to leave only the residual outflowing gas. When using two Gaussians to fit the self absorbed spectra, we employed a method similar to the single Gaussian fitting of Purcell et al. (2006) because we used the sides of the detected lines to fit our profiles (see their Figure 3). Comparing the two Gaussian fits to single Gaussian fits showed no significant differences in distinguishing line wing intensity. Because of the possibility of contamination from SO_2 emission in the blue shifted outflow wing (at -17 km s^{-1}), the peak brightness of the residual emission was determined using only the red shifted wing emission. In all cases (except for G10.47 for which we could not find a linear baseline), we found a minimum of a 5σ peak brightness temperature in the residual line wing emission, with 19 of our sources having a minimum of a 10σ peak. This result suggests that we can detect outflow motions in all sources using our detections of HCO^+, despite not detecting SiO towards every source.

Our observations show that for ten of our sources, the spectral line profile of the HCO^+ emission has a double peak. This profile could either be due to self absorption of the optically thick HCO^+ line or from multiple velocity components within our $15''$ beam. To break this degeneracy, we observed the optically thin $H^{13}CO^+$. If the $H^{13}CO^+$ line has a single peak at the same velocity as the HCO^+ absorption feature, then it is likely that the HCO^+ line is self absorbed. If, however, the $H^{13}CO^+$ also has two peaks, and they are at approximately the same velocities as the two HCO^+ peaks, it would suggest that there are multiple components within the beam. Of our ten sources with double HCO^+ peaks, only one shows a double peak profile in $H^{13}CO^+$ (G20.08). This results in nine sources with double peaked optically thick HCO^+.

In addition to the nine optically thick sources, similar line asymmetries

appear in a number of other sources. However, in these sources, there is no clear emission gap producing a double peak profile, only an emission shoulder (i.e. De Vries & Myers, 2005). If we take G75.78 as an example, the HCO^+ line peak is red shifted from the rest velocity of the source, with a blue shifted emission shoulder.

There are a number of different kinds of source dynamics that can lead to the double peaked line profiles seen in our spectra, such as infall, outflow and even rotation. However, infall is the only one of these processes which would produce line asymmetries which are consistently blue (i.e. the blue peak is higher than the red peak or shoulder). If these profiles were due to outflow or rotation, there would be no statistical reason to have more sources with higher blue peaks than red peaks. Many previous studies have investigated the statistical significance of using this type of optically thick blue line asymmetry to trace infall as opposed to other dynamical motions; i.e. Mardones et al. (1997) and Gregersen et al. (1997) for low mass star forming regions, and Fuller et al. (2005) for high mass star forming regions.

Of the 10 sources in our survey which have double peaked HCO^+ profiles, we suggest eight may be indicative of infall. The other two sources are G20.08 and G45.47. G20.08 has already been shown to have multiple components in the beam from the double peaked $H^{13}CO^+$ profile, and G45.47 has a brighter red peak than blue. There are two additional sources (G19.61, and G240.3) in which HCO^+ has a strong red shifted shoulder, which we suggest may also be tracing infall. This analysis gives a total of ten infall candidates in our sample of 23 sources.

A recent survey of HCO^+ (J=1-0) towards sources with methanol masers shows an even distribution of sources with blue and red line asymmetries, and a higher percentage of self absorbed lines than in our study (Purcell et al., 2006). Of the six sources which overlap between our survey and that of Purcell et al, all six are self absorbed in HCO^+ (J=1-0). Five of them have blue line asymmetries consistent with infall, while only one (G31.41) has its red peak brighter than its blue peak. We only find self-absorption in HCO^+ (J=4-3) for three of these six sources. In two of the sources for which we do not see a clear self-absorption feature, we do see evidence for a red shifted shoulder which may be showing unresolved infall.

The sources in Purcell et al. (2006) have an even distribution of red and blue line asymmetries, while we have a clear bias towards detecting blue line asymmetries. This comparison could suggest that the higher energy J=4-3 transition of HCO^+ is a better tracer of infalling gas because it does not self absorb as readily as the J=1-0 transition.

For each of the 8 sources with blue, double peaked HCO^+ profiles, we can determine an infall velocity ($v_{\rm in}$) using the two layer radiative transfer model of Myers et al. (1996). Using their equation 9, we find infall velocities for all

eight double peaked infall sources (Table 2.4). The mass infall rate can then be determined using:

$$\dot{M} = \frac{dM}{dt} \approx \frac{M}{t} = \frac{\rho V v_{\rm in}}{r_{\rm gm}} = \frac{4}{3}\pi n_{\rm H_2} \mu m_{\rm H} r_{\rm gm}^2 v_{\rm in} \tag{2.3}$$

where μ is the mean molecular weight ($\mu = 2.35$), the geometric mean radius ($r_{\rm gm}$) is the unresolved circular radius of the HCO^+ emitting region derived from the beam radius and the beam filling factor ($r_{\rm gm} = \sqrt{f} r_{\rm beam}$), and $n_{\rm H_2}$ is the ambient source density. For seven of the sources in Table 2.4, the ambient density was determined by either P97, Hofner et al. (2000), or Wang et al. (1993). We could not find the ambient density for the eighth source (G192.58). From this analysis, we determine mass infall rates ranging from $1{\times}10^{-2}$ to $2{\times}10^{-5}$ $M_\odot$ yr^{-1}. These values are slightly higher than those generally observed for low mass star forming regions, but are consistent with the accretion rates derived for high mass star forming regions by McKee & Tan (2003). Since outflow rates are orders of magnitude higher in high mass star forming regions (i.e Beuther et al., 2002) it is not unreasonable to suggest that infall rates are also much higher in these regions.

The mass outflow rate for only one of these sources (Cep A) can be determined from the Wu et al. (2004) survey of high velocity outflows by dividing the mass in the outflow by the kinematic age of the outflow. We find the ratio of the mass outflow rate to the mass infall rate to be $\dot{M}_{\rm out}/\dot{M}_{\rm in} \approx 16$. This value is only slightly higher than values seen in other high mass star forming regions (i.e. Behrend & Maeder, 2001). Also, models suggest that a mass equivalent to 20-30% of the mass accreted onto a protostar is ejected as a wind (i.e. Pelletier & Pudritz, 1992; Shu et al., 1994), and that this wind entrains 5-20 times its mass in the outflow (Matzner & McKee, 1999).

2.3.3 Source Properties Derived from mapping G45.07

At a distance of 9.7 kpc, G45.07 is one of our furthest sources. This source was known from previous observations to have multiple continuum sources (De Buizer et al., 2003, 2005). The three continuum sources were observed in the mid-Infrared (MIR) and all three fall within 6″ of our map center. A fairly young outflow has also been mapped at high resolution (< 3″ synthesized beam) in CO and CS towards this region (Hunter, 1997). They observed a bipolar outflow with a position angle of -30° (east of north), as well as a red shifted absorption feature in their CS observations which they take to be indicative of infall.

Due to the large distance to this source, we should be able to detect all of the emission associated with this source in a fairly small map. In the left panel of Figure 2.7 we present a map of the SiO (contours) and $H^{13}CO^+$

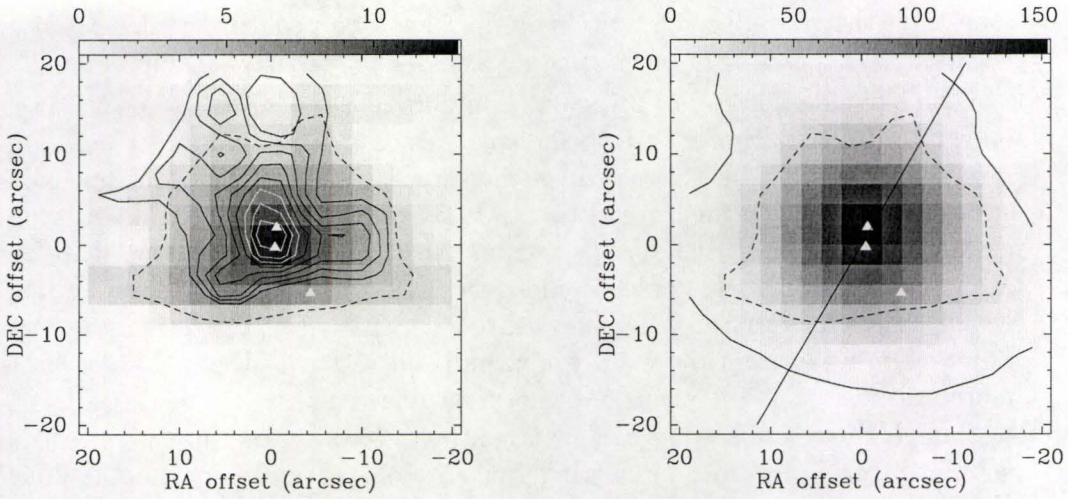

Figure 2.7: **Left:** SiO and $H^{13}CO^+$ towards G45.07. The halftone scale represents the integrated $H^{13}CO^+$ emission, while the contours show the integrated intensity of SiO. The velocity range used to determine the integrated intensities is the same as the single pointing velocity range (dv), however the rms noise limits are those listed at the end of Section 2. The first SiO contour is 5σ (3.2 K km s^{-1}), incrementing in steps of 2σ, with the same scale continuing into the white contours near the center. **Right:** HCO^+ integrated intensity towards G45.07. The solid contour represents the 5σ emission for the HCO^+ emission (3.5 K km s^{-1}), and the solid line represents the cut used for the PV diagram along the outflow axis (PA = -30°) presented in Figure 2.8. For both panels, the dashed line represents the 5σ $H^{13}CO^+$ emission contour (3.0 K km s^{-1}). The three triangles represent the Mid IR sources detected by De Buizer et al. (2005).

(halftone) emission in this region. The right panel of Figure 2.7 shows the HCO^+ emission. In both figures, the 5σ (2.1 K km s^{-1}) $H^{13}CO^+$ emission contour is plotted as a dashed line to help guide the eye. The first contour for SiO in the left panel and only contour of HCO^+ in the right panel are also 5σ (2.2 and 3.5 K km s^{-1} respectively). The differences in the 5σ contour levels for each tracer come from the different single channel rms levels between the two tunings, and the width of each line as given in Table 2.3. Also plotted in both figures are the three MIR continuum sources observed by De Buizer et al. (2003, 2005).

If we did not have the added information provided by this map, there would be two main conclusions we could draw from our single pointing observations towards this source. The first is that the enhanced blue emission in all three tracers suggests that our pointing is observing more of the blue shifted outflow

lobe than the red. Second, since we only have one peak in the spectrum of each tracer, there is only one source and we cannot classify it as infalling.

The left panel of Figure 2.7 shows contours of SiO emission superimposed on the $H^{13}CO^+$ halftone. With beam spacings of 5″, these maps are oversampled; however we note that much of the structure in the SiO emission is on scales comparable to the size of the JCMT beam. For instance, the structure at $\Delta\alpha = -10''$, $\Delta\delta = 0''$ is offset from the map center by more than the radius of our beam and could be independent from the emission at the map center. There is also SiO emission at $\Delta\alpha = 5''$, $\Delta\delta = 15''$, which is more than a full beam away from the map center, and suggests that the SiO emission is more extended that the primary beam of our observations. In fact, it appears as though there is a second SiO emission peak towards the upper left of the left panel of Figure 2.7. Interestingly, there does not appear to be as much $H^{13}CO^+$ emission at this northern position. This comparison shows that the SiO and $H^{13}CO^+$ lines are tracing different gas populations in this region. The excess SiO emission is offset from the map center in the same direction as the CO emission shown in Hunter (1997) at much higher resolution.

The right panel of Figure 2.7 shows the HCO^+ emission for this region. It appears that the HCO^+ emission extends much further than the SiO emission, suggesting it is tracing the larger scale envelope material. The line through the middle of this plot indicates the cut taken for the position-velocity (PV) diagram along the outflow axis as described by Hunter (1997).

The two panels of Figure 2.8 show the PV diagrams for SiO and HCO^+ in our maps both perpendicular and parallel to the outflow axis defined by Hunter (1997). Our single pointing HCO^+ spectrum (Figure 2.4) suggests we are observing more blue shifted outflow emission than red shifted emission; however, from our PV diagrams, we see that there is excess blue emission at all positions in our map. This excess blue emission cannot be due to outflow alone; instead, it could be due to an inherent velocity shift between the three continuum sources in our beam. We can, in fact, fit three Gaussian components to most of our HCO^+ spectra. These Gaussians peak at velocities of 60, 52 and 44 km s^{-1}, with the peak temperature for each component decreasing with velocity. The third component (at 44 km s^{-1}) could not be fit at all positions because it was intrinsically weaker than the other two peaks, and was lost in the noise towards the edges of the map. It appears as though this third component might be contamination from SO_2, which should occur at an apparent velocity of 41 km s^{-1} (or -17 km s^{-1} in Figure 2.4).

Perpendicular to the outflow axis, the mean velocity of the HCO^+ line peak appears to shift from $\sim$ 58 km s^{-1} at an offset of $+15''$ from the source center to $\sim$ 61 km s^{-1} at an offset of $-15''$ from the source (Figure 2.8). Given our velocity resolution (1.08 km s^{-1}) and spatial resolution (15″), is unclear whether this velocity shift is real. If it is, it could indicate large scale ($\sim$ 1.4

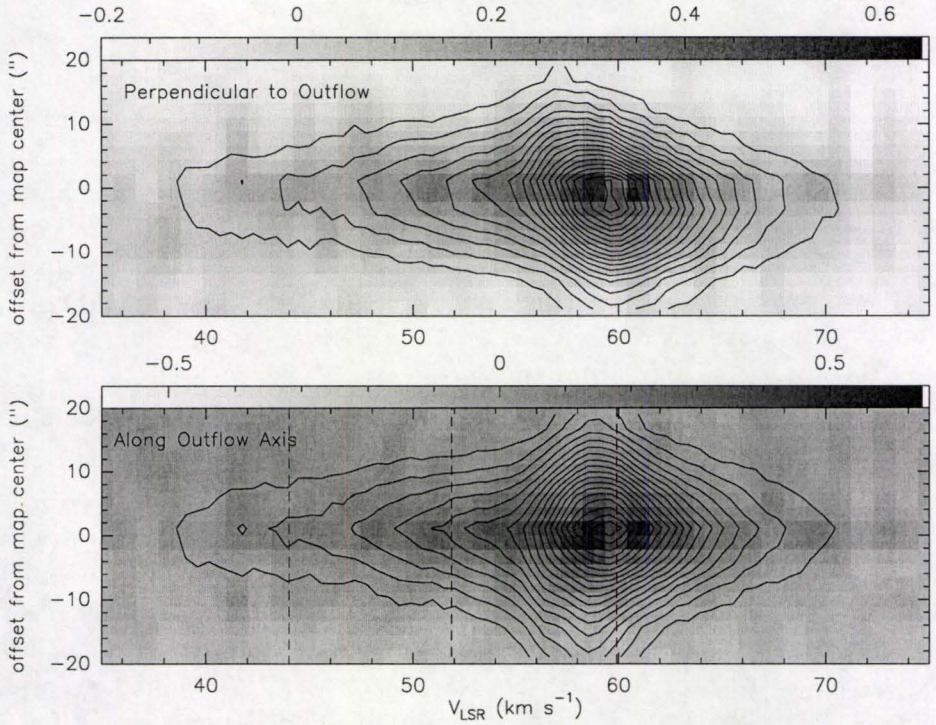

Figure 2.8: Position-Velocity (PV) diagrams for SiO (halftone scale) and HCO^+ emission (contours) in G45.07 both perpendicular to (top panel) and along the outflow axis (bottom panel) as defined in Hunter et al. (1997). These PV diagrams were taken at positions angles of 60° and -30° east of north respectively, with the cut for the bottom panel of this figure shown in the right panel of Figure 2.7. The first contour for HCO^+ is 5σ, or 0.7 K since the rms noise limit for this map is 0.14 K, and the contours increase in increments of 5σ. The three dashed lines in the bottom panel show the peak velocities of the Gaussian fits to the HCO^+ spectra.

pc) rotation within the core, on a much larger scale than would be expected for a rotating accretion disk.

2.3.4 Correlations Between Datasets

Previously, we discussed the reasons why we do not detect SiO towards a number of our sources, and have calculated the mass infall rates for the sources with double peaks in their HCO^+ emission, but we have not yet discussed the correlations between the two species. In Figure 2.9 we plot the logarithm of the abundance of $H^{13}CO^+$ against the same quantity for SiO (open circles), as well as the column densities of both species (filled circles). The abundance of $H^{13}CO^+$ was calculated in the same manner as the abundance of SiO described above (using the CS column density from P97 and the CS abundance from S03). The probability of obtaining these correlations if the data are, in fact, uncorrelated is 6×10^{-3} for the abundances, and 2×10^{-4} for the column densities.

As stated earlier, SiO is a well known shock tracer, and as such, an increased abundance of SiO would suggest more shocked material within our 15″ beam. The (generally) infall tracing HCO^+ has been shown by some authors to be destroyed in strong shocks (i.e. Bergin et al., 1998; Jørgensen et al., 2004). However, Wolfire & Koenigl (1993) suggest that HCO^+ can be enhanced in regions with high energy shocks, where electron abundances are much greater. This enhancement in the electron abundance increases the formation rate of ions, and we suggest that this is responsible for the $H^{13}CO^+$ abundance enhancement in our sources. This correlation between the abundances of $H^{13}CO^+$ and SiO suggests that HCO^+ and $H^{13}CO^+$ are not only tracing infalling gas, but also the outflowing gas as well. This conclusion is supported by the strong, and broad, line wing emission detected in HCO^+ (See Section 2.3.2).

HCO^+ over abundances have been seen in high mass star forming regions not included in this study like NGC 2071 (Girart et al., 1999) and Orion IRc2 (Vogel et al., 1984). In these two papers, the over abundances of $H^{13}CO^+$ are with respect to ambient cloud tracers such as CO and H_2, rather than the high density or shock tracers like the CS and SiO with which we are comparing our $H^{13}CO^+$ abundances. However, Viti & Williams (1999a,b) show that HCO^+ is indeed over abundant with respect to CS in the gas surrounding HH objects, and Jiménez-Serra et al. (2006) also show that the abundance of $H^{13}CO^+$ can be enhanced with respect to SiO by up to a factor of ten in the same regions ahead of HH objects.

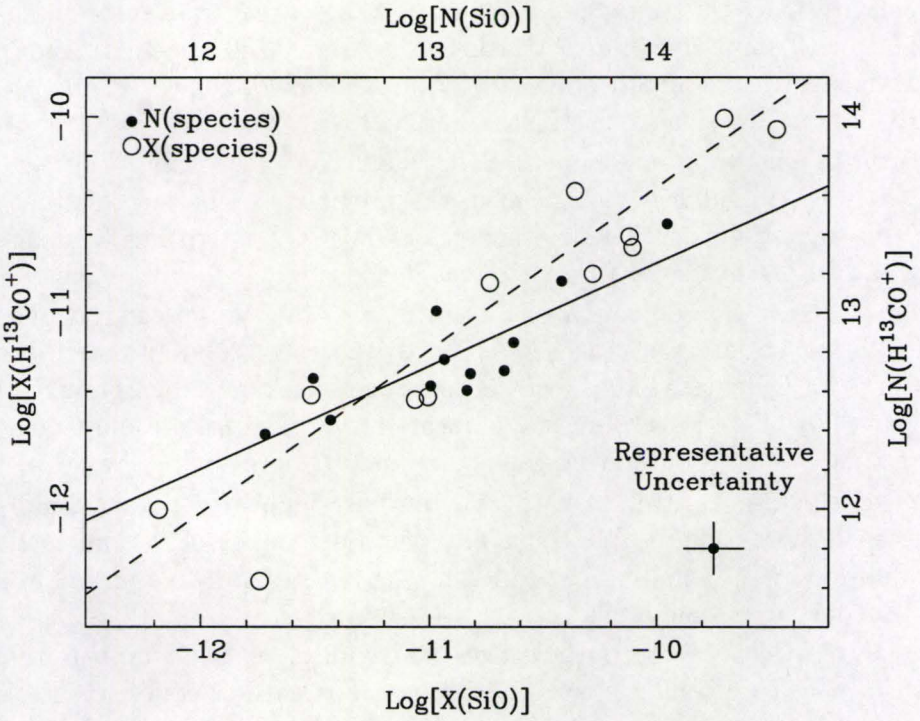

Figure 2.9: The abundance of $H^{13}CO^+$ with respect to the abundance of SiO (open circles, dashed line of best fit) appears to increase faster than the respective column densities of these two species (filled circles, solid line of best fit). The equations of the two lines of best fit are: $\log[X(H^{13}CO^+)]=(0.84\pm0.09)\log[X(SiO)]-(2.0\pm0.9)$, and $\log[N(H^{13}CO^+)]=(0.5\pm0.1)\log[N(SiO)]+(6\pm1)$. This relationship could be due to HCO^+ being enhanced (similarly to SiO), as discussed in the text.

2.4 Discussion and Conclusions

Without maps of each region, it is impossible to tell how much of the HCO^+ emission in the line center and in the line wings is due directly to infall and outflow motions; however, based on the arguments we have presented above, we suggest that ten sources show infall motions, and all 23 source show outflow motions based on the HCO^+ line profiles. We have found evidence for recent outflow activity (SiO emission) in 14 out of our 23 sources. Seven of these outflow and infall sources overlap. M17S, G192.6 and G240 appear to show only infall signatures and no SiO outflow signatures. They do, however, appear to have HCO^+ outflow signatures of a minimum of 8σ.

Detection of line wing emission in HCO^+ and the relationship between $H^{13}CO^+$ and SiO abundances described in the previous section suggest that while SiO is tracing outflow in most sources and HCO^+ is tracing infall in some sources, HCO^+ is also observable in the outflowing gas for all regions.

We find that the non-detection of SiO in nine of our sources is not due to beam dilution or larger average distances to the source, but possibly to older outflows for which the Si has likely either frozen back onto dust grains or evolved into SiO_2. For these sources, it appears that the accretion may have ceased, and the observed outflowing gas is a remnant of previous accretion.

We have found seven sources with SiO outflow signatures but no infall signatures in HCO^+. This result could be due to a number of factors such as beam dilution of the infalling gas which masks the spectral line profile we would expect for large scale infall.

It is possible that, as the outflow ages and widens, it may impinge on the region in which we could detect infalling gas. For outflow cones oriented along the line of sight, the younger, narrower outflows would have infalling gas with large line of sight velocities and be likely to produce an observable infall signature. However, for the older outflows which have widened, the largest infall velocities will be in the plane of the sky, and unobservable at the resolution of the JCMT. However, this effect would not be as pronounced for outflows in the plane of the sky (such as G5.89, for which we do not see an infall signature). It is difficult to assess the importance of this effect without detailed information on the outflow orientation in each source.

Thus, we suggest that some of these sources may have finished accreting, and what we observe are remnant outflows from a previous phase of accretion. This scenario was suggested by Klaassen et al. (2006) to explain the large scale outflow in G5.89, and this source is one of these seven sources with an SiO outflow and no apparent infall signature.

The seven sources which show recent outflow activity (those with SiO emission) and which appear to be undergoing infall are suggestive of ongoing accretion beyond the onset of the HII region. If accretion is ongoing in the

presence of an HII region, then it seems likely that this accretion flow may be ionized. This ionized accretion scenario could be similar to low angular momentum accretion with high ionization as suggested by Keto (2007). Thus, from this survey, we suggest that both models of ionized accretion and halted accretion may be important in describing the evolution of a massive protostar (or protostars) beyond the formation of an HII region.

Table 2.1: **Observed Sample of Massive Star Forming Regions.** The source velocity here is the reference velocity of each source, which has been removed from each spectrum. RMS noise levels are given in T_{MB}. References:(1) Hanson et al. 2002, (2) S03, (3) Kurtz et al. 1994, (4) Kumar et al. 2003., (5) Churchwell et al. 1990, and (6) Hofner et al. 2000

Name	Position (J2000)		RMS noise limit (K)		V_{LSR}	Distance		P92 Name[a]
	RA	DEC	347 GHz	356 GHz	(km/s)	(kpc)	ref	
G5.89	18 00 30.3	-24 03 58	0.060	0.111	9	2	1	W28A2 (1)
G5.97	18 03 40.4	-24 22 44	0.044	0.069	10	2.7	5	...
G8.67	18 06 19.0	-21 37 32	0.068	0.074	36	8.5	2	8.67-0.36
G10.47	18 08 38.4	-19 51 52	...[b]	0.100	67	12	2	W31 (1)
G12.21	18 12 39.7	-18 24 21	0.042	0.076	24	16.3	2	12.21-0.1
M17S	18 20 24.8	-16 11 35	0.044	0.077	20	2.3	5	M17 (2)
G19.61	18 27 38.1	-11 56 40	0.048	0.065	43	4.5	1	19.61-0.23
G20.08	18 28 10.4	-11 28 49	0.044	0.068	42	4.1	1	20.08-0.13
G29.96	18 46 03.9	-02 39 22	0.044	0.079	98	9	1	W43S
G31.41	18 47 33.0	-01 12 36	0.044	0.061	97	8.5	1	31.41+0.31
G34.26	18 53 18.5	01 14 58	0.047	0.131	58	3.7	1	W44
G45.07[c]	19 13 22.1	10 50 53	0.044	0.073	59	9.7	1	45.07+0.13
G45.47	19 14 25.6	11 09 26	0.037	0.063	58	8.3	6	...
G61.48	19 46 49.2	25 12 48	0.037	0.048	12	2	1	S88 B
K3-50A	20 01 45.6	33 32 42	0.035	0.077	-24	8.6	3	K3-50
G75.78	20 21 44.1	37 26 40	0.038	0.068	0	5.6	1	ON 2N
Cep A	22 56 17.9	62 01 49	0.031	0.076	-10	0.7	1	CEP A
W3(OH)	02 27 03.8	61 52 25	0.026	0.079	-48	2.4	2	W3 (OH)
G138.3	03 01 29.2	60 29 12	0.066	0.073	-38	3.8	1	S201
G139.9	03 07 23.9	58 30 53	0.058	0.071	-39	4.2	1	...
G192.58	06 12 53.6	17 59 27	0.037	0.053	9	2.5	3	S255/7
G192.6	06 12 53.6	18 00 26	0.074	0.098	9	2.5	3	S255/7
G240.3	07 44 51.9	-24 07 40	0.035	0.048	68	6.4	4	...

[a]Name given to source in Plume et al. (1992). When included in P97 and S03 these were the source names used.

[b]Too much chemistry in spectrum to determine a reliable rms noise level.

[c]The rms noise limits for the two maps of this source are 0.1 K and 0.14 K for the 347 GHz and 356 GHz pointings respectively.

Table 2.2: **Integrated Intensities for SiO, HCO^+ and $H^{13}CO^+$.**For the sources in which we did not detect SiO or $H^{13}CO^+$, 3σ upper limits on the brightness temperature and integrated intensities are given.

Name	SiO Properties			HCO^+ Properties			$H^{13}CO^+$ Properties		
	T_{MB}	$\int T_{MB} dv$	dv	T_{MB}	$\int T_{MB} dv$	dv	T_{MB}	$\int T_{MB} dv$	dv
G5.89	2.3	75.3±0.7	120	39.2	690.0±0.8	105	8.9	65.2±0.4	35
G5.97	<0.1	<0.3±0.1	8	12.4	50.5 ±0.2	15	0.6	1.6 ±0.1	8
G8.67	0.2	1.6 ±0.3	13	13.8	80.0 ±0.3	38	5.6	20.9±0.2	10
G10.47	1.0	9.9 ± ...	22	7.7	79.3 ±0.4	35	1.2	9.2 ± ...	15
G12.21	0.2	2.5 ±0.2	25	10.0	93.8 ±0.3	30	0.8	6.5 ±0.2	15
M17S	<0.1	<0.7±0.2	15	16.2	79.0 ±0.2	15	2.9	9.4 ±0.2	11
G19.61	0.8	15.9±0.3	45	10.8	162.2±0.4	55	1.8	16.1±0.2	20
G20.08	0.4	6.9 ±0.3	40	6.5	75.0 ±0.3	40	1.1	9.7 ±0.2	25
G29.96	0.5	7.9 ±0.3	40	23.6	160.4±0.3	30	3.8	13.2±0.1	10
G31.41	<0.1	<0.7±0.2	15	1.6	6.8 ±0.2	13	<0.1	<0.3±0.1	3
G34.26	1.3	26.0±0.4	55	27.8	228.2±0.6	35	4.3	33.2±0.2	25
G45.07	0.7	10.3±0.3	37	15.0	169.4±0.4	45	1.5	11.2±0.3	33
G45.47	<0.1	<0.3±0.1	12	10.1	59.4 ±0.2	20	1.3	6.1 ±0.1	12
G61.48	<0.1	<0.3±0.1	8	10.8	58.5 ±0.1	18	1.5	4.7 ±0.1	8
K3-50A	0.3	2.1 ±0.1	16	18.6	154.8±0.3	25	1.8	10.6±0.2	18
G75.78	0.3	2.2 ±0.1	13	12.5	136.8±0.3	45	2.5	10.3±0.2	17
Cep A	0.5	7.3 ±0.2	45	23.2	234.7±0.4	60	4.5	23.4±0.2	28
W3(OH)	1.4	14.5±0.2	50	18.5	148.2±0.3	30	2.4	11.6±0.1	15
G138.3	<0.2	<0.3±0.1	2	5.0	10.6 ±0.2	8	0.3	0.5 ±0.1	4
G139.9	<0.2	<0.3±0.1	11	8.6	18.8 ±0.1	6	<0.2	<0.3±0.1	2
G192.58	0.3	1.3 ±0.1	8	14.5	84.2 ±0.2	25	1.1	5.5 ±0.1	15
G192.6	<0.2	<0.6±0.2	30	12.0	54.1 ±0.3	15	0.8	2.2 ±0.2	8
G240.3	<0.1	<0.4±0.2	10	7.3	59.1 ±0.2	30	0.4	2.5 ±0.1	14

Table 2.3: **Observed and Derived Source Parameters.**

Name	Detection		f^a	Col. Dens ($\times 10^{12}$)		[SiO]/[H_2]^b	L_{FIR}	Age^c
	SO_2	Infall		$H^{13}CO^+$	SiO		Log($L_\odot$)	(10^4 yr)
G5.89	Y	N	0.79	28.5	110.1	-9.48	5.25^d	0.2
G5.97	N	N	0.28	0.7	<0.4	...	5.23^d	...
G8.67	Y	Y	0.24	9.1	2.4	...	5.70^d	...
G10.47	Y	Y	0.16	4.0	14.6	-10.11	6.26^d	...
G12.21	Y	N	0.22	2.8	3.7	-10.74	6.17^d	...
M17S	N	Y	0.33	4.1	<1.0	<-11.31	5.72^d	...
G19.61	Y	Y	0.22	7.0	23.3	-10.28	5.42^d	...
G20.08	Y	N	0.13	4.2	10.1	-11.06	4.86^d	...
G29.96	Y	N	0.49	5.7	11.6	-9.71	6.30^d	...
G31.41	N	N	...	<0.1	<1.0	<-12.47	5.45^d	...
G34.26	Y	Y	0.58	14.5	38.2	-11.01	5.77^d	...
G45.07	Y	N	0.32	4.9	15.1	-10.12	6.15^d	4
G45.47	Y	N	0.21	2.7	<0.4	...	6.04^d	...
G61.48	N	N	0.23	2.1	<0.4	<-11.39	5.01^d	7
K3-50A	Y	N	0.40	4.6	3.1	-12.18	6.35^e	...
G75.78	Y	N	0.25	4.5	3.2	...	5.65^d	3.7
Cep A	Y	Y	0.47	10.2	10.7	-10.36	4.40^f	0.2
W3(OH)	Y	Y	0.39	5.1	21.3	-11.74	5.12^e	...
G138.3	N	N	0.11	0.2	<0.4	...	4.57^e	17
G139.9	N	N	...	<0.1	<0.4	...	4.82^e	6
G192.58	Y	Y	0.32	2.4	1.9	-11.52	4.79^e	50
G192.6	Y	Y	0.26	1.0	<0.9	...	...	...
G240.3	Y	Y	0.16	1.1	<0.6	...	...	2.3

[a] HCO^+ beam filling factor.

[b] SiO abundance relative to H_2 for sources with CS observations (P97) and abundance calculations (S03).

[c] Kinematic age of outflow from Wu et al. (2004).

[d] Far Infrared Luminosities modified from Wood & Churchwell (1989).

[e] Far Infrared Luminosities modified from Kurtz et al. (1994).

[f] Far Infrared Luminosities taken from Evans et al. (1981).

Table 2.4: **Infall Velocities and Mass Infall Rates.**

Name	V_{in}[a] (km s^{-1})	n_{H_2}[b] (10^5 cm^{-1})	$\dot{M}_{in}$[c] (10^{-4} $M_\odot$ yr^{-1})
G8.67	0.4 ± 0.1	1.8	4±2
G10.47	1.8 ± 0.3	7.2	100±80
M17S	1.4 ± 0.5	5.0	4±2
Cep A	0.23±0.07	10.0	0.17±0.07
W3(OH)	0.06±0.02	60.0	3±1
G192.58	0.8 ± 0.3	...	...
G192.6	0.9 ± 0.4	4.0	2±1
G34.26	1.5 ± 0.3	3.6	14±4

[a]Infall velocities for sources with double peaked HCO^+ profiles.
[b]Ambient densities taken from P97 except for G34.26 (Hofner et al. 2000), M17S (Wang et al. 1993).
[c]Mass infall rates.

Chapter 3

Outflow and Infall in a Sample of Massive Star Forming Regions II: Large Scale Kinematics

This chapter has previously been published by the Astrophysical Journal as an article titled "Outflow and Infall in a Sample of Massive Star-forming Regions." by P.D. Klaassen, and C.D Wilson (The Astrophysical Journal, Scheduled for Volume 684 Issue 2 pp. 1273-1280). Reproduced with permission of the American Astronomical Society.

3.1 Introduction

In the last 20 years, the processes involved in the formation of solar type stars have been well characterized. An evolutionary sequence has been developed in which a prestellar core (i.e. Andre et al., 2000) begins to collapse under its own gravity and forms a Class 0 object (i.e. Andre et al., 1993) with a large disk of material surrounding it. This accreting protostar begins to produce an observable molecular outflow which releases the build up of angular momentum (i.e. Bachiller, 1996; Arce et al., 2007) and evolves into the Class 1 stage. Later, as the protostar becomes more revealed, accretion slows and a pre-main-sequence star forms. It then undergoes quasi-static contraction until core hydrogen burning commences and the star reaches the main sequence (i.e. Shu et al., 1987). These processes have been well studied and characterized based in part on the high resolution observations possible towards the closest examples of low mass star forming regions.

The initial mass function (IMF) of stars (i.e. Kroupa, 2001) shows that

most of the mass contained in stars is within the lower mass stars, and that massive stars do not form nearly as often as their lower mass counterparts. There are a number of nearby low mass star forming regions (i.e. Taurus, Ophiuchus, Chameleon, and Serpens are well studied nearby examples) in which there is no massive star formation. High mass stars do not, in general, form in isolation, but together with low mass stars (i.e. Orion, see Riddick et al., 2007). The high densities required for massive star formation also mean that more of them form in the molecular ring. This means that statistically, the closest examples of regions forming high mass stars are further away, and are also forming clusters of stars. Both distance and clustering can cause confusion when attempting to determine the dynamics in a region.

Add to the large average distances and source confusion the higher energies involved in the formation of massive stars and the presence of HII regions surrounding the more evolved massive protostars, and it becomes clear why high mass star formation is not nearly as well understood as lower mass star formation. If we assume that massive stars form in a manner similar to their lower mass counterparts (i.e. McKee & Tan, 2003), it is possible to suggest an evolutionary sequence starting from an Infrared Dark Cloud (i.e. Pillai et al., 2006) with a deeply embedded protostar which then begins to heat its surroundings and creates a hot core (i.e. Kurtz et al., 2000). The protostar then begins burning hydrogen brightly enough to ionize its surroundings, forming a hypercompact HII region (Keto, 2003), which continues to expand into an ultracompact HII region (Wood & Churchwell, 1989) as the protostar evolves towards and up the main sequence (Beuther & Shepherd, 2005; Keto & Wood, 2006). There are many observable phenomena, such as large scale infall and outflows, which appear to be common between both low and high mass star formation, which suggests that perhaps high mass stars may form via the accretion of matter onto a single object in a manner similar to low mass stars. However, for high mass star formation, there are still a number of questions to be answered. For the large scale phenomena observable with a single dish telescope, we still do not know how large an area the outflowing gas shocks, how much energy is required to shock these regions, how large the infall region is, or how much mass from the protostellar core undergoes infall onto the central massive object.

Here, we present follow-up observations to Chapter 2 with which we address the questions posed above for seven high mass star forming regions mapped using the James Clerk Maxwell Telescope[1]. In Chapter 2, we obtained single pointing observations towards 23 massive star forming regions previously known to have HII regions (Wood & Churchwell, 1989; Kurtz et al., 1994) and

[1]The James Clerk Maxwell Telescope is operated by The Joint Astronomy Centre on behalf of the Science and Technology Facilities Council of the United Kingdom, the Netherlands Organisation for Scientific Research, and the National Research Council of Canada.

molecular outflows as traced by CS (Plume et al., 1997; Shirley et al., 2003) or CO (Hunter, 1997). We were able to show that, of our observed high mass star forming regions with ongoing outflow activity (14 sources, as traced by SiO emission), half (seven) showed evidence for large scale infall motion as well (as traced by HCO^+ line asymmetries). We suggested that the sources with infall and outflow detections were still actively accreting material (possibly in an ionized form, like that discussed in Keto (2007), while the other half may have already finished accreting (like the source discussed in Klaassen et al., 2006). However, with single pointing observations, we could not determine the sizes of the infalling or shocked (outflowing) regions, and therefore could not discuss properties such as the extents of the infall and outflow regions, whether these phenomena were beam diluted, or how their sizes compared. In this paper, we present maps of seven sources in the same tracers as Chapter 2 in order to understand better the nature of the large scale infall and outflow towards massive star forming regions.

For this paper, we chose to map the SiO (J=8-7) and $HCO^+/H^{13}CO^+$ (J=4-3) emission towards seven massive star forming regions. Six sources were selected from Chapter 2, and were chosen to be representative of the survey as a whole. Two sources (G29.96-0.02 and G5.89-0.39) showed only outflow signatures, while two showed both infall and outflow signatures (G10.47+0.03 and G19.61-0.23), and one source (K3-50A) showed only a weak outflow signature. It was unclear whether the emission towards the sixth source (G20.08-0.14) was due to one cloud (as suggested by the single peaked SiO line profile) or two (as suggested by the double peaked HCO^+ and $H^{13}CO^+$ line profiles). The G20.08 region was previously known to have two ultracompact HII regions in close proximity (i.e. Sewilo et al., 2004), although the two HII regions are separated by more than a single JCMT beam. To this list of six sources, we added one more source, G10.6-0.4. This source was added to determine whether the ionized and molecular accretion observed on small scales in this region (i.e. Keto & Wood, 2006; Sollins et al., 2005) has a corresponding larger scale molecular infall signature. G10.6-0.4 will act as a good test for determining whether our large scale results reflect the smaller scale dynamics, since the small scale structures are fairly well understood for this region. From this point forward, all source names based on Galactic coordinates will be truncated to latitudes only.

In Section 3.2 we present our observations and in Section 3.3 we determine outflow and infall properties based on these observations. Our results are then discussed in Section 3.4, and we summarize in Section 3.5

3.2 Observations

Observations of SiO (J=8-7), HCO^+ and $H^{13}CO^+$ (J=4-3) were obtained at the JCMT towards G10.47, G10.62, G19.61, G20.08, G29.96 and K3-50A in April and August 2007 as project M06BC08 along with HCO^+ observations of G5.89. SiO (J=8-7) and $H^{13}CO^+$ were observed simultaneously towards G5.89-0.39 as part of project M03AC13 (see Klaassen et al., 2006, for a description of these observations) and taken from the JCMT archive for this study. The archive map is smaller than our new maps; however, both the SiO and $H^{13}CO^+$ emission falls below the rms limits within the edges of this map.

The spectral resolution of the new datasets is 0.42 km s^{-1}, the observations are spaced at 7″ to Nyquist sample the 14″ full width of the JCMT beam at these frequencies, and the main beam efficiency was 0.62. Map center positions and local standard of rest velocities are given for our six original sources in Chapter 2. For G10.6, these properties are as follows: α = 18:10:27.8, δ = -19:56:04, and V_{LSR} = 3 km s^{-1}. For reasons presented in Section 3.4.1, in this paper we adopt a distance of 5.8 kpc (i.e. Gibb et al., 2004) for G10.47, which is much closer than the value of 12 kpc (i.e. Shirley et al., 2003) used in Chapter 2.

The 2007 observations were obtained using HARP-B and the ACSIS autororrelator system in either grid position switching or jiggle position switching mode. Both methods provided similar noise limits in similar times. The noise levels in each map are given in the respective figure captions and were generally consistent across each map, staying within approximately 30% of a mean value when receivers with bad noise levels were removed from the maps. These observations were reduced using the Joint Astronomy Center Starlink software. The 2003 observations were obtained with RxB in raster mapping mode using the DAS autocorrelator system and reduced using SPECX. First order linear baselines were removed from each pixel within each map, and the reduced maps were exported to the MIRIAD format for analysis.

3.3 Results

SiO and HCO^+ were chosen for this study because they trace outflow and infall, respectively, in star forming regions on all mass scales. Once each map was properly calibrated and exported into MIRIAD, the peak brightness temperature and line full width at zero power (FWZP) were determined from the spectrum at the map pointing center. The uncertainty in the integrated intensity for each line was determined using $\Delta I = T_{rms}\Delta\nu(N_{chan})^{1/2}$ where T_{rms} is the single channel rms uncertainty, $\Delta\nu$ is the velocity resolution of our observations, and N_{chan} is the number of channels used to cover the full width of the line (FWZP). Note that for sources with self absorbed HCO^+ profiles, the peak

line temperature is an underestimate of the source brightness temperature.

In our maps, we find that the HCO^+ emission towards each source is extended, as is the $H^{13}CO^+$ emission; however, $H^{13}CO^+$ does not reach the same spatial scales as the 77 times more abundant (Wilson & Rood, 1994) HCO^+. In only five of our seven sources is the SiO emission at least marginally resolved. The deconvolved source size was determined using $D_{\rm sou} = \sqrt{D_{\rm obs}^2 - D_{\rm beam}^2}$ where the longest axis of the observed region full width at half maximum diameter ($D_{\rm obs}$) was used to compare to the beam diameter ($D_{\rm beam}$). Towards the two unresolved sources (K3-50A and G19.61), the deconvolved diameter of the emitting region is less than 50% of the JCMT primary beam, while the deconvolved diameter is greater than 70% of the JCMT primary beam towards our other sources. Our SiO detection is weak in K3-50A (the line peak was only detected at 3.5-4σ) and was insufficient for detecting SiO beyond the central pixel. This was not the case for G19.61 (the line peak was detected at 7σ), yet the SiO emission in this source was also unresolved. Thus, if the shocked region in G19.61 were as extended as our JCMT beam, we would have detected the extended SiO emission.

Emission maps for each source are shown in Figures 3.1-3.7. In each case, HCO^+ emission spectra are shown for pixels with HCO^+ integrated intensities which are 10σ or greater. For each tracer, the intensity scale for the HCO^+ spectra is constant for a given source, and the peak HCO^+ intensity for each source is listed in Table 3.2. The dashed contour in each plot represents the 3σ emission region for $H^{13}CO^+$ and the solid contours represent SiO emission, starting at 3σ and increasing in intervals of 3σ. The 3σ rms uncertainties in the integrated intensities are given in each figure caption. The star in each figure marks the position of the peak in the HCO^+ integrated intensity. In all cases except K3-50A and G29.96, the positions of the HCO^+ peak is within the same beam as the SiO peak. For the two remaining sources, this offset may be due to pointing errors between the two maps.

Using the FWZP from the central pixel, the integrated intensity for each species across each map was determined. The rms uncertainty in the integrated intensity was determined using the same method as presented in Chapter 2. For each tracer, the line is broadest in the map center, and so using the same FWZP across the entire map captures all of the emission from that transition. The integrated intensities averaged over each map in SiO and HCO^+ are shown in Tables 3.1 and 3.2, respectively.

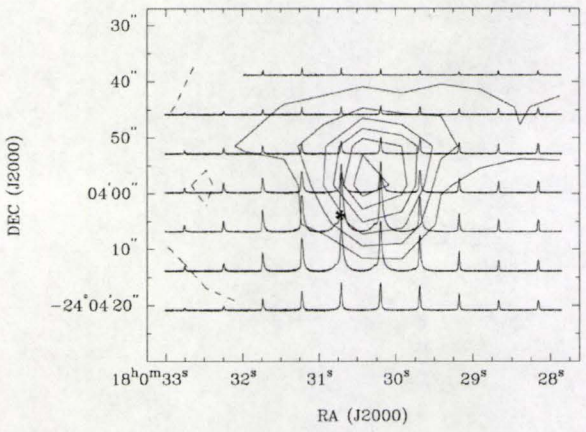

Figure 3.1: **G5.89-0.39** The solid contours represent integrated SiO emission towards G5.89. They start at 3σ (9.68 K km s^{-1}) and increase in steps of 3σ. The dashed contour is the 3σ (5.23 K km s^{-1}) contour of $H^{13}CO^+$ emission while the spectra represent the HCO^+ emission where the integrated intensity is above 10σ (14.50 K km s^{-1}) from -50 to 80 km s^{-1}.

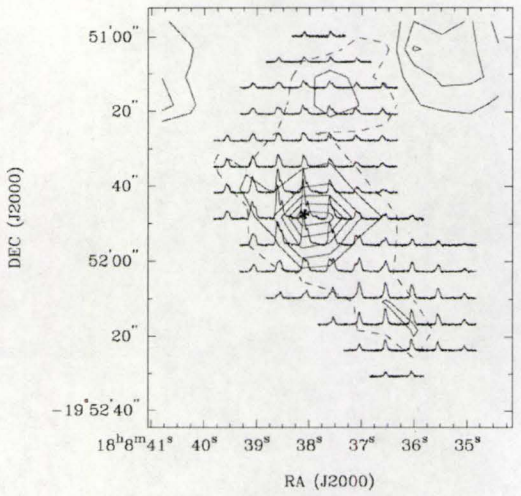

Figure 3.2: **G10.47+0.03** The solid contours represent integrated SiO emission towards G10.47. They start at 3σ (1.14 K km s^{-1}) and increase in steps of 3σ. The dashed contour is the 3σ (0.75 K km s^{-1}) contour of $H^{13}CO^+$ emission while the spectra represent the HCO^+ emission where the integrated intensity is above 10σ (10.00 K km s^{-1}) from 45 to 90 km s^{-1}.

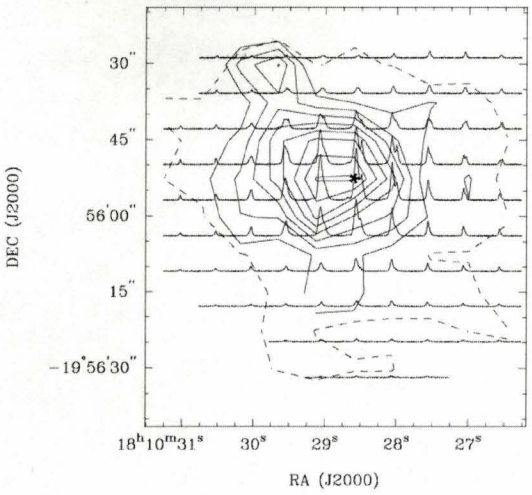

Figure 3.3: **G10.62-0.38** The solid contours represent integrated SiO emission towards G10.6. They start at 3σ (1.01 K km s^{-1}) and increase in steps of 3σ. The dashed contour is the 3σ (1.13 K km s^{-1}) contour of $H^{13}CO^+$ emission while the spectra represent the HCO^+ emission where the integrated intensity is above 10σ (8.55 K km s^{-1}) from -30 to 30 km s^{-1}.

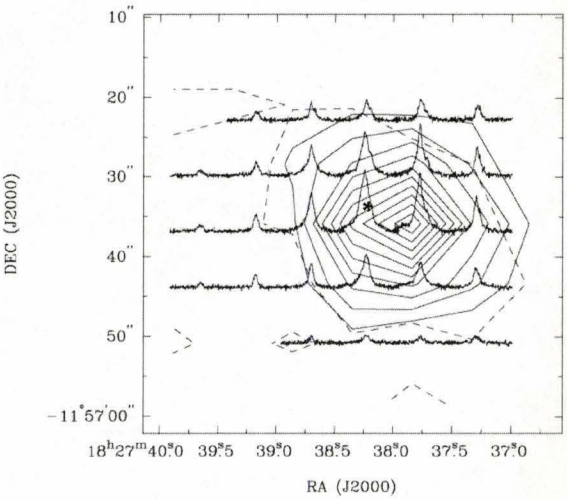

Figure 3.4: **G19.61-0.23** The solid contours represent integrated SiO emission towards G19.61. They start at 3σ (1.35 K km s^{-1}) and increase in steps of 3σ. The dashed contour is the 3σ (0.9 K km s^{-1}) contour of $H^{13}CO^+$ emission while the spectra represent the HCO^+ emission where the integrated intensity is above 10σ (8.39 K km s^{-1}) from 10 to 80 km s^{-1}.

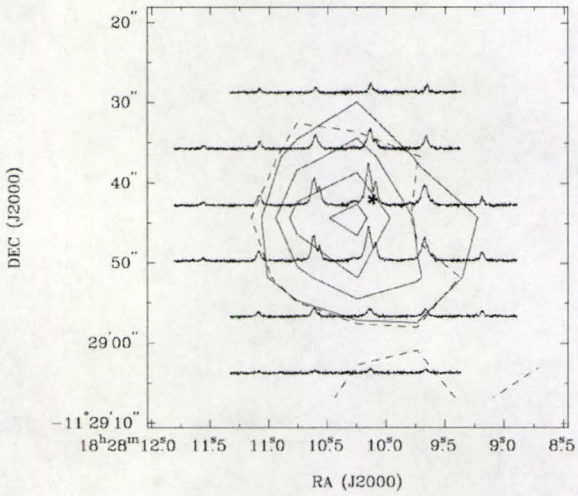

Figure 3.5: **G20.08-0.14** The solid contours represent integrated SiO emission towards G20.08. They start at 3σ (1.10 K km s^{-1}) and increase in steps of 3σ. The dashed contour is the 3σ (0.90 K km s^{-1}) contour of $H^{13}CO^+$ emission while the spectra represent the HCO^+ emission where the integrated intensity is above 10σ (8.23 K km s^{-1}) from 10 to 80 km s^{-1}.

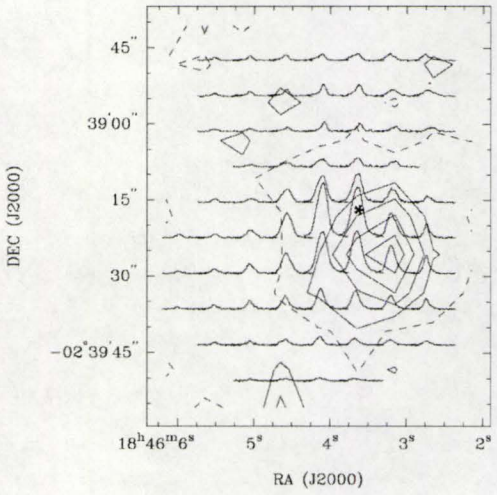

Figure 3.6: **G29.96-0.02** The solid contours represent integrated SiO emission towards G29.96. They start at 3σ (1.53 K km s^{-1}) and increase in steps of 3σ. The dashed contour is the 3σ (0.76 K km s^{-1}) contour of $H^{13}CO^+$ emission while the spectra represent the HCO^+ emission where the integrated intensity is above 10σ (6.3 K km s^{-1}) from 90 to 110 km s^{-1}.

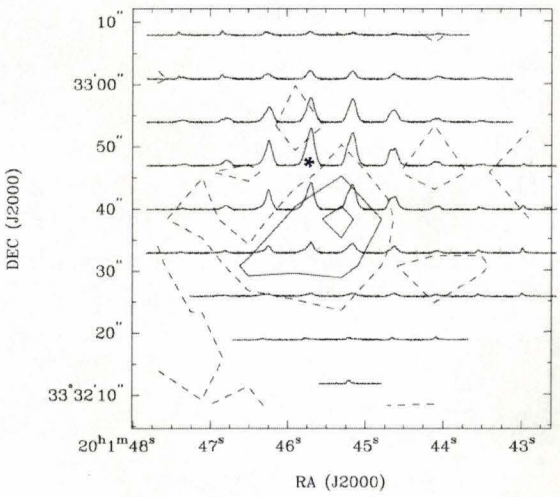

Figure 3.7: **K3-50A** The solid contours represent integrated SiO emission towards K3-50A. They start at 3σ (1.15 K km s^{-1}) and increase in steps of 3σ. The dashed contour is the 3σ (1.00 K km s^{-1}) contour of $H^{13}CO^+$ emission while the spectra represent the HCO^+ emission where the integrated intensity is above 10σ (5.97 K km s^{-1}) from -50 to 0 km s^{-1}.

Table 3.1: SiO Observations and Derived Outflow Properties

Source	Dist (kpc)	T_{mb} (K)	FWZP[a] (km/s)	X[SiO]	$\int T^*_{mb} dv$ (K km/s)	$\log[N_{SiO}]$ (cm^{-2})	$\log[N_{H_2}]$ (cm^{-2})	Mass ($M_\odot$)	Radius[b] ($\times 10^{17}$ cm)	L ($L_\odot$) ($\times 10^3$)	E_{th} (erg) ($\times 10^{48}$)
G5.89-0.39	2.0	2.37	105	-9.48	4.38	12.81	22.29	3.7	1.9	1.1	0.18
G10.47+0.03	5.8	1.24	30	-10.42	2.70	12.60	23.02	184	5.8	10.3	5.1
G10.6-0.4	6.0	1.14	20	-9.92	8.74	13.11	23.03	497	9.4	27.2	21.6
G19.61-0.23	4.5	0.71	45	-10.32	4.57	12.83	23.15	162	<4.7	<6.8	<2.7
G20.08-0.14	4.1	0.66	30	-11.06	2.68	12.60	23.66	374	4.0	4.8	1.6
G29.96-0.02	9.0	0.63	40	-9.70	5.14	12.88	22.58	124	7.9	19.2	12.8
K3-50A[c]	8.6	0.48	20	-10.15	3.15	12.67	22.82	276	<9.0	<24.7	<18.7

[a]Full Width at Zero Power of the SiO line.

[b]Longest axis of SiO emitting region, after deconvolution from the 14″ JCMT beam.

[c]The SiO abundance used towards K3-50A for deriving outflow kinematics is the average abundance from the other six sources.

Table 3.2: HCO^+ Observations and Derived Infall Properties

Source	T_{mb} (K)	FWZP[a] (km s^{-1})	$< \int T^*_{mv} dv >$ (K km s^{-1})	$<\log[N_{HCO^+}]>$ (cm^{-2})	$<V_{in}{}^b>$ (km s^{-1})	$\dot{M}_{in}(M_\odot/yr)$ ($\times 10^{-3}$)	Age (yr) ($\times 10^4$)	M_{in} ($M_\odot$)	M_{in}/M_{out}
G5.89-0.39	31.5	140	35.6	13.17	...	...	0.29	...	...
G10.47+0.03	11.7	60	11.2	12.67	1.02±0.1	8.89	0.88	78.0	0.42
G10.6-0.4	31.2	50	28.4	13.08	1.19±0.1	27.34	1.42	389	0.78
G19.61-0.23	8.3	80	14.4	12.78	1.49±0.6	<8.5	<0.71	<60.3	<0.37
G20.08-0.14	5.9	55	9.2	12.59	1.35±0.3	5.51	0.60	33.0	0.09
G29.967-0.02	16.5	30	9.2	12.59	...	...	1.19	...	...
K3-50A	17.0	30	13.2	12.75	...	...	<1.36	...	...

[a]Full Width at Zero Power of the HCO^+ line.

[b]Infall velocity averaged over each pixel with an infall signature

The integrated intensities in SiO and HCO^+ were used to find the column density of gas emitting across the map in that tracer. For optically thin gas, the column density in the higher energy level is proportional to the integrated intensity of the line, with a scaling constant proportional to the frequency of the transition and the Einstein coefficient for that transition (see Equation 1 of Chapter 2, or Tielens, 2005). Assuming local thermodynamic equilibrium and an ambient temperature of 44 K (as was done in Chapter 2), we can use the partition function to determine the column density of optically thin gas in each tracer (see for instance Equation 14.38 of Rholfs & Wilson, 2004). The average column densities of SiO and HCO^+ are presented in Tables 3.1 and 3.2. The values for the $H^{13}CO^+$ column density are not presented here, but were found to be only 4-22 times less than those for HCO^+. That we do not see a larger difference in the column densities, given the abundance ratio of 77 between the isotopologues, suggests that we are not seeing all of the HCO^+ emission because the line is optically thick. Thus, our derived column densities are lower limits to the true HCO^+ column densities due to optical depth effects. This trend was also seen in Chapter 2, and supports the claim that the double peaked HCO^+ profiles towards four of our sources are due to self absorption of the optically thick line, and not multiple clouds along the line of sight.

3.3.1 Outflow Properties Derived from SiO Observations

In an environment which has recently been shocked, the abundance of SiO can be enhanced up to a factor of 10^{-8} (from dark cloud abundances of approximately 10^{-11}) with respect to molecular hydrogen, due to silicon being liberated from dust grains and combining with oxygen to form SiO (i.e. Caselli et al., 1997; Schilke et al., 1997). After approximately 10^4 years, SiO depletes out of the gas phase again and the abundance drops (i.e. Pineau des Forets et al., 1997). Because of the short enhancement lifetime, SiO is generally only detectable in regions which have recently been shocked. Where we detect SiO (J=4-3) we suggest there is ongoing outflow activity.

We present the column density of SiO towards each source in Table 3.1. We can divide this value by the abundance of SiO with respect to H_2 in order to determine the column density of shocked gas in each region. These values are also presented in Table 3.1. We used the same methods as described in Chapter 2 to calculate the abundance of SiO towards G10.6 ($\log[N_{SiO}] + \log[X_{CS}] - \log[N_{CS}] = \log[X_{SiO}] = -9.92$) and we have assumed a constant SiO abundance across each map. We note that the SiO column densities listed in Chapter 2 are over estimated by a factor of 3.8, and thus the logarithmic SiO abundances listed in that paper are corrected in Table 3.1. Because we have adopted

a new distance for G10.47, we have had in addition to modify our original abundance estimate from Chapter 2. The CS column density quoted in Plume et al. (1997) appears to be distance independent; however, the CS abundance presented in Shirley et al. (2003) is dependent on the assumed distance to the source (see their Equations 7 and 12). Thus, our SiO abundance has changed from -9.53 in Chapter 2 to -10.42 when the new distance and revised column density are taken into account. The SiO abundance determined for K3-50A in Chapter 2 ($\log[X_{\rm SiO}]$ = -11.6) is much closer to that found in dark clouds than in outflow regions. The region in which SiO is emitting is unresolved by our observations and highly beam diluted. Thus, for our analysis, we have assumed an SiO abundance of -10.15, the average abundance from our other six sources. Based on the abundance estimates presented in Table 3.1, we have determined the total column of shocked material towards each source, from which we determined the mass of shocked gas because we know the area of the emitting region (see below). For our sources which are unresolved in SiO, we have taken the radius of our primary beam to be the radius of the emitting region.

Comparing the integrated intensities of our SiO emission in the central pixel of each map, where our signal to noise ratio is highest, to the models presented in Schilke et al. (1997), we suggest shock velocities of 20-22 km s^{-1}, and ambient densities of $n_o = 10^6$ cm^{-3}. The ambient densities suggested here are consistent with those of Plume et al. (1997) who determined densities and CS column densities for these regions using large velocity gradient models. For each of our sources, we adopt a shock velocity of v_s = 21 km s^{-1}.

Because we have mapped the SiO emission towards seven sources, we can determine the radius of the region in which SiO is being emitted (R_s). The method used to determine the deconvolved source size was described in Section 3.2, and the radius of the emitting region is presented in Table 3.1. From this radius and the shock velocity determined above, we can constrain the ages of our outflows from simple kinematic arguments. These approximate outflow ages are presented in Table 3.2 and are used later to constrain the amount of infalling material.

In order for the outflow shocks to reach their observed sizes given the mass of shocked gas, the powering sources for these outflows must produce enough energy to push through the ambient medium. If we assume a steady wind is driving a spherical bubble of gas outward, we can use the model of Castor et al. (1975) to determine the luminosity required to push the ambient gas. Equation 6 of Castor et al. (1975) can be re-expressed as:

$$L_o = R_s^2 \rho_o v_s^3 \left(\frac{154\pi}{125}\right) \tag{3.1}$$

where $L_o = E_o/t$ is the luminosity imparted by the wind, R_s is the radius

of the bubble, v_s is the shock velocity, and related to the outflow age by $v_s = R_s/t$, and ρ_o is the ambient density, and related to the ambient number density by the mass of molecular hydrogen ($\rho_o = \mu m_H n_o$). While much of this wind luminosity goes into accelerating the ambient medium, some of it is also transferred into thermal energy. From Basu et al. (1999), the thermal energy can be expressed as $E_{\rm th} = (5/11)L_o t$, or, given the value for t above, $E_{\rm th} = (5/11)L_o R_s/v_s$. Both the calculated wind luminosity and thermal energy required to power these wind driven shocks are listed in Table 3.1. These thermal energies are of approximately the same order of magnitude as the kinetic energies calculated for the CO outflows in a number of massive star forming regions (see for instance Wu et al., 2004; Klaassen & Wilson, 2008a); similarly the wind luminosities are comparable to the luminosities of their HII regions (see for instance Wood & Churchwell, 1989).

3.3.2 Infall Properties Derived from HCO^+ Observations

Many authors suggest that an asymmetric self absorbed line profile of an optically thick line tracer in which the blue emission peak is brighter than the red, and the optically thin tracer has a single line peak, can be indicative of infall (i.e. Mardones et al., 1997; Gregersen et al., 1997; Fuller et al., 2005). Here, our optically thick line is HCO^+ (J=4-3) and the optically thin isotopologue is $H^{13}CO^+$ (J=4-3).

From Chapter 2, we expected to observe infall signatures in G10.47 and G19.61. Infall is detected towards these two sources, as well as towards G20.08 from our original study. In our single pointing observations, G20.08 was shown to have a double peaked line profile in both HCO^+ and $H^{13}CO^+$, which was suggested to be due to two overlapping sources. However, in the more extended map, we see that $H^{13}CO^+$ becomes single peaked, suggesting that perhaps it is optically thick towards the center of the source and that mapping is required to resolve the ambiguity with respect to the chance super-position of line of sight clouds and self absorption of multiple isotopologues. G10.6 was not in our original sample, but was added because it was known to have small scale infall motions. It too is seen to have a large scale infall signature.

In Chapter 2, we suggested that beam dilution may have been a contributing factor as to why we did not detect infall in a number of sources. That we have detected extended infall in two distant ($\sim$ 6 kpc) sources in this study suggests that if beam dilution of the signal is a problem, it only affects intrinsically smaller sources, and not intrinsically more distant ones, since our unresolved detections are for G19.61 and G20.08 at 4.5 and 4.1 kpc.

Infall velocities were calculated for each self absorbed HCO^+ spectrum towards G10.47, G10.6, G19.61, and G20.08 using the models of Myers et al.

(1996) in the same way as described in Chapter 2. From our rms uncertainties in line temperatures and the spectral resolution of our observations, we determined the uncertainties associated with our derived infall velocities. We used these uncertainties to limit the regions in which we claim infall detections. Only if the derived infall velocity is more than three times our uncertainty for that spectrum do we claim to detect infall in that pixel. Towards G19.61 and G20.08, robust detections were made in one and three pixels (respectively) suggesting that the infall in both of these sources is unresolved. Towards G10.47 and G10.6 (both at approximately 6 kpc), robust infall detections were made in seven Nyquist sampled pixels per map, suggesting that the large scale infall in these regions is extended.

Along the northern, blue shifted, outflow lobe in G10.47, the HCO^+ line profiles again become double peaked. It is quite possible that there is a second instance of a collapsing region here since SiO is marginally detected (at the 3σ level) in the middle of this northern extension. The double peaked profiles do lead to infall velocities (in three pixels) which are greater than 3σ; however, we do not include this region in our infall analysis for a number of reasons. The infall signature is not continuous from the central region to this northern region, which suggests that there are two distinct regions of infall. This discontinuity would confuse conclusions about the central infall region. Similarly, we are interested in the infall activity surrounding HII regions, where we know massive stars are forming. Neither the mid infrared nor radio maps of this region (Pascucci et al. (2004) and Wood & Churchwell (1989), respectively) extend far enough to the north to determine whether there are HII regions in this northern extension. Archival SCUBA maps of this region at the same resolution as our observations (Di Francesco et al., 2008) show emission which has the same extent and morphology as our HCO^+ observations.

For each region in which infall was observed, we determined an average infall velocity by taking the mean of the infall velocities determined for each position in each map using the models of Myers et al. (1996). This averaging resulted in the velocities shown in Table 3.2. We chose to use this method over creating an averaged spectrum and determining infall velocities from it. The latter method resulted in unreasonably high infall rates (i.e. 5 km s^{-1} in G10.47), which give very large mass infall rates (0.22 $M_\odot$ yr^{-1}) and total infall masses ($\sim$ 2000 $M_\odot$) assuming constant infall rates over the lifetime of the outflow. Averaging the spectra and then determining the infall velocity increased the infall velocity by increasing the full width at half maximum (FWHM) of the line. Since the infall velocity varies as the FWHM squared (see Equation 9 of Myers et al., 1996), this broadening leads to an overestimate of the infall velocity. Thus, for our unresolved sources, the calculated infall velocities may be upper limits, since there could be unresolved velocity gradients within the JCMT beam. Higher resolution imaging of these sources could decrease our

calculated infall velocities.

Using the derived average infall velocities for each region, we determined mass infall rates for each source using $\dot{M} = dM/dt \approx \rho V v_{\rm in}/r = (4/3)\pi n_o \mu m_H r^2 v_{\rm in}$, where $\rho = \mu m_H n_o$ is the mass density, $v_{\rm in}$ is the infall velocity presented in Table 3.2, and V/r is the area of the infalling area (which we assume to be circular). Since the area in which we detected an infall signature was always similar to the area in which SiO was detected, we used the radius of the SiO emitting region as the radius of the infalling region.

From the radii of the SiO emitting regions and a shock velocity of 21 km s^{-1}, we were able to estimate outflow ages in Section 3.3.1. Assuming infall and outflow are contemporaneous, these outflow ages can be used to constrain how much mass has undergone infall. These values are also given in Table 3.2, and represent the total mass of infalling molecular gas, not just the mass of the infalling HCO^+.

3.4 Discussion

It is interesting to note that the infall and outflow signatures in G19.61 are both unresolved, and the signatures in G20.08 are both marginally resolved. This comparison suggests that the shocked region, as traced by SiO, may have a similar physical size as the infall regions in these smaller sources. Towards G10.6 and G10.47, the regions over which we have robustly detected extended infall, our deconvolved SiO emitting regions also appear to be on the same approximate spatial scales.

Comparing infall mass and outflow mass, we note that our infall masses are lower than our outflow masses. This is contrary to the results of Beuther et al. (2002); however, their ratio was calculated for the protostellar jet, not the entrained molecular outflow. This comparison to Beuther et al. (2002) suggests that more of the ambient mass is entrained into the large scale molecular outflow (produced by a protostellar jet) than falls in onto the forming stars (i.e. Shepherd & Churchwell, 1996).

3.4.1 G10.47: Extended Outflow or Chance Super-position?

The large spatial extent of the HCO^+ emission in our map of G10.47 places it among the largest molecular outflows due to star formation in our Galaxy. Some Herbig-Haro objects have been observed emanating from nearby lower mass star forming regions at distances of up to 12 pc from their powering stars (i.e. Bally & Reipurth, 2002); however in those cases, the associated molecular outflow is not nearly as wide as the case of G10.47, and those jets are not pushing through an ambient medium dense enough for massive stars to form (i.e. 10^6 cm^{-3}). In Chapter 2, we used a distance estimate of 12 kpc

to G10.47. Given the extent of HCO^+ gas ($\sim 2'$) in our current maps, this distance would give a linear scale of over 4 pc for a single outflow. Other authors have suggested a distance to this source of 5.8 kpc (i.e. Gibb et al., 2004). For the analysis presented here, we adopt this new distance, which changes the length of the outflow from 4 pc to 2 pc. Given that this source is along a line of sight reasonably close to both the Galactic plane and Galactic center, it is not unreasonable to suggest that what appears to be an extremely large outflow is instead the super-position of a number of clouds along the line of sight. However, based on the arguments presented below, we suggest that the gas kinematics and morphology are due to a large outflow.

Examining the spectra of our HCO^+ map, we note that while the HCO^+ emission is extended, it is not present in all pixels, suggesting that we have captured all of the emission in this velocity range. Figure 3.8 shows the HCO^+ line profiles averaged over the blue and red shifted emission regions as well as the HCO^+ and $H^{13}CO^+$ line profiles averaged over the central nine pixels of our map. The red and blue spectra, while having very little overlap between their profiles, do both fit within the width of the source center line profile. The velocities at line peak for the blue and red spectra are -64 and -70 km s^{-1} respectively, and match the velocities of the two peaks of the self absorbed, averaged HCO^+ central profile. The single peak of the optically thin $H^{13}CO^+$ is at -67 km s^{-1} as is the minimum of the HCO^+ self absorption feature. This self-absorption lies directly between the peaks of the red and blue profiles, and is the same as the source rest velocity. No other sources in the W31 region have rest velocities similar to the ones seen in the G10.47 region.

The double peak in the HCO^+ spectrum is due to self absorption, not multiple components, since there is a single peak in the $H^{13}CO^+$ spectrum. The same is true for the CO isotopologues in this region. The BIMA observations of Gibb et al. (2004) show one peak in $C^{18}O$, while the ^{13}CO observations of Olmi et al. (1996) with the IRAM Interferometer show two peaks indicative of self absorption.

The first moment map of the HCO^+ emission (grayscale in Figure 3.9) in this region also suggests a single outflow. The observed smooth transition from blue to red along the source would be more likely to be observed in one source with a velocity gradient than three separate sources with discontinuous cloud boundaries. The second moment map of this region (contours in Figure 3.9) suggest that the largest velocity dispersion is towards the center, and continuously decreases towards the emission edges (outflow lobe ends), suggesting that most of the mass is centrally concentrated.

While we favor the outflow interpretation of this morphology, higher resolution, large scale observations of this source are necessary in order to resolve this ambiguity. This region contains four individual UCHII regions and what is likely a large scale outflow with a collimation factor ($R_{\rm maj}/R_{\rm min}$) of approx-

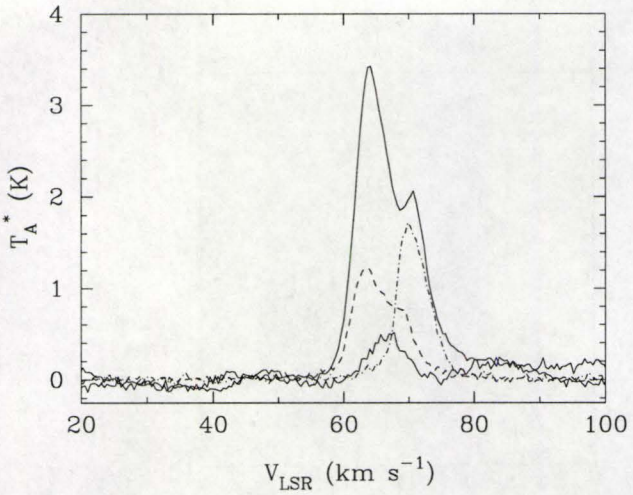

Figure 3.8: Spectra from G10.47 averaged over 9 pixels each. The strongest (solid) line represents the HCO^+ emission towards the source center, while the dashed and dashed-dotted spectra represent the HCO^+ emission towards the blue and red shifted regions (respectively). The least intense (solid) line represents the $H^{13}CO^+$ emission towards the same central region as the strong HCO^+ line. Note that the central HCO^+ emission spectrum has a double peaked line profile due to self absorption, while the $H^{13}CO^+$ appears single peaked and optically thin.

imately 1.5, which may be even more highly collimated at higher resolution. Objects like G10.47, with large scale, fairly collimated outflow emanating from a cluster of HII regions pose interesting challenges for accretion models.

3.4.2 Large and Small Scale Infall in G10.6

As stated previously, G10.6 was added to our source list because it was previously known to show evidence for small scale infall, both in molecular gas (Sollins et al., 2005) and ionized gas (Keto & Wood, 2006). These small scale infall signatures appear to be consistent with a single accretion flow which changes from being molecular to ionized as it passes the ionization boundary of the HII region. While we cannot determine the orientation of the large scale infall from our observations, we note that our derived mass infall rate (0.03 $M_\odot$ yr^{-1}) is comparable to, but slightly larger than, that of Sollins et al. (2005) (0.02 $M_\odot$ yr^{-1}). This similarity may suggest that the large scale infall possibly maps to the small scale accretion flow; in addition, despite resolving the infall region, we may still be over estimating the infall velocity due to velocity gradients in our larger JCMT beam (see Section 3.3.2).

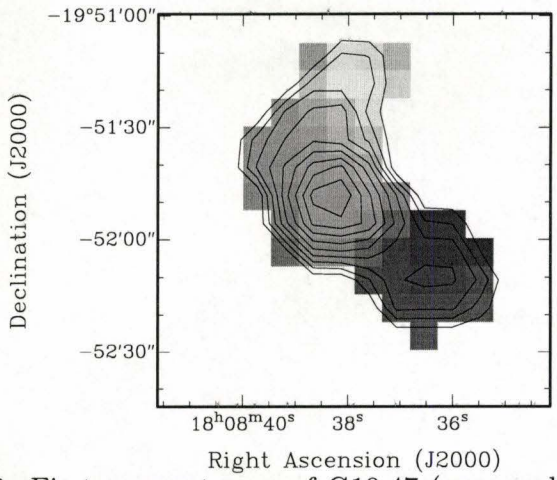

Figure 3.9: First moment map of G10.47 (gray scale). The grayscale ranges from 63 to 72 K km s^{-1}. The velocity weighted integrated intensity shifts smoothly from the blue lobe to the central source to the red outflow lobe, suggesting that this is a single source with an outflow. The second moment map (black contours) shows that the highest velocity dispersion is centered on the location of the HII regions. The contours start at 10% of the peak velocity dispersion (0.41 km s^{-1}) and increase in 10% intervals.

3.4.3 How Mapping has Changed the Results from Chapter 2

None of our basic conclusions drawn from our single pointing observations of SiO (i.e. column densities in the central pixel or outflow lifetimes) have changed due to mapping save for the infall detection in G20.08. However, with respect to the outflowing gas, we have been able to place constraints on the energy required to shock these regions. With respect to infalling gas, we have placed better constraints on infall velocities and shown that the lack of infall signatures in some sources is not due to the signature being beam diluted out of observability at large distances.

We have found that one of our sources which was previously not thought to have an infall signature (G20.08) in fact does appear to have large scale infall motions. This discovery suggests that more accurate infall results are possible with maps of massive star forming environments than with single pointing observations. Returning to the results of Chapter 2, we determined that seven out of the 14 sources with ongoing outflow signatures had infall signatures as well. These numbers can now be revised to eight out of 15 outflow sources with infall signatures when G10.6 is added to the source list. Thus, we find that approximately half of the sources with ongoing outflows have infall signatures which we take to trace accretion. Because our sources were selected based on

the presence of HII regions, ongoing infall suggests that there is a phase of massive star formation in which the star is still actively accreting, but is also burning hydrogen brightly enough to ionize its surroundings (see for instance the discussion in Keto & Klaassen, 2008).

3.5 Conclusions

We have found that just over half of the sources in our sample have large scale infall motions suggesting that the protostars powering the UCHII regions and massive outflows are still actively accreting material. Where we have detected infall motions, they have been on quite large scales, suggesting that infall, as traced by HCO^+, is in general observable with single dish maps at the distances to massive star forming regions. Maps are required in order to capture all of the infalling gas since the infall signature can be extended, even at 6 kpc. In mapping these regions, we have been able to determine how much mass is falling into the central regions of our sample sources, which we would not have been able to determine with our single pointing observations. We find that when the infall is resolved, the infalling mass is greater than 30 $M_\odot$. Our derived mass infall rate towards G10.6 is similar to the small scale rate found by Sollins et al. (2005), suggesting that we may be observing the same physical process, but on different spatial scales.

In general, we have found that SiO is not very extended; however, since we mapped these regions in SiO, we were able to determine the radius of the emitting region, the mass of shocked gas and how much energy is required to shock the gas surrounding a massive protostar. We find these energies and luminosities to be similar to the kinetic energy imparted to the outflowing gas and the luminosities of the HII regions themselves. We also find that the region over which we detect an infall signature and the region in which we detect SiO is quite similar, and find that in these regions, the total infall mass is less than the total outflow mass ($M_{in}/M_{out} \sim 0.1$ to 0.8) assuming the two processes are contemporaneous.

Chapter 4

High Resolution Molecular Line Observations of Massive Star Forming Regions I: Small Scale Infall and Rotation

This chapter is soon to be submitted to the Astrophysical Journal as an article titled "High Resolution Molecular Line Observations of Massive Star Forming Regions I: Small Scale Infall and Rotation." by P.D. Klaassen, C.D. Wilson, E.R. Keto and Q. Zhang.

4.1 Introduction

The formation mechanism responsible for low mass stars like the Sun is, in broad terms, well constrained, from pre-stellar cores (Ward-Thompson et al., 2002) to pre-main sequence stars (i.e. Shu et al., 1987; Andre et al., 2000). At approximately $8M_{\odot}$, however, the situation becomes more complicated. The forming star begins to burn hydrogen brightly enough for ultraviolet radiation to push outwards and ionize the surrounding gas. With these extreme outward pressures, how then, can accretion continue? Can a scaled up version of the processes involved in low mass star formation be responsible for forming massive stars (i.e. McKee & Tan, 2003)? Or does the dense and turbulent nature of massive star forming regions cause multiple protostellar cores to form, that then coalesce into more massive stars (i.e. Bonnell et al., 1997)? It is unclear how the former method is possible given the short formation timescales of, and large outwards radiation and thermal pressures involved in, high mass star formation; however, even in the densest star forming regions, stellar densities are a few orders of magnitude too small for the latter method to be feasible. In order to distinguish between these two mechanisms for forming a high mass

star, we can attempt to observe phenomena unique to one of the formation mechanisms. For instance, if we can observe both the infall of molecular gas onto the HII region, and rotation of the warm gas surrounding the HII region, we are more likely to be observing a scenario similar to that found in low mass star forming regions.

With interferometers, we can resolve the spatial structures and kinematics of a number of molecular species, and often determine whether the spectral line signatures are coming from the massive protostar/HII region or surrounding hot cores. In general, they filter out emission from large scale structures, and can be quite useful for observing small scale structures within larger scale emission (i.e. Eisner et al., 2008). Even high optical depth molecules, such as ^{12}CO, can be detected with the interferometer if they are observable in absorption against a bright, compact background such as an HII region.

Here, we present 1mm observations of ^{12}CO, ^{13}CO and SO_2 towards four massive star forming regions obtained with the SMA in its extended configuration. In Section 4.2 we present our observations and we present the results of both our continuum and our kinematic studies of the molecular gas tracers in Section 4.3. In Sections 4.4 and 4.5 we discuss our results and conclude.

4.2 Observations

Observations were obtained at the Submillimeter Array (SMA) in 2005. The SMA observations had H30α (at 231 GHz) centered in chunk 21 of the upper sideband (see Keto et al., 2008). The correlator had uniform channel spacing, at a resolution of 0.41 MHz (0.53 km s^{-1}) for the entire 2 GHz passband. Two isotopologues of CO (^{12}CO and ^{13}CO J=2-1) were simultaneously observed in the upper and lower sidebands (respectively, at 230.538 and 220.398 GHz) with SO_2 (J=$11_{1,11}$-$10_{0,10}$) observed in the lower sideband (at 221.965 GHz). The sources observed, pointing centers, integration times on source and average system temperatures for our observations are listed in Table 4.1. For each source, the ^{12}CO line occurs at a chunk boundary, and in the W51e2 and NGC 7538 IRS1 pointings, so does the ^{13}CO line. SO_2 does not appear at a chunk boundary in any of these observations. Having a line appear at the boundary between two correlator chunks can lead to large uncertainties when interpreting spectra if the bandpass of each chunk is not properly calibrated. In each case where our line appears at a chunk boundary, the line intensities, and spectral features in the UV plane are well matched in the 30+ overlapping channels at the boundary, suggesting we are not introducing any offsets due to poor bandpass calibration. SMA data reduction and imaging was completed using the MIRIAD data reduction software. Bandpass calibration was completed using 3c454.3, while phase and gain calibration was completed using 1833-210 (for G10.6), 1911-201 (for G28.2), 2202+422 (for NGC 7538) and 2025+337

Source	Pointing Center (J2000)		V_{LSR}	Dist.	τ_{int}	T_{sys}	rms[a]
	RA	DEC	(km/s)	(kpc)	(hr)	(K)	(Jy/Beam)
G10.6-0.4	18:10:27.77	−19:56:04.5	-3	6.0	2.52	125	0.32
G28.2-0.05	18:43:58.17	−04:13:57.0	97	9.0	2.78	129	0.19
NGC 7538	23:13:45.30	+61:28:10.0	-59	2.8	5.41	104	0.12
W51e2/e8[b]	19:23:43.90	+14:30:34.8	55	7.0	4.75	128	0.23

[a] Single channel rms noise levels at a resolution of 0.53 km/s.
[b]Note that W51e2 and W51e8 were observed simultaneously.
(W51e8 is offset from the pointing center by 7″.)

Table 4.1: Observed Sample of Massive Star Forming Regions.

(for W51e2/e8). In order to test how robust our MIRIAD data reduction was with respect to the SMA native data reduction package MIR, we compared the H30α intensities reported in Keto et al. (2008) with those we obtained after reducing our data with MIRIAD. We found intensities which were within ±15% of those reported in Keto et al.

Before inverting our molecular line data into the image plane, we fit and removed a linear baseline from our data in the *uv* plane using the MIRIAD command `UVLIN`. This process removes the continuum emission from the map, and ensures that the signal detected in an integrated intensity map is due to the spectral line only, not the continuum. Dirty images were created using robust weightings of between 0.5 and 2, and clean components were found using a 3σ cutoff in a region smaller than the primary beam which varied by source. Clean images were then restored using the components found when cleaning the dirty image.

The 220 GHz continuum emission maps presented here were also created using `UVLIN` and line contamination was minimized by inputting frequency intervals to skip when determining the continuum emission. These data were then brought into the image plane using the same methods as for the line data.

4.3 Results

The 2 GHz bandwidth of the SMA correlator allows for the simultaneous observation of a large number of molecular species as well as the continuum emission. At 230 GHz, its extended configuration is sensitive to structures on size scales smaller than $\sim 10''$, and has a resolution element (a synthesized beam) of approximately 1″ (actual sizes of the individual synthesized beams are given in Table 4.2). At the average distance to the high mass star forming regions discussed in this chapter (6.4 kpc), an UCHII region of 0.1 pc across measures 3.2″ on the sky. Thus, the data presented here are ideally suited to

characterizing the gas close to the HII region.

The continuum emission we present below is, for most sources, primarily due to the thermal emission from dust. From this, we can estimate the mass producing this emission. We can also use molecular line emission to estimate masses, as we present below using SO_2.

Each of our observed molecular species traces a different part of the gas surrounding the HII region, and from the velocity shifts in the lines, we can determine the kinematics of the various components of the region. For instance, ^{12}CO is the second most abundant molecule in the ISM (after H_2) and it can be used to trace low column density gas since it becomes optically thick quite easily. In the observations presented here, most of the ^{12}CO is filtered out by the interferometer; however we can use the 'pencil beam' along the line of sight towards the HII region to observe ^{12}CO in absorption and see the small scale structures associated with the ^{12}CO emission. In Chapter 5, we present the large scale structures observable using ^{12}CO.

The ^{13}CO isotopologue is 55 times less abundant than ^{12}CO (Wilson & Rood, 1994) and thus can be used to trace the molecular gas surrounding the observed massive protostars at slightly higher column densities. We can use the ^{13}CO to trace bulk flows (as described below in Section 4.3.1) in both emission (if the emission region is small enough) or in absorption like with ^{12}CO. The third molecular species presented here, SO_2, is not a tracer of bulk gas like CO, but of warm gas. It is generally only observable in regions where the temperature is between 100-300 K (Doty et al., 2002; Charnley, 1997), like the warm gas surrounding an HII region.

We have used these three molecular species to understand the kinematics of the gas surrounding five massive star forming regions. Below, we describe how we use these observed species to detect infall and rotation towards these sources as well as how we have used the continuum emission to derive gas masses. Maps of the ^{13}CO and SO_2 emission presented here are shown in Figures 4.1-4.5. In each case, the three panels on the right side of the Figure show contours of the continuum emission with the grayscales showing the integrated intensities of the SO_2 (top panel) and ^{13}CO (bottom panel), while the panel with the color scale shows the first moment (velocity weighted integrated intensity) map of the SO_2 emission. In the two SO_2 maps, the line through the source denotes the cut in position along which the PV diagram was created. The position angle of the PV diagram cut was determine based on the direction of the velocity gradient present in the first moment map and it is centered on the continuum peak. The elliptical contour shown in each first moment map corresponds to SO_2 emitting region deconvolved from the synthesized beam (as described in Section 4.3.2). The upper left panel shows a PV diagram of the ^{13}CO (in grayscale and in white contours) and SO_2 (black contours), while the lower left panel shows the CO spectra along the line of sight towards the continuum

Parameter		G10.6	G28.20	W51e2	W51e8	NGC 7538
Synthesized beam						
Resolution	($''$)	1.5×0.9	1.2×0.9	1.3×0.7	1.3×0.7	1.2×0.9
PA[b]	(^{o})	61	-85	-85	-89	-79
PV Diagram cut coordinates						
RA offset[c]	($''$)	12	-1.5	0.6	0.0	0.3
Dec offset[c]	($''$)	14.4	0.0	-0.3	-6.6	0.3
PA[b]	(^{o})	140	100	48	146	210
SO_2 Emitting Region						
Offset[c]	RA	11.9±0.2	-1.5±0.1	0.76±0.07	0.1±0.1	0.31±0.07
($''$)	DEC	14.3±0.1	0.0±0.1	-0.17±0.09	-6.5±0.1	0.00±0.07
FWHM	Major	4.9±0.6	2.2±0.5	2.9±0.4	3.2±0.3	1.3±0.2
($''$)	Minor	2.2±0.2	2.0±0.5	2.3±0.3	2.9±0.3	1.3±0.2
PA[b]	($''$)	-66	-73	22.8	30.4	63.7
Deconv. Size[d]	($''$)	4.8×1.8	2.0×1.8	2.8×1.9	3.1× 2.6	0.9×0.5
PA[b]	($''$)	-64.9	-41.2	17.5	19.5	15.8
Peak Int.[e,f]		12±1	14±2	59±4	48±5	23±3
Total Flux[f]	(Jy km/s)	100±3	63±5	420±13	470±16	36±4

[a] Averaged over $\tau_{\rm int}$

[b] Position Angle Measured North of East

[c] Measured from Pointing Center

[d] Source size deconvolved from Synthesized beam.

[e] Units of Jy/Beam km/s

[f] Measurement uncertainties listed (not 20% calibration uncert.)

Table 4.2: Observation Statistics

peak.

4.3.1 Infall of Molecular Gas onto the HII Region

Unambiguous detections of infall onto massive star forming regions are difficult to make due to the large distances involved and the generally clustered nature of massive star formation. Here, we use the term infall to mean the large scale bulk inflow (when compared to the size of the HII region itself) of molecular gas towards the HII region, not the much smaller scale accretion of molecular gas directly onto the HII region, or the accretion of ionized gas onto the individual massive protostars themselves. With high angular resolution observations there are two robust methods for detecting molecular infall onto a specific HII region: an arc of emission in a position-velocity diagram (see, for instance, Zhang & Ho, 1997, and below), or redshifted absorption of a molecular line along a pencil beam towards a bright continuum source such as an HII region (see, for instance, Chandler et al., 2005, and below). Here, we present infall detections in ^{13}CO towards four of our HII regions using one of these two methods. We did not detect a molecular infall signature towards G10.6; however, we note that an ionized infall signature (Keto & Wood, 2006) as well as both small and large scale molecular infall signatures (Sollins et al., 2005; Klaassen & Wilson, 2008b, Chapter 3) have been seen in other tracers towards this source.

^{13}CO Infall Kinematics Seen in Emission

Infall was detected in ^{13}CO in emission towards G28.2 . The position-velocity (PV) diagram showing the characteristic 'arc' structure of infall for this source is presented in the top left panel of Figure 4.2. This type of arc structure in a PV diagram shows that at larger distances from the source, the velocity of the ^{13}CO emission is similar to the rest velocity of the region, since the infall motions are primarily perpendicular to the line of sight (i.e. along the plane of the sky with no line of sight velocity shift component to observe). As the emission gets closer to the direct line of sight to the source (i.e. the infall becomes primarily along the line of sight), the emission profile becomes redder. Thus, an arc structure in a PV diagram is indicative of spherical infall (Zhang & Ho, 1997; Keto & Wood, 2006). The position cuts for the PV diagrams presented here in Figures 4.1-4.5 were taken along the lines drawn in the SO_2 integrated intensity and first moment maps shown in the same Figures. These position angles are presented in Table 4.2. Towards G28.2 (Figure 4.2), the arc has the same orientation as the one shown in Figure 1.5, and peaks at a velocity of $\sim$ 110 km s^{-1}.

^{13}CO Infall Kinematics Seen in Absorption

With a bright continuum source for a background, we can observe absorption features in a given species (i.e. in an inverse P-Cygni line profile) to probe the kinematics of the gas along the line of sight to that source. Against a bright continuum source, only the foreground gas is absorbed. Thus, blue shifted absorption is due to gas moving away from the source and towards the observer (outflow), while red shifted absorption is due to gas moving towards the source, and away from the observer (infall).

In order to determine the absorption profiles of both CO isotopologues we plot the spectrum of each species towards the peak of the continuum emission in each source. The absorption profiles, when observed, are representative of the gas along the line of sight towards the HII regions. Regardless of whether there was an absorption profile in the spectrum, the ^{12}CO (thin gray line) and ^{13}CO (thick black line) spectra are plotted in the bottom left panels of Figures 4.1 - 4.5. The vertical black lines represent the V_{LSR} of the source. When an absorption profile is present in these spectra, the dotted lines show the fitted two layer infall models.

Along the line of sight towards NGC 7538 (shown in Figure 4.3) most of the absorption seen in ^{13}CO is red shifted with respect to the V_{LSR} suggesting that most of the line of sight ^{13}CO is undergoing infall with some contamination from outflowing gas (causing the blue shifted absorption). There also appears to be blue shifted emission in the ^{13}CO spectrum. The combination of absorption and emission along the line of sight has caused the integrated intensity (shown in the bottom right panel of Figure 4.3) to fall below the 3σ cutoff in intensity towards the continuum source, although emission can be seen off source in this region.

There are also redshifted absorption features in ^{13}CO observed along the lines of sight towards W51e2 and W51e8. There are also foreground clouds along the line of sight towards these sources, and due to the relatively low column densities at which ^{13}CO is observable, it is possible that these absorption features come from absorption of the gas by foreground clouds, and not in-situ absorption. However, molecules such as HCO^+ trace much higher density gas than ^{13}CO, and a redshifted absorption feature is seen towards W51e2 in the interferometer maps of Rudolph et al. (1990) and single dish maps of Cox et al. (1987). There is no absorption feature seen in HCO^+ in the interferometer map towards W51e8, and the single dish map cannot resolve the two sources. Since the HCO^+ absorption feature in W51e2 has been shown by other authors to be produced in the dense cloud containing the HII region and the velocity ranges of the previously observed HCO^+ absorption feature is the same as our observed ^{13}CO absorption feature towards W51e2, we suggest that our ^{13}CO observations are also tracing the gas near the W51e2 region, and extend that suggestion to the gas in the W51e8 region since the velocity ranges of the

absorption feature in this region are similar to those of the W51e2 region.

Towards W51e2, the absorption feature extends to slightly blue shifted velocities, although most of the absorption is red shifted from the V_{LSR}. It should be noted that the very strong blue shifted outflow lobe does appear to originate at the very edge of the HII region, and we could be tracing a small part of that motion in the absorption profile (Keto & Klaassen, 2008, see also Chapter 5).

The ^{12}CO absorption profile in NGC 7538 is much more symmetric about the V_{LSR} (equal parts blue shifted and red shifted), than the ^{13}CO. To a lesser extent, the same is true for the two sources shown in Figures 4.4 and 4.5 (W51e2 and W51e8, respectively). The ^{12}CO spectra in these later two sources both show much wider blue shifted absorption than the ^{13}CO, while showing similar widths of red shifted absorption. Here again, the combination of emission and absorption along the line of sight towards the HII region obscures the signal in the integrated intensity maps.

The low column densities probed by the ^{12}CO suggest that along these lines of sight, we are observing the gas far from the continuum source. The fairly symmetric absorption profiles could be due to both infall and outflow far from the source, or due to the turbulence inherent in regions forming massive stars. Towards NGC 7538, the width of the absorption features is the same as the full width at half maximum of the large scale ^{12}CO emission observed at the JCMT, while for the two regions in W51, the absorption features have the same width as the emission at zero intensity (see Chapter 5 for this JCMT data). As will be shown in Chapter 5, there is a large scale outflow observed in ^{12}CO towards NGC 7538, and there are large line wings in the single dish spectrum. The outflows observed towards the sources in W51e are much smaller scale, and line wing emission from these sources may be beam diluted out of observability in the single dish map of these sources. This suggests that the ^{12}CO is more likely to be tracing the turbulent motions in the outer layers of the massive star forming region than tracing both outflow and infall along the line of sight towards the HII regions.

The absorption features along the line of sight towards NGC 7538 IRS1 and both W51e regions are most likely saturated for much of that velocity range, since both isotopologues have approximately the same depth in the absorption feature, which is at, or slightly below zero intensity.

Using the two layer model described in Di Francesco et al. (2001), we have determined the infall velocities likely responsible for the observed ^{13}CO absorption profiles towards NGC 7538 IRS 1 and both W51e8 and W51e2. Using the same notation as Di Francesco et al. (2001) (i.e. that $J_x = T_0/[\exp(T_0/T_x) - 1]$ where $T_0 = h\nu/k$), our model produced line temperatures from

Source	T_c (K)	T_r (K)	T_f (K)	τ_0	ϕ	σ (km s^{-1})	$V_{\rm in}$ (km s^{-1})	$V_{\rm LSR}$ (km s^{-1})
NGC 7538	54	54	7.4	30	0.60	1.2	1.5	-57.75
W51e2	75.2	76.3	7.4	17.8	0.73	3.2	6.46	55.0
W51e8	110	50	7.4	40	0.40	2.9	3.8	58.5

Table 4.3: Infall Properties Derived from 2-Layer Infall Modeling

$$\Delta T_B = (J_f - J_{cr})[1 - \exp(-\tau_f)] + (1-\phi)(J_r - J_b) \times [1 - \exp(-\tau_r - \tau_f)] \quad (4.1)$$

in which ΔT_B is the observed brightness temperature of the line at velocity V, ϕ is the beam filling factor of the continuum source, $J_{cr} = J_c\phi - (1-\phi)J_r$, $\tau_f = \tau_o \exp(-(V - V_{\rm in} - V_{\rm LSR})^2/2\sigma^2)$, and $\tau_r = \tau_o \exp(-(V + V_{\rm in} - V_{\rm LSR})^2/2\sigma^2)$ where τ_o is the maximum opacity of the line, and σ is the velocity dispersion of the line (σ= FWHM/2.3548). We present values for these parameters in Table 4.3 which are suggestive of the line profiles presented in Figures 4.3 - 4.5.

We find, from modeling the infall in W51e8 (and the rotation in Section 4.3.2) that modeling fits best if the $V_{\rm LSR}$ of this source is 58.5 km s^{-1} instead of the 55 km s^{-1} used for the W51e2 region taken from Sollins et al. (2005). Thus, for this study, we set the $V_{\rm LSR}$ of this source to be 58.5 km s^{-1}.

As expected from the saturated absorption profiles, the optical depths suggested by our modeling are quite large. The infall velocities inferred for the W51e regions are much higher than the velocities generally seen in lower mass star forming regions (i.e Di Francesco et al., 2001); however, we note that due to the high optical depth of the lines, we are not observing the gas closest to the HII region, and thus we are tracing the larger scale infall motions of the region, not accretion onto the HII region itself. The beam filling factors shown in Table 4.3 suggest that the continuum emission is filling much of the beam, but not completely filling it. That the continuum source does not fill the beam is expected since there is blue shifted emission observed in the spectra towards each infalling source. This blue shifted emission can be accounted for as either foreground outflow emission or background infall emission. That the two layer infall models are able to fit this blue shifted emission suggests that we are observing background infall.

4.3.2 Rotation of Hot Gas Surrounding HII Regions

As stated previously, SO_2 is generally found in regions where the temperature is in the range between 100 and 300 K. This is due to the reaction pathways

leading to its creating requiring temperatures of $\sim$ 100 K to work efficiently and the destruction pathways requiring temperatures of $\sim$ 300 K (see Figure 8 of Doty et al., 2002)

In the top right panels of Figures 4.1 - 4.5 we present integrated SO_2 emission maps towards each source in grayscale, and the continuum emission in contours. For both the molecular and continuum emission, we present the coordinates of the peak intensity in Table 4.2 as offsets from the pointing centers presented in Table 4.1. Note that the position of the continuum peak is the same as the center coordinates for the PV diagrams and is thus only presented once. In each case, the continuum and SO_2 emission peak occur within the same synthesized beam. Each SO_2 integrated intensity map is cut at 3σ. The lowest contour of the continuum emission is also drawn in terms of the noise level. The contour levels are listed in the figure captions. In each case, the SO_2 emission is more extended than the continuum (without either region being deconvolved from the synthesized observing beam). That the SO_2 emission peaks at the same position as the continuum, and is slightly more extended suggests that we are tracing the warm gas surrounding the HII region in each case.

Using the MIRIAD command `IMFIT`, we fit an elliptical Gaussian to the SO_2 emitting region and were able to deconvolve it from the beam. The deconvolved FWHM fits to the SO_2 emitting region are shown as a single contour in the middle right panels of Figures 4.1 - 4.5 using the semi major and minor axes and position angles listed in Table 4.2.

The integrated intensity maps of the SO_2 were masked to twice this deconvolved region and the average intensity within the masked region was determined using the MIRIAD command `IMLIST`. As was done in Chapters 2 and 3, we can use the average integrated intensity in this region to determine the column density of the emitting gas via (See Appendix B):

$$N_{\rm TOT} = \frac{Z(T)}{g_u e^{-E_{u\ell}/kT}} \frac{8\pi k\nu^2}{A_{u\ell} hc^3} \frac{[SO_2]}{[H_2]} < \int T_R^* dv >= 4.057\times10^{13} \frac{[SO_2]}{[H_2]} < \int T_R^* dv > \tag{4.2}$$

where $Z(T)$ is the partition function for SO_2, g_u is the statistical weight of the upper level of the transition, $E_{u\ell}$ is the energy difference between the two levels in the transition, $A_{u\ell}$ is the Einstein A coefficient for the transition and ν is the frequency of the transition. From the column density, we can determine the mass of the emitting region since the deconvolved area is known, as is the distance to each source and the abundance of SO_2 with respect to H_2 ($[SO_2]/[H_2] = 5.67\times10^{-7}$ averaged from the sample of high mass star forming regions in Keane et al. (2001)).

SO_2 is an asymmetric top molecule with a large number of rotational transitions. As such, the partition function is much more complicated to calculate

Source	$< \int T_R^* dv >^a$ (Jy/beam km/s)	K→Jy^b	N^{a,c} ($\times 10^{15}$ cm^{-2})	Area ($\times 10^{34}$ cm^2)	Mass^a ($M_\odot$)
G10.6	6.5±0.9	18.63	4.9±0.7	13.6±0.6	2.3±0.4
G28.2	7±1	24.78	7±1	13.1±0.4	3.2±0.6
NGC 7538	13.8±0.6	21.44	12.0±0.5	0.5±0.02	0.2±0.02
W51e2	30±2	26.10	32±2	12.0±0.3	13±1
W51e8	24±2	26.10	26±2	16.3±0.3	14±2

[a] Measurement Uncertainties listed (not 20% calibration uncert.)
[b] Conversion from Jy/Beam to Kelvin
[c] Column Density

Table 4.4: Mass Estimates Derived from SO_2 Emission.

than for linear molecules such as CO and SiO. The Cologne Database for Molecular Spectroscopy[1] (CDMS) lists partition functions for the ground vibrational state of SO_2 at a number of different temperatures, but not at the 100 K temperature assumed for this study. Thus, we fit a polynomial to the values calculated at 75, 150, 225 and 300 K to interpolate the partition function at 100 K. $Z = 0.89T^{1.55}$ results in Z(100K) = 1142. The CDMS website also lists the statistical weight of the upper level of the transition. The Einstein A coefficient and energies of the upper and lower energy levels were obtained from the Leiden Atomic and Molecular Database[2]. Using Equation 4.2, and the constants provided by these databases, we were able to determine the column densities of the gas emitting SO_2. From the column densities and the emission area, we then determined the masses of the SO_2 emitting regions. These column densities and masses are listed in Table 4.4.

In the middle right panels of Figures 4.1 - 4.5 we present the first moment maps of the SO_2 emission. The color scale traces the shift in the peak velocity of the gas as it varies with position across the source (as illustrated in Figure 1.5). In each region we observe a velocity gradient across the source. Towards G10.6, this velocity gradient has the same orientation and velocity range as that found by Sollins et al. (2005) in NH_3. Towards W51e2, our velocity gradient has the same orientation as the one found by Zhang & Ho (1997) in NH_3; however, our range in velocities is higher, and the spatial scale of the observed gas is larger. In both instances, these authors suggest that the velocity gradients in their NH_3 observations are due to rotation, and thus we adopt this interpretation here, and extend it to our other sources as well. We also note that the position angles of these velocity gradients (given in Table 4.2 in terms of the PV cuts, which were made along the rotation axes) are perpendicular to the orientations of the outflows when the outflow directions

[1] http://www.astro.uni-koeln.de/site/vorhersagen/
[2] http://www.strw.leidenuniv.nl/ moldata/

are known (see Chapter 5). We note that the velocity gradient is not very well defined in G28.2. If it exists, it is not very extended (in the region with a high enough signal to noise ratio to appear in a first moment map), and the shift in velocity across the source may be comparable to the velocity resolution of our observations (0.53 km s^{-1}).

Since we detect a velocity gradient indicative of rotation around most, if not all, of our sources in SO_2, we suggest that this species is a good tracer of the hot, rotating molecular gas surrounding HII regions.

To determine the velocity gradient in their NH_3 observations of W51e2, Zhang & Ho (1997) fit an elliptical Gaussian to the emission in their PV diagram. The semi major axis of this elliptical Gaussian was projected onto the position and velocity axes (i.e. corrected for the position angle of the Gaussian fit) and used to determine the velocity shift (4 km s^{-1}) and angular size over which the shift occurs (0.2″ at 7 kpc is 0.0067 pc) to give a velocity gradient (500 km s^{-1} pc^{-1}). We employ the same method to determine the velocity shift and angular size from the PV diagrams shown in Figures 4.1 - 4.5. We note that the redshifted portion of the SO_2 emission in the W51e8 PV diagram is much more extended than the blue shifted portion. We suggest that this is due to contamination from the redshifted outflow lobe, and when fitting our Gaussian in the PV diagram, kept the center at 58.5 km s^{-1} and fit only the blue shifted portion of the emission.

Using the source distances listed in Table 4.1, we determined the velocity gradients listed in Table 4.5. For comparison, we also determined the velocity gradients for these sources using the semi major axis of the deconvolved emitting region shown in Table 4.2 with the velocity shift determined from the PV diagram. These values are also presented in Table 4.5.

If we assume that the rotation in these regions is in virial equilibrium (i.e. $V = \sqrt{GM/r}$), we can determine the dynamical mass enclosed within the SO_2 emitting region. Because we cannot constrain the inclination angle of these rotating structures from our observations, we will assume that the velocity gradients are observed primarily 'edge on' (i.e. the observed velocities are the true velocities of the gas) and thus our derived masses would increase for structures which are inclined with respect to the plane of the sky. Using the velocity shift determined previously, along with both methods of deriving the angular extent of the rotation, we can determine the enclosed mass, as presented in Table 4.5.

4.3.3 Mass Estimates from Continuum Emission

Much of the continuum emission at sub-mm wavelengths is due to the thermal emission of cold dust. In general, however, there is also a contribution from the free-free emission of the HII region itself. The free-free emission peaks

Source	ΔV^a (km/s)	$\Delta d^{1(b)}$ ($''$)	$\Delta d^{2(b)}$ ($''$)	Velocity Gradient (km/s/pc)		Mass ($M_\odot$)	
				1^c	2^c	1^c	2^c
G10.6	3.7±0.3	2.1±0.2	2.4±0.2	61±9	53±7	195±40	223±30
G28.2	2.7±0.3	0.9±0.2	1.0±0.2	67±18	60±15	64±23	71±18
NGC 7538	2.7±0.3	0.6±0.2	0.5±0.2	325±113	430±187	13±6	10±4
W51e2	5.3±0.3	1.2±0.2	1.4±0.2	130±23	110±17	265±59	310±48
W51e8	4.8±0.3	1.2±0.2	1.6±0.2	120±21	91±14	215±50	280±42

[a] Velocity shift measured in the PV diagram.
[b] Δd^1 refers to the length derived from the PV diagram while Δd^2 refers to the length derived from the deconvolved source.
[c] 1 refers to values derived using Δd^1 and 2 refers to values derived using Δd^2.

Table 4.5: Velocity Gradients and Dynamical Masses Determined from SO_2 PV Diagrams.

at longer wavelengths, and can be removed from the observed emission using $S_\nu \propto \nu^{-0.1}$ (Spitzer, 1998), under the assumption that the free-free emission is optically thin. Further assuming that the 2 cm emission in each source ($S^{\rm TOT}_{\rm 2cm}$) is entirely due to free-free emission, we can determine the free-free contribution of our continuum emission($S^{\rm f-f}_{\rm 1.4mm}$) using the values given in Keto et al. (2008), and scale our observed 1.4 mm flux densities ($S^{\rm TOT}_{\rm 1.4mm}$) accordingly ($S^{\rm dust}_{\rm 1.4mm}$ = $S^{\rm TOT}_{\rm 1.4mm}$ - $S^{\rm f-f}_{\rm 1.4mm}$). For the W51e8 region, where no 2 cm flux densities are given in Keto et al., we use the 3.6 cm flux measured by Mehringer (1994). These corrections resulted in free-free contaminations of less than 0.5 Jy, in all cases except for G10.6. Using this approximation, we find that the expected contamination from free-free emission in G10.6 (2.13 Jy) is greater than the observed flux density (1.75 Jy). This suggests that we are not seeing any dust in the continuum emission, and thus we do not calculate a dust mass for this region.

Using the equations and relations presented in Hildebrand (1983), we determined the masses of the regions producing the continuum emission (in units of $M_\odot$) via

$$M = 1.25 \times 10^{-3} \left(\frac{S^{\rm dust}_\nu}{\rm Jy}\right) \left(\frac{D}{\rm kpc}\right)^2 \left(\exp\left(\frac{0.048\nu_{\rm GHz}}{T}\right) - 1\right) \left(\frac{2400}{\nu_{\rm GHz}}\right)^{\beta+3} \tag{4.3}$$

where $S^{\rm dust}_\nu$ is the observed flux density (generally corrected for free-free contamination), D is the distance to source in kpc, $\nu_{\rm GHz}$ is the frequency of the ^{13}CO (J=2-1) transition in units of GHz, T is the dust temperature, and β is the power law scaling for the dust opacity, and we have extrapolated the dust emissivity from Hildebrand (1983) as $Q_\lambda = 7 \times 10^{-4}(0.125/\lambda_{mm})^\beta$, where

Source	$S^{TOT}_{1.4mm}$	$S^{TOT\,a}_{2cm}$	$S^{f-f}_{1.4mm}$	$S^{dust}_{1.4mm}$	M^b_1	M^b_2
G10.6	1.8±0.4	2.8±0.6	2.13±0.4			
G28.2	0.6±0.1	0.5±0.1	0.41±0.08	0.2±0.2	31±34	30±32
NGC 7538	2.8±0.6	0.42±0.08	0.31±0.06	2.48±0.7	40±11	38±10
W51e2	5.7±1.1	0.26±0.05	0.20±0.04	5.48±1.5	560±150	530±145
W51e8[c]	3.4±0.7	0.16±0.03	0.10±0.02	3.25±0.7	333±72	314±68

[a] 2 cm flux densities taken from Keto et al. (2008) (and references therein).
[b] M_1 was calculated with T=300 K, β=1.5. M_2, with T=100 K, β=1.0.
[c]No 2 cm flux density was listed in Keto et al. (2008) for W51e8
The 3.6 cm value from Mehringer (1994) was used instead

Table 4.6: Gas Masses Derived from Continuum Emission Measurements. We assume 20% calibration uncertainties (not included in uncertainty measurements).

0.125 and λ_{mm} are both wavelengths in units of mm. For our calculations, we have calculated gas masses based on the range of gas temperatures we could be observing in SO_2 (assuming the gas and dust temperatures are well coupled). The masses listed in Table 4.6 in the M_1 column were calculated assuming T=300 K and $\beta = 1.5$, while those listed in the M_2 column were calculated assuming T=100 K and $\beta = 1.0$. Increasing β to 2 (and keeping the temperature at 300 K) increases the derived masses by more than a factor of 3.

4.4 Discussion

From our ^{13}CO observations, we have been able to detect infall in four out of five observed HII regions, while the fifth source (G10.6) has been previously shown to have infall signatures in other tracers (i.e. Keto & Wood, 2006; Sollins et al., 2005; Klaassen & Wilson, 2008b). Thus, infall of molecular gas onto each of these HII regions has been observed. This suggests that there is a long lived stage of continued infall (and possibly accretion) after an HII region has formed and expanded to observable scales. It is unclear why no infall signature was detected either in emission or absorption towards G10.6; however, based on the observations of the other sources, we suggest that ^{13}CO can be used to observe molecular gas at the right optical depths to detect bulk infall onto HII regions. It is possible that the optical depth of the molecular gas in the G10.6 region is too low for us to detect an absorption feature in ^{13}CO along the line of sight towards the HII region. This is consistent with infall having been detected in higher density tracers such as HCO^+ and NH_3.

In addition to the infall signatures seen towards four of our sources, we have

detected rotational signatures in the hot molecular gas surrounding each HII region. These observations suggest that the hot gas surrounding these sources is undergoing bulk rotational motions, which, if continued into the HII region, seems to suggest that each observed massive star forming region in our sample has collapsed from a single massive over-density in the surrounding molecular cloud. If these rotational motions do continue into each of these HII regions, and there is a disk within each HII region, these disks may be similar to the photoevaporating disks within hypercompact HII regions as discussed in Keto (2007).

We have presented three different methods for determining the mass of these regions. We find that each of these methods gives a different mass for each region. The masses derived from the SO_2 emission indicate the amount of warm gas surrounding each HII region while the mass estimate derived from the SO_2 velocity gradients are representative of the dynamical mass enclosed within the SO_2 emitting region including the stellar mass and ionized gas. Thus, the masses derived from the SO_2 emission are expected to be much lower than the other two mass estimates. We find that, in general, the masses we derive from the SO_2 emission are approximately 5% of the dynamical masses. The exception to this is NGC 7538, where the emission mass is only $\sim 1.5\%$ of the dynamical mass. We note that the emission masses were calculated assuming a temperature of 100 K. If this temperature were increased to the upper limit suggested for SO_2 emission (300 K), the derived masses would increase by a factor of 5, and would then be approximately 25% of the derived dynamical masses.

We find that the dynamical mass and the continuum mass agree, to within 2σ for each source except for NGC 7538 (which agree to within 3σ). This suggests that the dynamically derived masses for these regions are reasonable, and that these rotating structures may be undergoing somewhat dynamically stable rotation.

NGC 7538 is the only source in this sample in which the deconvolved SO_2 emitting region is not resolved by the SMA beam. This suggests that beam dilution may cause us to underestimate the masses. The dynamical mass estimate for NGC 7538 (13 $M_\odot$) must be an under estimate since the source powering the HII region has a luminosity of $\sim 10^5$ (Kraus et al., 2006) suggesting a star of approximately 20 $M_\odot$. This suggests that the rotation observed in this source may not be dynamically stable. The masses derived for the other sources are large enough to account for one (or more) massive star(s) in each region suggesting that the rotation in these sources may be somewhat dynamically stable.

We find the masses derived for the two regions in W51e to be much larger than the masses derived for the other sources regardless of the methods used. Previous observations of this region have masses from the continuum emission

of 40 000 $M_\odot$ for an area encompassing both of these two HII regions (Rudolph et al., 1990), much larger than our derived masses. The dynamical mass of W51e2 derived by Zhang & Ho (1997) is 10 $M_\odot$ on size scales of 0.3″. Our value of 265 $M_\odot$ within 1.2″ is consistent with their mass projected out to the size scales we observed ($M_2 = M_1 * (V_2^2 r_2 / V_1^2 r_1)$), given the uncertainties in the measurements.

As discussed earlier, there appears to be a component of the SO_2 emission in the W51e8 region which is due to outflow (we present the CO outflow observations later, in Chapter 5). That we detect outflowing gas in the warm layers surrounding the HII region suggests that the mechanism driving the outflow must be enclosed within the shell of SO_2 emission; it must originate somewhere inside the HII region. Continued infall onto this region, rotation of the gas around it, and an outflow emanating from within the HII region all lead to the conclusion that the massive protostar(s) in this HII region are continuing to accrete material and are growing within the HII region.

4.5 Conclusions

We have detected rotation in the hot gas surrounding five massive star forming regions, and have detected molecular infall onto four of them (with the non-detection in the fifth believed to be due to optical depth effects). This suggests that the stage of ionized infall (and thus accretion) onto massive star forming regions must be fairly long lived if it is so readily observable.

That the hot molecular gas surrounding these HII regions is rotating suggests that the HII region itself may be rotating. If these HII regions are similar to the photoevaporating HCHII regions, then it is reasonable to expect the hot gas just outside of the ionization boundary to be rotating as well, as we see in our SO_2 maps.

We have shown evidence for infall and rotation for five massive star forming regions with HII regions. This suggests that there is an, apparently common, stage in the formation of massive stars in which infall onto a rotating structure (which powers the outflow) is occurring close into (if not directly onto) the HII region.

It is clear from the observations presented here that we are seeing an extended period of infall beyond the formation of an HII region, and that the molecular gas around these HII regions appears to be rotating as a whole. These two lines of evidence lead us to conclude that these massive stars are probably forming in a manner similar to, but scaled up from, the processes involved in the formation of lower mass stars, and not from the mergers of multiple, lower mass protostellar seeds

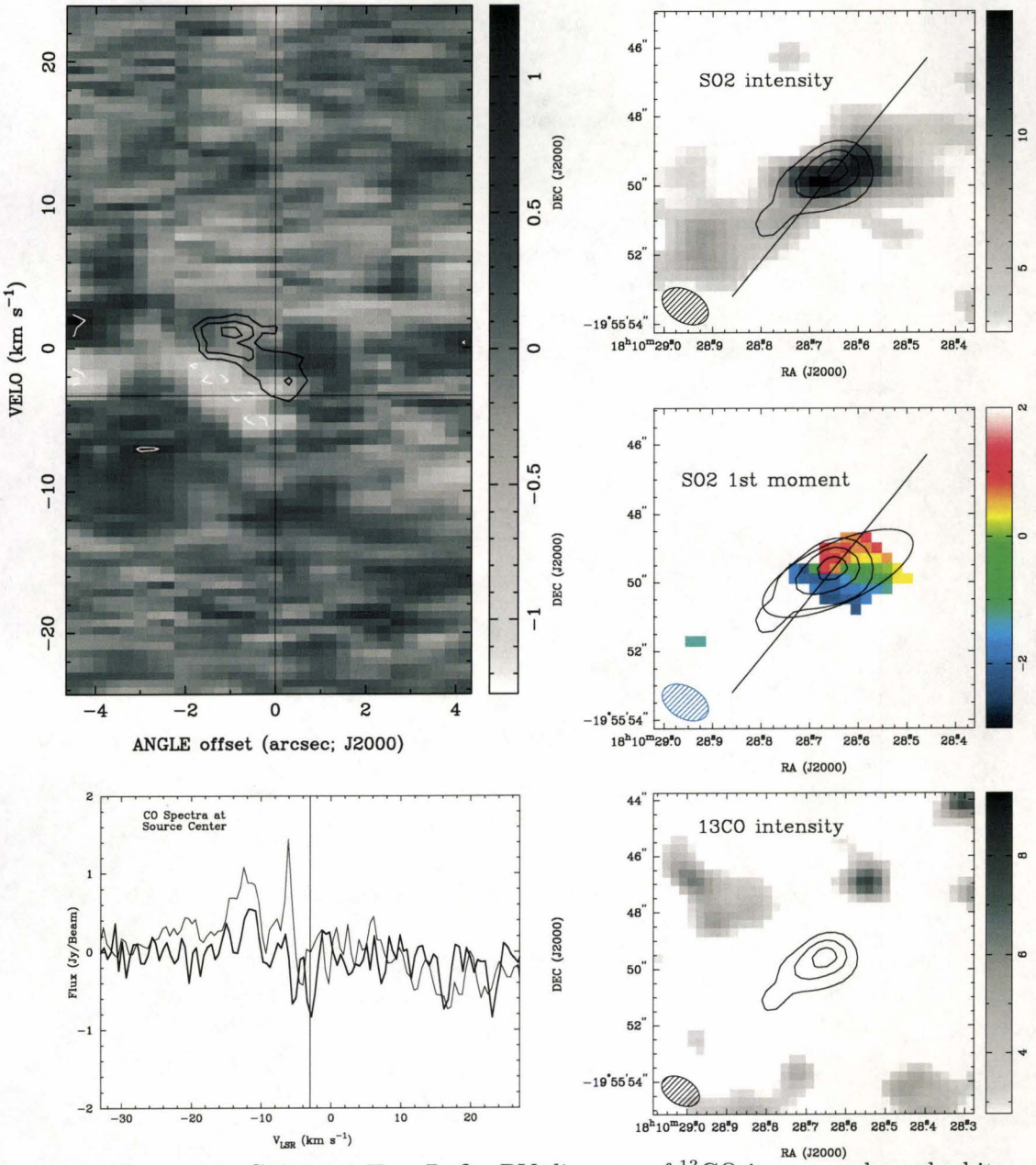

Figure 4.1: G10.6-0.4 **Top Left:** PV diagram of ^{13}CO in grayscale and white contours and SO_2 in black contours. Both sets of contours start at 3σ (0.32 Jy/beam), and increase in intervals of 1σ. **Bottom Left:** ^{12}CO (grey) and ^{13}CO (black) at the peak of the continuum emission. **Top Right:** Integrated intensity of SO_2 starting at 3σ (2.59 Jy/Beam km/s) with continuum contours starting at 5σ (0.24 Jy/beam) and increasing in intervals of 5σ. **Middle Right:** First moment map with continuum contours and an ellipse showing the deconvolved SO_2 emitting region. **Bottom Right:** ^{13}CO integrated intensity cut at 3σ (2.77 Jy/Beam km/s) with continuum emission contours.

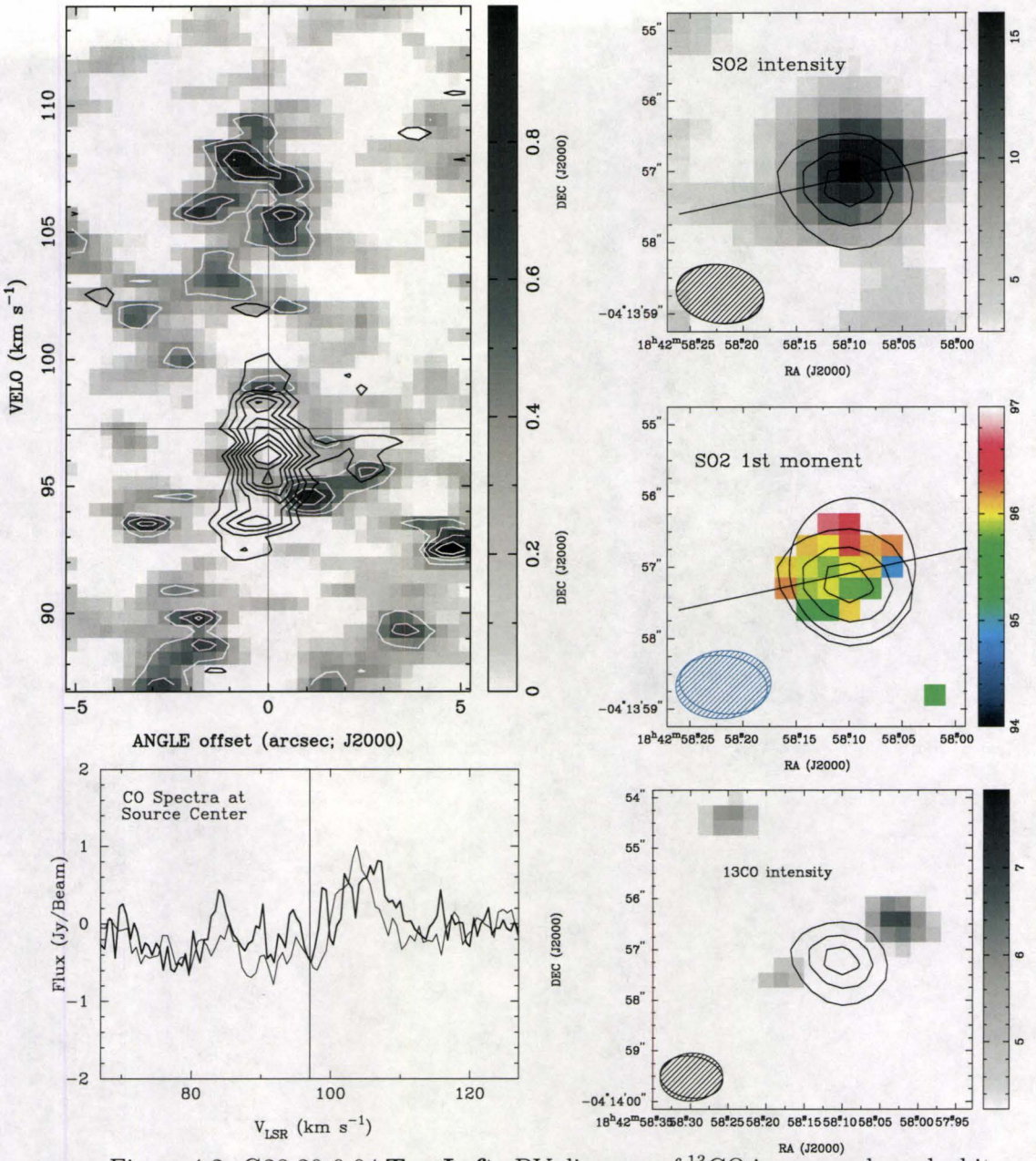

Figure 4.2: G28.20-0.04 **Top Left:** PV diagram of ^{13}CO in grayscale and white contours and SO_2 in black contours. Both sets of contours start at 2σ (0.19 Jy/beam), and increase in intervals of 1σ. **Bottom Left:** ^{12}CO (grey) and ^{13}CO (black) at the peak of the continuum emission. **Top Right:** Integrated intensity of SO_2 starting at 3σ (2.89 Jy/Beam km/s) with continuum contours starting at 3σ (0.13 Jy/beam) and increasing in intervals of 3σ. **Middle Right:** First moment map with continuum contours and an ellipse showing the deconvolved SO_2 emitting region. **Bottom Right:** ^{13}CO integrated intensity cut at 3σ (4.23 Jy/Beam km/s) with continuum emission contours.

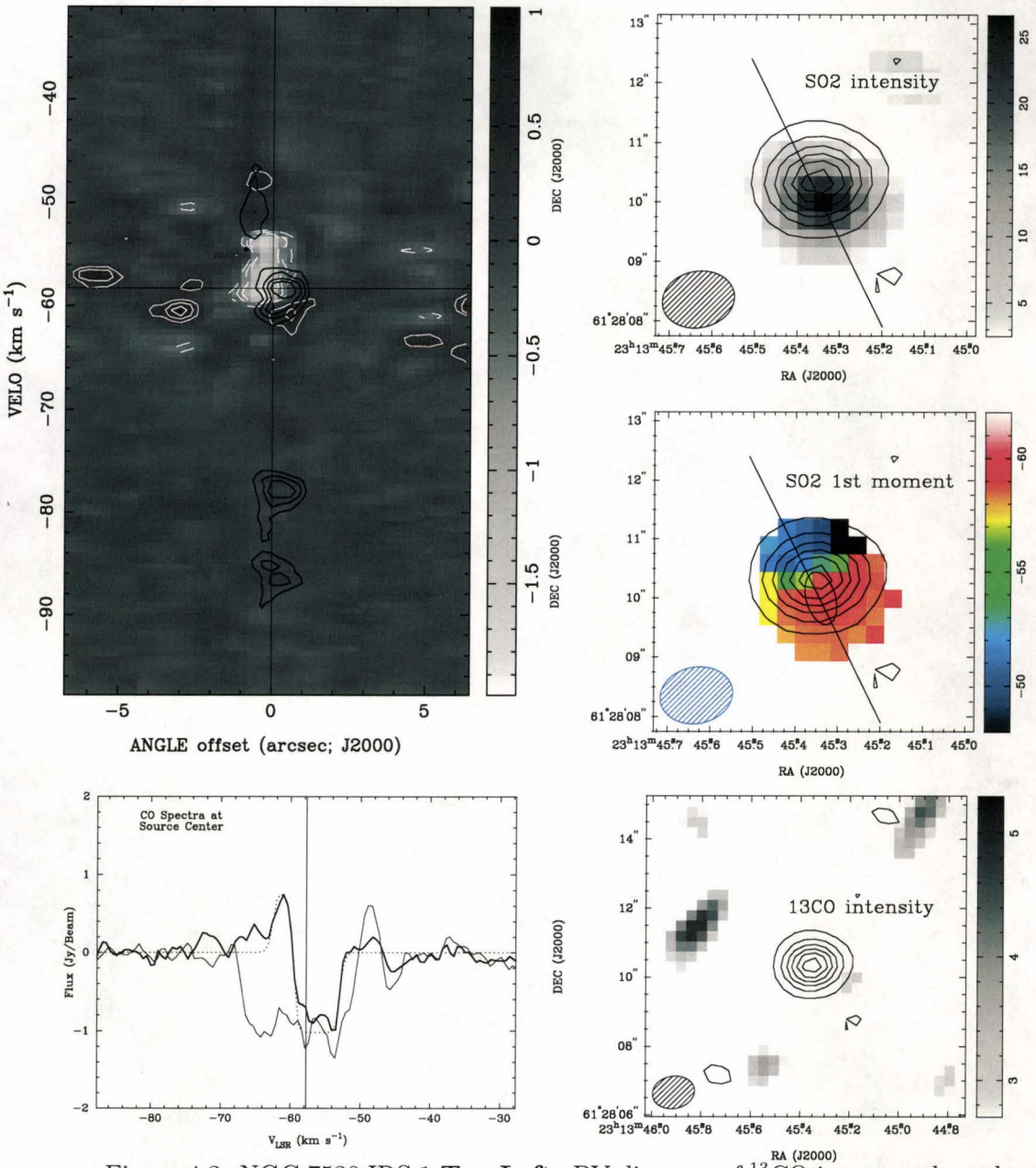

Figure 4.3: NGC 7538 IRS 1 **Top Left:** PV diagram of ^{13}CO in grayscale and white contours and SO_2 in black contours. Both sets of contours start at 3σ (0.12 Jy/beam), and increase (or decrease) in intervals of 2σ. **Bottom Left:** ^{12}CO (grey) and ^{13}CO (black) at the peak of the continuum emission. **Top Right:** Integrated intensity of SO_2 starting at 3σ (2.46 Jy/Beam km/s) with continuum contours starting at 10σ (0.2 Jy/beam) and increasing in intervals of 10σ. **Middle Right:** First moment map with continuum contours and an ellipse showing the deconvolved SO_2 emitting region. **Bottom Right:** ^{13}CO integrated intensity cut at 3σ (2.7 Jy/Beam km/s) with continuum emission contours.

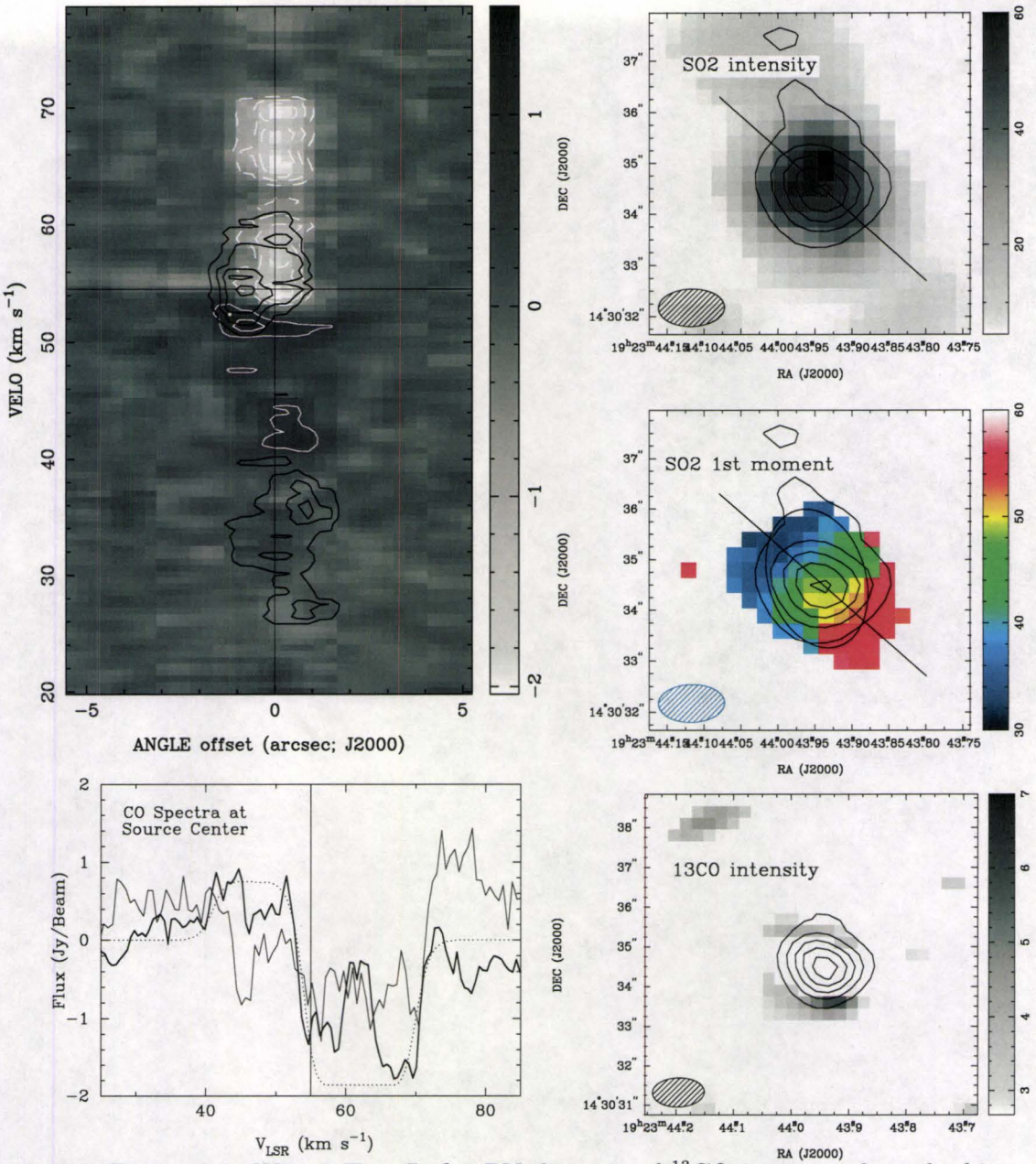

Figure 4.4: W51e2 **Top Left:** PV diagram of ^{13}CO in grayscale and white contours and SO_2 in black contours. Both sets of contours start at 3σ (0.23 Jy/beam), and increase (or decrease) in intervals of 2σ. **Bottom Left:** ^{12}CO (grey) and ^{13}CO (black) at the peak of the continuum emission. **Top Right:** Integrated intensity of SO_2 starting at 3σ (4.5 Jy/Beam km/s) with continuum contours starting at 7σ (0.4 Jy/beam) and increasing in intervals of 7σ. **Middle Right:** First moment map with continuum contours and an ellipse showing the deconvolved SO_2 emitting region. **Bottom Right:** ^{13}CO integrated intensity cut at 3σ (2.67 Jy/Beam km/s) with continuum emission contours.

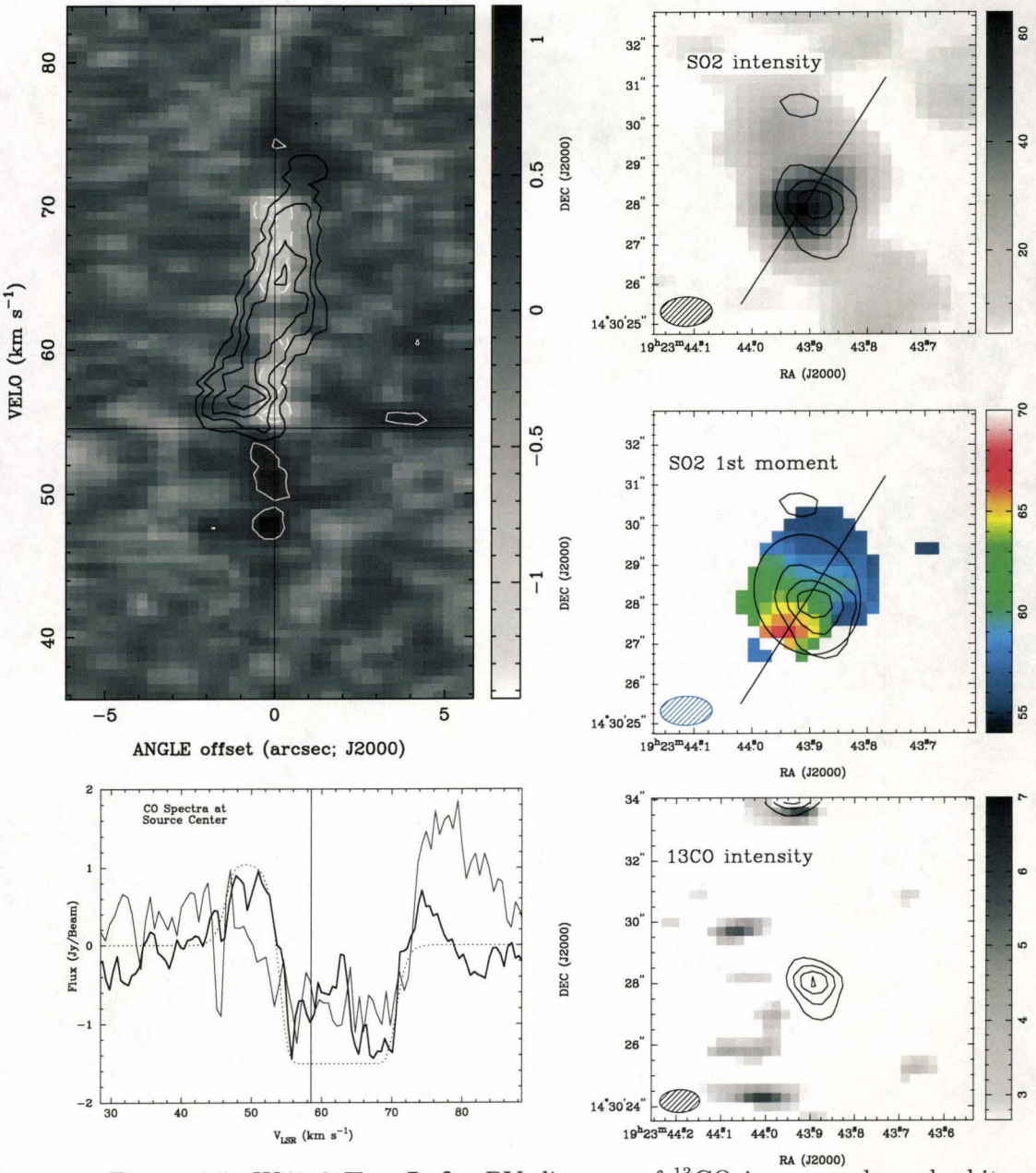

Figure 4.5: W51e8 **Top Left:** PV diagram of ^{13}CO in grayscale and white contours and SO_2 in black contours. Both sets of contours start at 3σ (0.23 Jy/beam), and increase (or decrease) in intervals of 2σ. **Bottom Left:** ^{12}CO (grey) and ^{13}CO (black) at the peak of the continuum emission. **Top Right:** Integrated intensity of SO_2 starting at 3σ (4.5 Jy/Beam km/s) with continuum contours starting at 7σ (0.4 Jy/beam) and increasing in intervals of 7σ. **Middle Right:** First moment map with continuum contours and an ellipse showing the deconvolved SO_2 emitting region. **Bottom Right:** ^{13}CO integrated intensity cut at 3σ (2.67 Jy/Beam km/s) with continuum emission contours.

Chapter 5

High Resolution Molecular Line Observations of Massive Star Forming Regions II: Outflows

This chapter is soon to be submitted to the Astrophysical Journal as an article titled "High Resolution Molecular Line Observations of Massive Star Forming Regions II: Outflows". By P.D. Klaassen, C.D. Wilson, E.R. Keto and Q. Zhang.

5.1 Introduction

The mechanisms responsible for the formation of high mass stars (see, for instance Zinnecker & Yorke, 2007) are not nearly as well constrained as those for lower mass stars (see, for instance Evans, 1999). However, one phenomenon that appears to be ubiquitous in regions forming stars of all masses is the outflow of gas from the star forming region. Through characterizing the kinematics of the outflowing gas surrounding the formation sites of massive stars, we can begin to constrain the formation mechanisms which can produce these large scale phenomena (i.e. how much gas is accelerated into the outflow and how much energy is required to power it). Once gas kinematics are determined for a number of sources, we can begin to constrain models of star forming outflows, and thus constrain models of massive star formation.

Outflows act as an important release mechanism for the buildup of angular momentum in star forming regions on all scales. The outflows observed in nearby low mass star forming regions can be quite collimated, while collimation factors in higher mass star forming regions do not appear to be as high. This has led some authors to suggest that intermediate and high mass stars evolve up the main sequence (i.e. Keto & Wood, 2006), and that the outflows lose collimation because they are older and the outflow has had more of a chance to

widen into the surrounding medium (i.e. Beuther & Shepherd, 2005). Indeed, there are no observations to date of highly collimated outflows for sources with luminosities greater than 10^5 $L_\odot$ (masses greater than O7 main sequence stars; McKee & Ostriker, 2007). However, it should be noted that the highest mass stars are intrinsically further away, and so it is unclear whether there is an observational bias introduced by the limiting resolutions and sensitivities of current interferometers.

The angular resolution possible with a filled aperture (i.e. single dish) telescope is severely limited by the physical size of the antenna as compared to the wavelength being observed ($\theta = 1.22\lambda/D$). Interferometers circumvent this problem by placing multiple antennae at large distances from each other. The longer the baselines between two antennae, the higher the resolution of the observations, but there is a trade off in sensitivity due to the limits in the coverage of the UV plane. Because interferometers are not filled aperture telescopes, they cannot detect the full power from a source, and the largest scale structures to which they are sensitive is a function of how closely the antennae can be packed (i.e. the shortest baseline). The full power signal can be added in later by combining interferometer observations with those from a single dish telescope which, ideally, has at least twice the diameter of the individual interferometer antennae. For example, the James Clerk Maxwell Telescope (JCMT) is well suited (at a diameter of 15 m) to provided zero spacing information for a dataset obtained at the Submillimeter Array (SMA, with 6 m dishes) assuming emission is extended beyond the size scales to which the SMA is sensitive.

When the SMA is in its extended configuration, most of the flux from structures on scales less than $\sim 10''$ is recovered, and there is no need to fill in the missing flux for these small scale structures. Pervasive molecules such as CO tend to exist in large scale structures. Thus, when observed by the SMA in this configuration, most of the flux is filtered out, and we require the addition of single dish data to recover it.

Here, we present 1mm observations of CO towards five massive star forming regions obtained with the SMA in its extended configuration, as well as JCMT observations for the same sources which were combined with the SMA data. In Section 5.2 we present our observations and image combination method while we present the results of our kinematic studies in Section 5.3. In Sections 5.4 and 5.5 we discuss our results and conclude.

5.2 Observations

Observations were obtained at the Submillimeter Array (SMA) in 2005, and the James Clerk Maxwell Telescope (JCMT) in October 2006. The observations obtained at the SMA are part of the same dataset as the observations

Source	RMS noise (Jy/Beam)			Tsys[a]	Outflow Age[c]	
	SMA	JCMT[b]	Combined	(K)	$\times 10^4$ (yr)	ref[d]
G10.6	0.32	1.67	0.40	341	5.7	1
G28.20	0.19	2.17	0.19	361	1.4	1
NGC7538	0.12	1.97	0.19	439	4.2[e]	2
W51e2	0.23	3.31	0.33	444	12	1
W51e8[f]	0.23	3.31	0.33	444	12	1

[a] System temperatures for JCMT observations
[b] Data regridded to SMA resolution
[c] Ages are assumed to be uncertain by 20%
[d] 1 - These observations, 2 - Davis et al. (1998)
[e] Using the same method to determine the age of the outflow in NGC 7538 gives an age of 1.2×10^4 yr.
[f] outflow age for W51e8 is assumed to be the same as for W51e2

Table 5.1: SMA and JCMT Observation Characteristics

presented in Chapter 4, and the pointing centers, integration times, system temperatures and synthesized beam sizes are presented in Tables 4.1 and 4.2.

^{12}CO (J=2-1) was observed at the JCMT using RxA. 7×7 pixel raster maps with 10″ spacing were obtained at a spectral resolution of 0.63 km s^{-1} and a bandwidth of 1 GHz. The angular resolution of the JCMT at this frequency is 20″, and thus we present Nyquist sampled observations. The maps each took one hour to complete (each point was observed for 74 seconds), the data were recorded using the antenna temperature flux scale, and then corrected into a main beam temperature using the main beam efficiency of the JCMT ($\eta_{\rm MB} = 0.69$). These intensities were later converted to Jy using a conversion factor of 26.44 (K/Jy = $15.6/\eta_{\rm ap}$, where $\eta_{\rm ap} = 0.59$). System temperatures during the observations and RMS noise limits (at a resolution of 0.5 km/s for the SMA, and 0.63 km/s for the JCMT and combined data) are given in Table 5.1. For each source, multiple JCMT raster maps were coadded, and linear baselines were removed. Data reduction was completed using the JCMT Starlink software, and the data cubes were exported into the MIRIAD data format for combination with the SMA data.

5.2.1 Combining Datasets

The SMA extended array observations are sensitive to structures from $\sim 25 - 150$kλ, corresponding to size scales of $\sim 1 - 10''$ at 230 GHz. At the same frequencies, the 15 m JCMT dish is sensitive to structures larger than $\sim 20''$ (or smaller than 15 kλ) up to the angular size of the mapped region. Thus,

we have a gap in our UV coverage (from 15 to 25 kλ) for these observations.

During the formation of stars of all masses, the angular momentum releasing outflows can become quite extended. In the study of Wu et al. (2004), only two sources (one classified as high mass, and one classified as low mass) have angular sizes of less than 6″ (see their Figure 3), and at most, six of the 397 sources in their study would have observable in the $< 10''$ scales to which our SMA observations are sensitive. For each dataset presented here, our JCMT observations show strong emission features with large line widths while our SMA observations only show coherent emission at high velocities with respect to the local standard of rest source velocity (See Figures 5.7 and 5.8).

Despite the large bandwidth of the SMA observations (2 GHz in each sideband), we only obtained JCMT observations for the 1 GHz bandwidth surrounding the CO line. As part of the JCMT data reduction process, a linear baseline was removed from each spectrum, and in order to match the baseline subtracted JCMT observations, the continuum emission was subtracted from the SMA observations as well (using the MIRIAD command `UVLIN`).

There are a number of ways of combining single dish and interferometer data, and we applied two image plane combination techniques to our data in order to determine which would produce the most accurate combination. Our datasets were combined using both linear and non-linear combination techniques (MIRIAD commands `IMMERGE` and `MOSMEM` respectively). In general, linear image combination techniques are best suited to datasets in which the emission is not very extended, while non-linear techniques are generally better for datasets with extended emission. For our datasets, where there is significantly more emission in the JCMT maps than the SMA maps, we found the non-linear maximum entropy method worked best at combining our datasets. Thus, the ^{12}CO maps presented here were produced from combining the SMA and JCMT data using the MIRIAD command `MOSMEM`, and then restored with the MIRIAD command `RESTOR` using the SMA dirty image and the combined map from `MOSMEM` as a model for the clean components. See Appendix C for a detailed description of the image combination methods we used.

Combining the SMA and JCMT data significantly increased the sensitivity to outflowing material in our observations. For example, the SMA only CO emission from NGC 7538 IRS1 was seen in only a few small ($< 3''$) structures at a peak detection of 7σ. Previous observations of the same molecule (but in the J=1-0 transition) were made using the Nobeyama 45m telescope by Kameya et al. (1989), and a clearly bipolar morphology was seen on 16″ scales. A similar morphology was seen at 3″ resolution by Pratap et al. (1990). After combining the SMA and JCMT data, the outflow is observed with $> 20\sigma$ detections over much of the SMA primary beam, with significant blue shifted emission towards the north west, and significant red shifted emission towards the south east, the same orientation as the previously detected outflow.

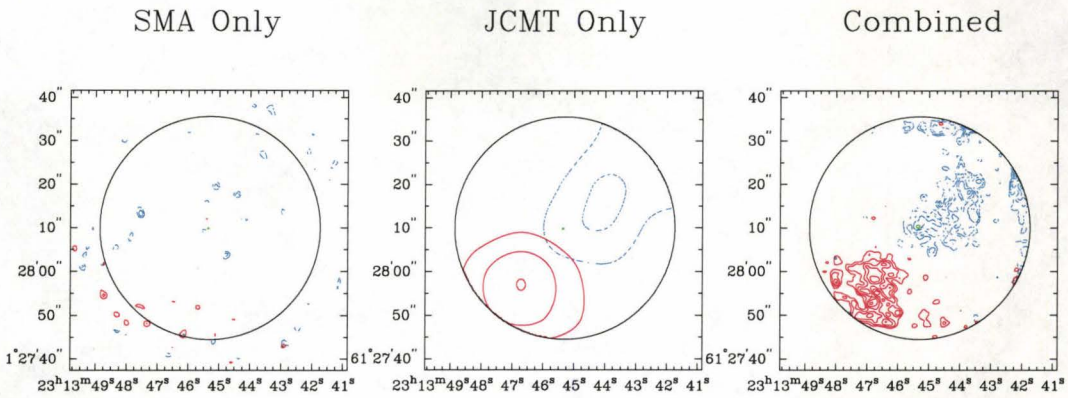

Figure 5.1: Interferometer (SMA) and single dish (JCMT) observations of ^{12}CO towards NGC7538 IRS 1. Using a non-linear image combination technique (the MOSMEM command in MIRIAD), we were able to combine the data from the two telescopes, resulting in the panel on the right. The contours for the blue (-74 to -65 km s^{-1}, dashed contours) and red (-45 to -34 km s^{-1}, solid contours) start at 6σ, and increase in intervals of 3σ for the individual map. The green contours in the center of each image represent the 230 GHz continuum emission from IRS 1. The large circle in each panel represents the 45% gain limits of the SMA at 230 GHz. Figure reproduced from Klaassen & Wilson (2008a)

In Figure 5.1 we show the single dish, interferometer and combined maps of the red and blue outflow lobes in NGC 7538 IRS1 (integrated over the same velocity ranges, with the JCMT dataset regridded to the resolution of the SMA dataset) to show how the combination of the two dataset improved our observations.

5.3 Results

The line full widths at zero power (FWZP) of CO in our sources, when averaged over the entire outflow area, are comparable to, but slightly smaller than the FWZP of the H30α lines presented in Keto et al. (2008), suggesting a possible correlation between the terminal velocities in an outflow and the velocity of the ionized gas in the HII region (since H30α does not suffer from pressure broadening, Keto et al., 2008).

^{12}CO is very abundant in the ISM, and can be excited into some of its lowest rotational energy states (i.e. J=1 or J=2) at the fairly low temperatures (5 and 10 K) that can be reached in molecular clouds. Bulk motions of the gas, such as the material entrained into an outflow from a forming star, can thus be

traced on large scales by CO emission. With our combined interferometer and single dish datasets, we can observe large scale structures at high resolution.

The high abundance of CO does make it an excellent tracer of high velocity and bulk gas motions; however, it does cause the line to become optically thick quite quickly. Thus, the outflow mass, momentum, kinetic energy, luminosity and mass loss rates calculated below are lower limits to their true values because we can only trace gas to the $\tau = 1$ surface. When calculating outflow mass (not total mass) and gas kinematics, we have used the integrated intensity of the line wing emission so that we minimize the problems arising from higher line opacities in the line center.

To determine both the outflow masses (in both the red and the blue lobes) assuming optically thin ^{12}CO in each region, we created integrated intensity maps (zeroth moment maps) of the red and blue shifted emission for each source (the velocity ranges of which are given in the captions of Figures 5.3, 5.4, 5.5, and 5.6). These maps were then masked to their respective 3σ limits, and the masked maps were used to determine source properties. To set lower limits on the total gas mass in these regions (i.e. the mass of the optically thin gas), we also created zeroth moment maps, but we integrated over the full line width instead of just the line wings.

From these integrated intensity maps, we determined the average flux within the specified velocity range. This value was then multiplied by a scaling factor similar to those described in previous chapters to determine the average column density of CO (N=$1.3 \times 10^{15} \int TdV$ cm^{-2}/K km s^{-1}). This scaling factor includes the partition function to extrapolate from our one rotational transition of CO to the total column density of CO under the assumption of local thermodynamic equilibrium. To calculate the partition function, we need to assume an ambient temperature. Since SO_2 has been detected towards each source (Chapter 4), and it is generally only observed in regions where the temperature is greater than 100 K (Doty et al., 2002; Charnley, 1997), we have set the ambient temperature to 100K for our calculations. We note that increasing the temperature by a factor of two also increases our column densities by a factor of two.

Having determined the average column density within the emitting region, we multiplied by the area of the emitting region to determine the total number of CO molecules that are emitting. This value was then divided by the abundance of CO with respect to H_2 and the mass of the H_2 molecule to obtain the mass of optically thin material.

To determine the outflow momentum, we multiplied the zeroth moment map by the first moment map for the same velocity range (either for the red or blue shifted emission). A first moment map is a velocity weighted integrated intensity map ($\sum I*v/\sum I$), and thus, when multiplied by the zeroth moment map ($\sum I$) is proportional to the momentum at each velocity. This value, when

Source	Mass ($M_\odot$)		
	Red	Blue	Total
G10.6	11.75±0.03	14.66±0.04	148.8±0.03
G28.2	8.11±0.04	2.28±0.01	13.00±0.04
NGC 7538	0.508±0.002	1.123±0.005	17.73±0.03
W51e2	0.64±0.01	1.24±0.05	18.3±0.1
W51e8	0.59±0.01	0.355±0.008	19.5±0.1

Table 5.2: Outflow and Ambient Masses. Listed uncertainties reflect measurement uncertainties. A 20% calibration uncertainty is not included in the uncertainties listed.

Source	Momentum ($M_\odot$ km s^{-1})		$\dot{M}_{out}$ ($\times 10^{-5}$ $M_\odot$/yr)	
	Red	Blue	Red	Blue
G10.6	99.6±0.1	100.3±0.1	21±4	26±5
G28.2	78.25±0.09	18.95±0.03	58±12	17±3
NGC 7538	8.97±0.02	9.44±0.01	1.2±0.3	2.7±0.6
W51e2	15.2±0.2	24.5±0.9	0.5±0.1	1.0±0.2
W51e8	13.4±0.3	6.8±0.3	0.5±0.1	0.29±0.06

Table 5.3: Outflow Momentum and Mass Loss Rates. Assumed calibration uncertainty of 20% is not included in these numbers.

multiplied by the scaling factor between integrated intensity and mass gives the outflow momentum (const $* \sum I * v = Mv$).

The kinetic energy in a given outflow lobe can be determined from the mass in that lobe, and its momentum, since $E = P^2/2M$. Thus, the kinetic energy in each outflow lobe has been derived using the masses and momenta listed in Tables 5.2 and 5.3. The outflow luminosity can then be estimated if the age of the outflow is known. For four of our sources (all but NGC 7538), we found a kinematic age for our outflows using the extent of the outflowing gas, and the velocity of that gas. For NGC 7538, an outflow age was previously determined by Davis et al. (1998). Our calculated outflow age for NGC 7538 was $\sim$ 4 times smaller than that derived by Davis et al.. We chose to use their value for the outflow age since the outflow appears to be more extended than our primary beam; we are thus not seeing the full extent of the outflow and our derived age would be an underestimate. These ages are presented in Table 5.1, while the outflow kinematics are presented in Tables 5.2 - 5.4.

For each source in which an outflow was detected, the orientation of the outflow on the plane of the sky is perpendicular to the rotation axis of the hot gas (as traced by SO_2) surrounding each HII region (see Chapter 4). The

Source	Energy ($\times 10^{44}$ erg)		Luminosity ($L_\odot$)	
	Red	Blue	Red	Blue
G10.6	84.4±0.4	68.6±0.3	1.2±0.3	0.9±0.2
G28.2	75.5±0.5	15.7±0.1	4.5±0.9	0.9±0.2
NGC 7538	15.8±0.1	7.94±0.05	0.31±0.06	0.15±0.03
W51e2	36±1	48±5	0.24±0.06	0.3±0.1
W51e8	31±2	13±1	0.20±0.05	0.09±0.02

Table 5.4: Outflow Mechanical Energy and Luminosity. A calibration uncertainty of 20% is assumed, but not included in the presented uncertainties.

outflow kinematics, shown in Tables 5.2 - 5.4, are all within the ranges for these values listed in Wu et al. (2004) and towards the average values they show for high mass star forming regions (those shown with open squares in their Figures). We note that only one of our sources is coincident with their study (NGC 7538), and that our derived outflow kinematics are similar to their results.

From the outflow ages listed in Table 5.1 and the masses calculated above, we can determine the mass loss rates for each source. For each of our sources, the mass outflow rates are greater than the values generally seen in lower mass star forming regions (which are of order 10^{-8} $M_\odot$ yr^{-1} Shepherd, 2003). Assuming the amount of mass in the outflow scales proportionally to the amount of mass infalling onto the star (Beuther et al., 2002), then we would expect larger mass outflow rates than for lower mass stars since the masses of the outflows are larger, and the timescale over which the outflow is active is shorter.

5.3.1 Results for Individual Sources

With a source luminosity of 9.6×10^4 $L_\odot$ (Kraus et al., 2006), NGC 7538 is our best example of a large scale, fairly well collimated outflow. For NGC 7538 IRS1, the velocity ranges of the red and blue outflow lobes start at 15 and 5 km s^{-1} (respectively) from the rest velocity. That the outflow velocity cutoffs are so far from the source velocity explains why the outflow masses for this region are so much smaller than the total mass which is integrated over the entire map. For the NGC 7538 region, this means that IRS 2 and IRS 3 (which are both projected within the blue lobe of the IRS1 outflow) are both included in the mass estimate.

Assuming a B0 star is responsible for the HII region in W51e2 (Mehringer, 1994), the region has a luminosity of at least 5×10^4 $L_\odot$. The outflow lobes observed towards this source are much smaller (on the plane of the sky, but could be larger along the line of sight) than the NGC 7538 region and the

velocity ranges are much higher. The same is true for the W51e8 region which is suggested to be powered by a slightly more massive star (Mehringer, 1994). The smaller angular sizes and higher outflow velocities suggest that these outflows are oriented closer to the line of sight than they are the plane of the sky. Note that in the W51e8 case, if the blue shifted emission towards the north-east of the source is an outflow lobe, it is unclear why it is on the same side of the HII region as the red shifted lobe which is perpendicular to the SO2 velocity gradient (Klaassen et al., 2008a). If there were a wind pushing on this outflow from the west (i.e. from the W51e region itself), it might explain why the red and blue outflow lobes appear to be on one side of the HII region; the outflow is primarily along the line of sight, and the wind is pushing it away from the HII region. It is also possible that this is a monopolar outflow, that only one outflow lobe was able to push through the surrounding medium to grow to observable scales (as has been observed by Chernin & Masson, 1991, in the HH46-47 region).

That the morphologies of the two outflows of the W51e region in the combined (SMA + JCMT) map are similar to those seen in the SMA only maps suggests that the two datasets might not be combined properly (due to the gap in the UV coverage). This can be fixed by re-observing these sources with the SMA in its more compact configuration, and combining those data with the two datasets we currently have (we hope to obtain these observations in the summer/fall of 2008). This region is the only one in our sample in which there are multiple, resolved HII regions in the interferometer map which are unresolved in the single dish map. The implications of resolved vs. unresolved outflow powering sources are described further in Section 5.4. Between the e8 and e2 sources is W51e4 (see Zhang et al., 1998, for its position), which does not appear to have any high velocity gas indicative of an outflow.

The combined map of G28.2 does show a spatial offset between the red and blue shifted material; however these 'outflow lobes' are offset from the continuum source (see Figure 5.4) by approximately 2.5″, which is a slightly larger offset than the pointing accuracy of the JCMT (2″). It is unclear why the outflow is offset from the continuum source. Of the sources presented here, this dataset is the one with the largest gap in UV coverage between the SMA and JCMT. For this source, the UV coverage of the SMA observations is 35-135 kλ, while the JCMT, with a diameter of 15 m, can only observe structures on size scales from 0 to $\sim$ 20 kλ (see the top right panel of Figure 5.2).

There appears to be a spatial offset between the red and blue shifted emission in the JCMT only map of G10.6; however, since this source was not at the pointing center of the SMA observations, much of the emission from the blue lobe is cutoff by the primary beam of the SMA observations (which was also set as the edge of the JCMT map). We could not determine a coherent outflow structure from this source from our observations; however, this conclusion may

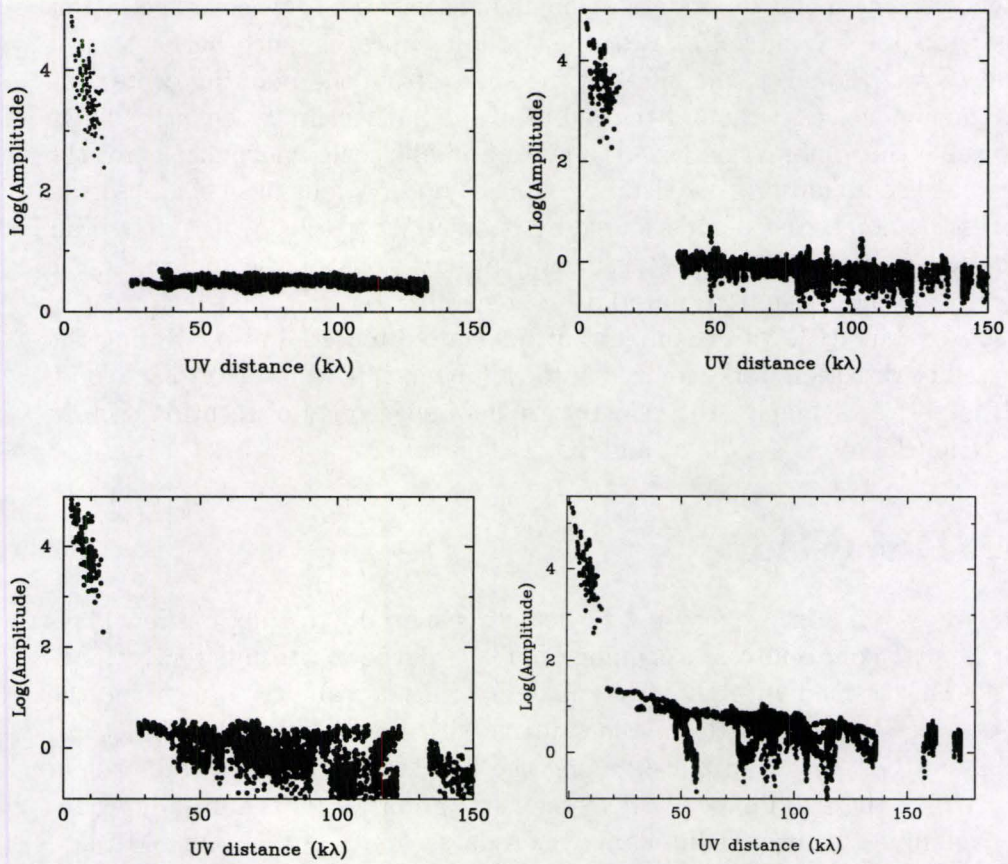

Figure 5.2: UV distances covered by the combination of the JCMT and SMA datasets. In each case, there is a gap in the JCMT visibilities and the SMA visibilities. In each case, the JCMT visibilities are the high amplitude ones with uv distances less than $\sim$ 15 kλ, and the SMA visibilities are the ones with uv distances greater than that. The UV coverages are presented for NGC 7538 (top left), G28.20 (top right), G10.6 (bottom left) and both regions in W51e (bottom right).

change with the inclusion of data at medium scales. The UV coverage in this dataset (25-150 kλ and 0-15 kλ for the two telescopes) is much better than it was for G28.2; however, the offset of the source from the pointing center (by $\sim 12''$, a significant fraction of the radius of the SMA primary beam) is likely responsible (in combination with the lack of middle scale information) for the poor image combination. A redshifted, ionized outflow lobe has been observed towards the north east of this source by Keto & Wood (2006) in H66α. Our much larger scale (i.e. single dish only) observations of the molecular gas suggest that the redshifted material lies generally towards the south west of this source, but with a large amount of red shifted material also covering the source. The direction of the ionized outflow lobe in this region (Keto & Wood, 2006) is perpendicular to the velocity gradient suggestive of rotation seen in both NH_3 (Sollins et al., 2005) and SO_2 (Klaassen et al., 2008a).

5.4 Discussion

There are two reasons we may not be detecting spatially distinct outflow lobes towards all of our sources, assuming that the outflows are inherently bipolar: the lack of medium scale fluxes is hampering our ability to combine the datasets, or the outflows from the sources with no clear bipolar structures (G28.2 and G10.6) are primarily along the line of sight and we cannot spatially resolve the two lobes. While these two options are not mutually exclusive, combining a third, medium scale SMA dataset with our current SMA and JCMT observations would resolve this ambiguity.

With more observations of the HII regions in the W51e region, we will be able to determine which of the HII regions within the primary beam is responsible for the large scale structures observed in the JCMT only maps. This will address the problem common to single dish observations of high mass star forming regions as to whether the strongest continuum emitter is responsible for the outflows, or whether all of the HII regions within a small region contribute equally. The single dish only map (see the bottom right hand panel of Figure 5.8) of this region shows that both the red and blue shifted emission is centered south of *both* HII regions. With single dish only data, the outflowing structures associated with the W51e region would have completely missed the small scale (but bright) outflowing emission from the W51e8 and W51e2 regions.

When we identified outflows here at high resolution (i.e. emanating from NGC 7538 IRS1, and both W51e regions), we are observing single outflows (whether bipolar or monopolar) which can be traced back to a single HII region. That there is only one outflow suggests that there is one dominant outflow driving source within each HII region. That the emission is traceable to the edges of the HII region suggests that this driving source is launching

the outflow from inside (or very close to the edge of) the HII region.

That we are seeing signs of infall of molecular gas onto these regions (Klaassen et al., 2008a) suggests that these outflows are still being powered, and that there is a long lived period of (ionized?) accretion beyond the formation of the HII region.

5.5 Conclusions

We have observed ^{12}CO (J=2-1) at the SMA and JCMT and have combined the two datasets using a maximum entropy method. From these combined datasets, we have placed constraints on the outflowing gas mass and kinematics. We find that these values agree with the values suggested for high mass star forming regions, with the exception of our derived mechanical luminosities, which are unusually high.

We find that when we can trace outflow morphology, we see outflows which appear to emanate from the surfaces of the HII regions, suggesting that they are being driven from within the HII region. Further observations, covering medium scale structures are required to confirm or deny the presence of molecular outflows in G28.2 and G10.6.

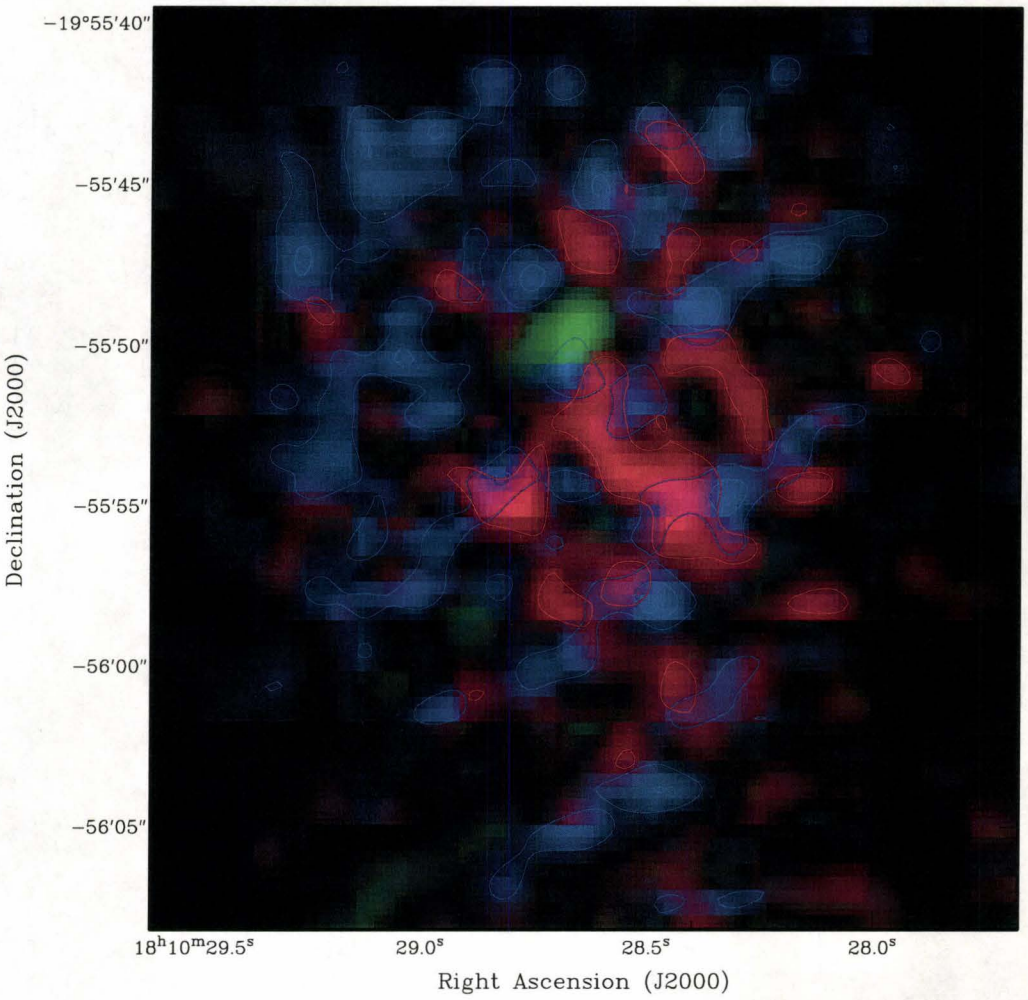

Figure 5.3: ^{12}CO emission towards G10.6 combined from the SMA and the JCMT. The red and blue halftones show the integrated intensities over the velocity ranges 3 to 12 km s^{-1} and -17 to -8 km s^{-1} (respectively) and are cut at 3σ (5.85 and 5.23 Jy, respectively). The contours start at 5σ, and increase in intervals of 3σ. The continuum emission is also cut at 3σ (0.074 Jy).

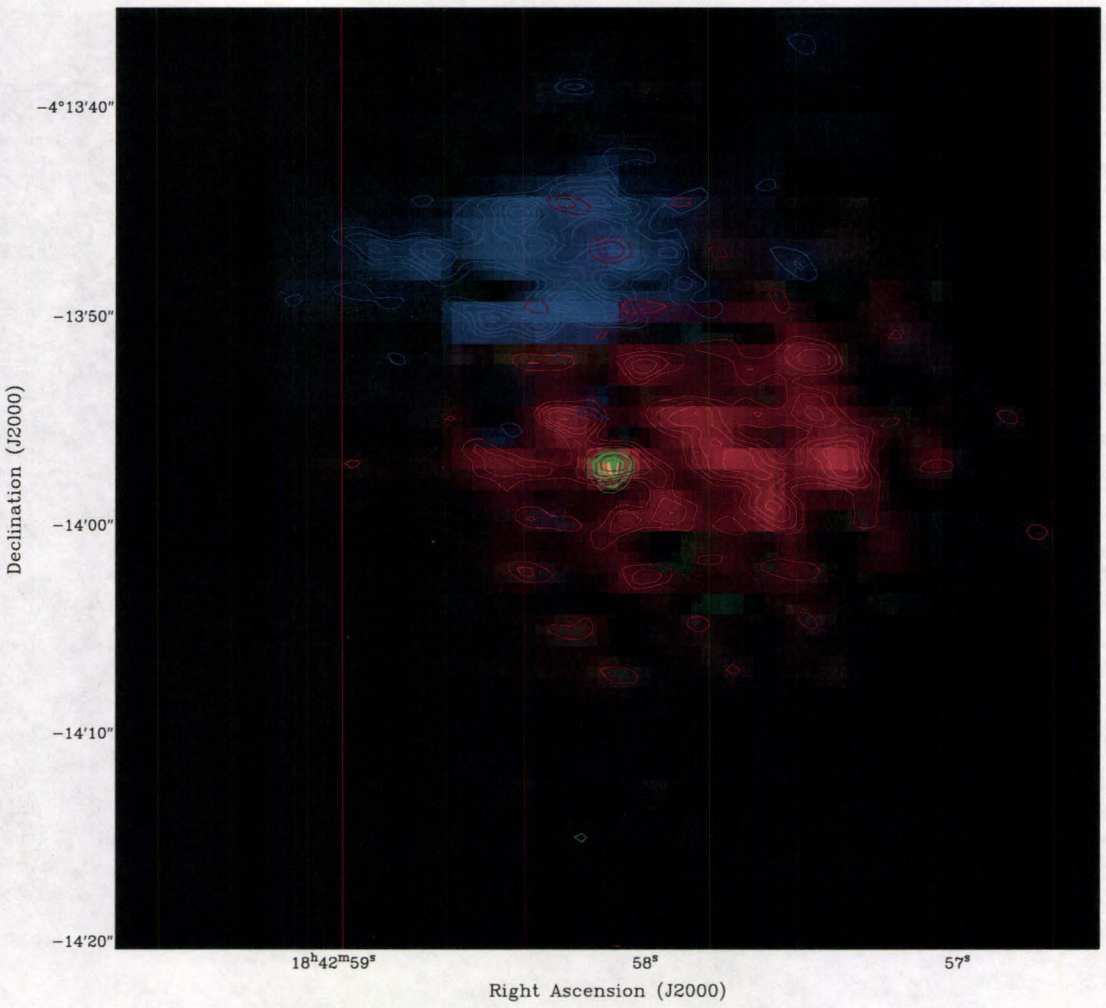

Figure 5.4: ^{12}CO emission towards G28.20 combined from the SMA and the JCMT. The red and blue halftones show the integrated intensities over the velocity ranges 98 to 120 km s^{-1} and 84 to 92 km s^{-1} (respectively) and are cut at 3σ (7.05 and 3.3 Jy, respectively). The contours start at 5σ, and increase in intervals of 3σ. The continuum emission is also cut at 3σ (0.03 Jy).

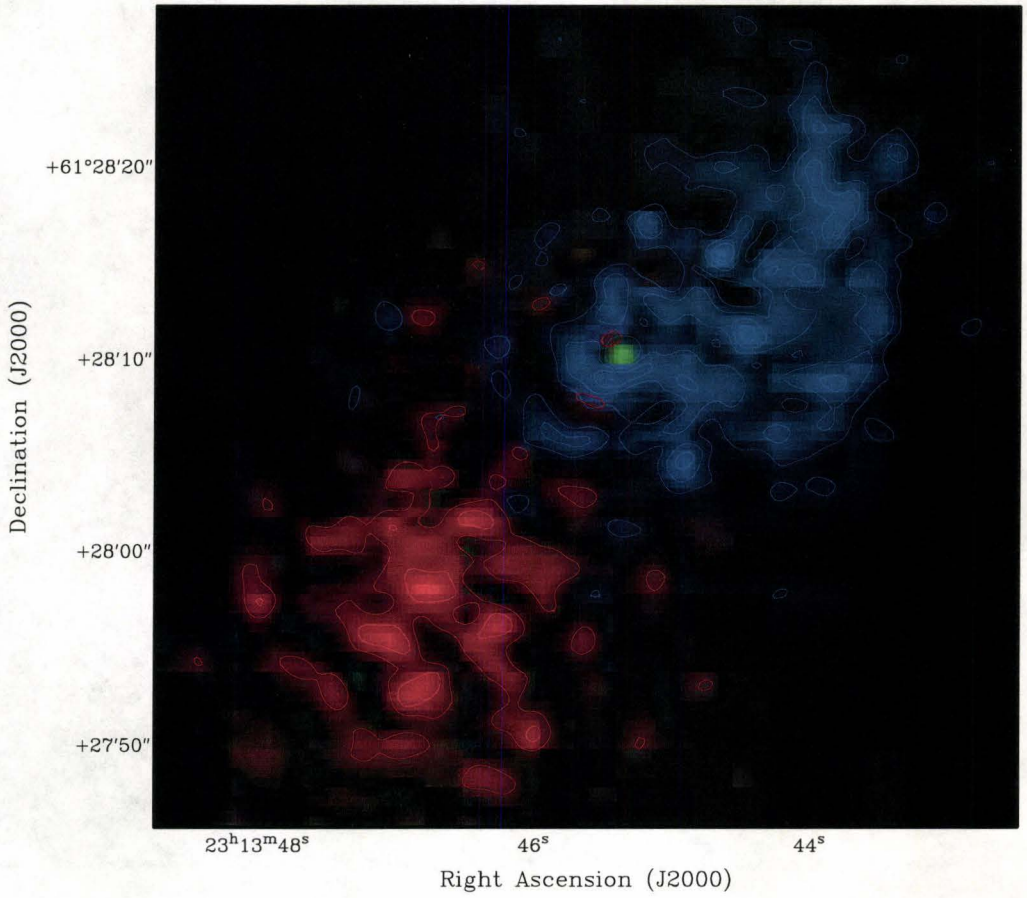

Figure 5.5: ^{12}CO emission towards NGC7538 IRS1 combined from the SMA and the JCMT. The red and blue halftones show the integrated intensities over the velocity ranges -45 to -34 km s^{-1} and -74 to -65 km s^{-1} (respectively) and are cut at 3σ (1.74 and 1.68 Jy, respectively). The contours start at 5σ, and increase in intervals of 3σ. The continuum emission is also cut at 3σ (0.107 Jy).

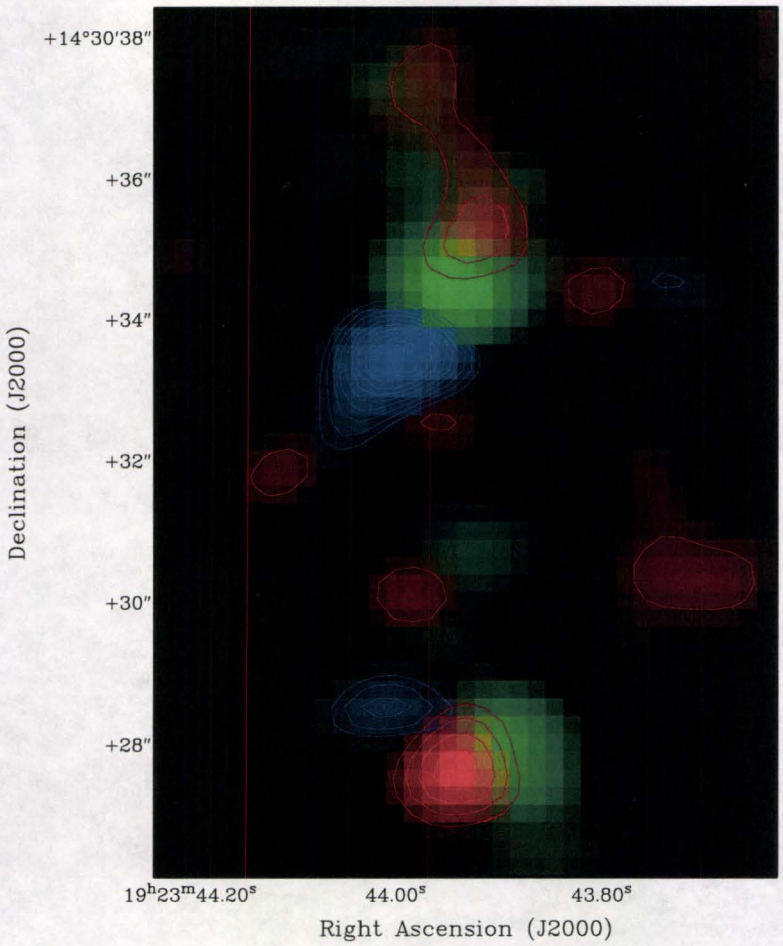

Figure 5.6: ^{12}CO emission towards W51e2 and W51e8 combined from the SMA and the JCMT. The red and blue halftones show the integrated intensities over the velocity ranges 73 to 86 km s^{-1} and 22 to 44 km s^{-1} (respectively) and are cut at 3σ (3.42 and 7.44 Jy, respectively). The contours start at 5σ, and increase in intervals of 3σ. The continuum emission is also cut at 3σ (0.192 Jy).

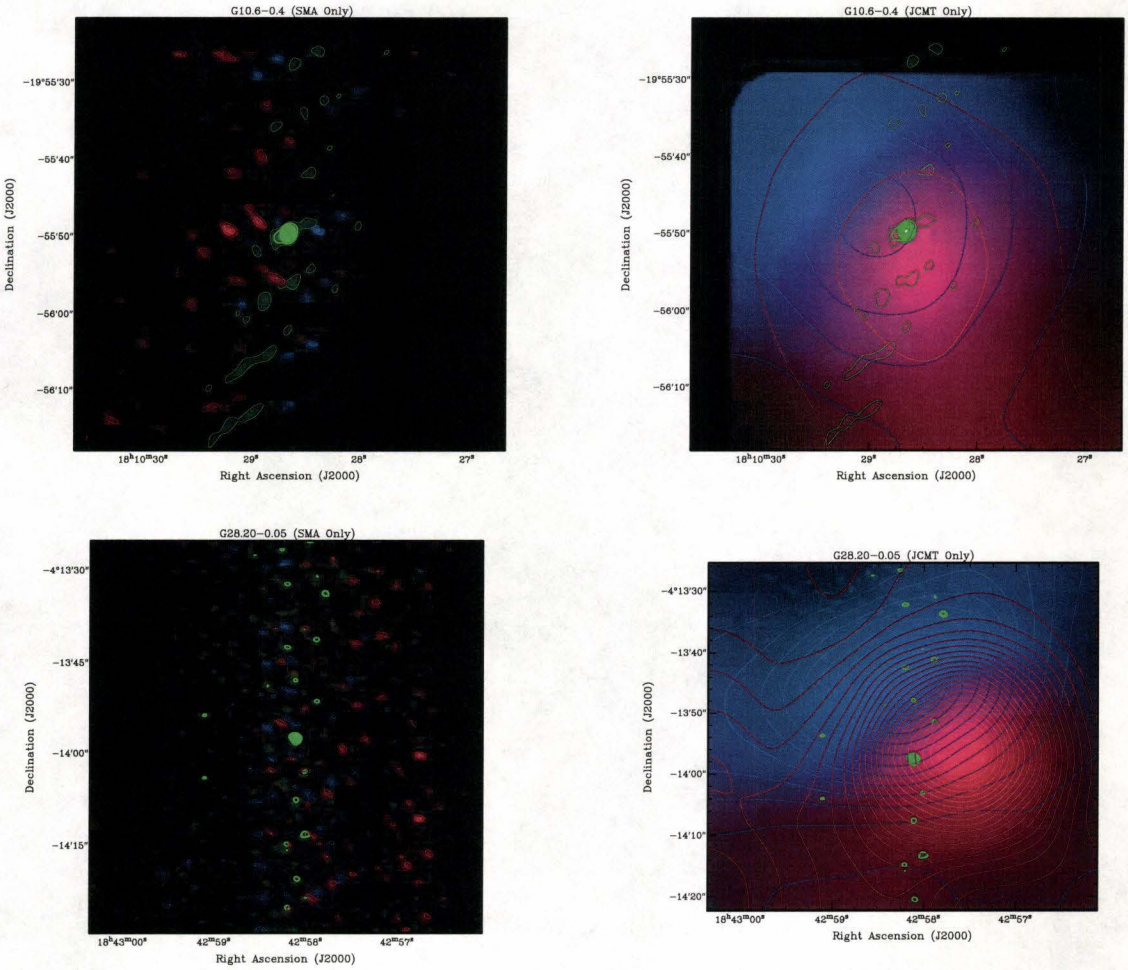

Figure 5.7: Interferometer and Single dish only maps of G10.6-0.4 and G28.20-0.05. The same velocity cutoffs were used in the maps for the same source, and these velocities match the cutoffs listed in the captions of Figures 5.3 and 5.4. The color scales cutoff at 3σ, and the contours start at 5σ, increasing in intervals of 5σ.

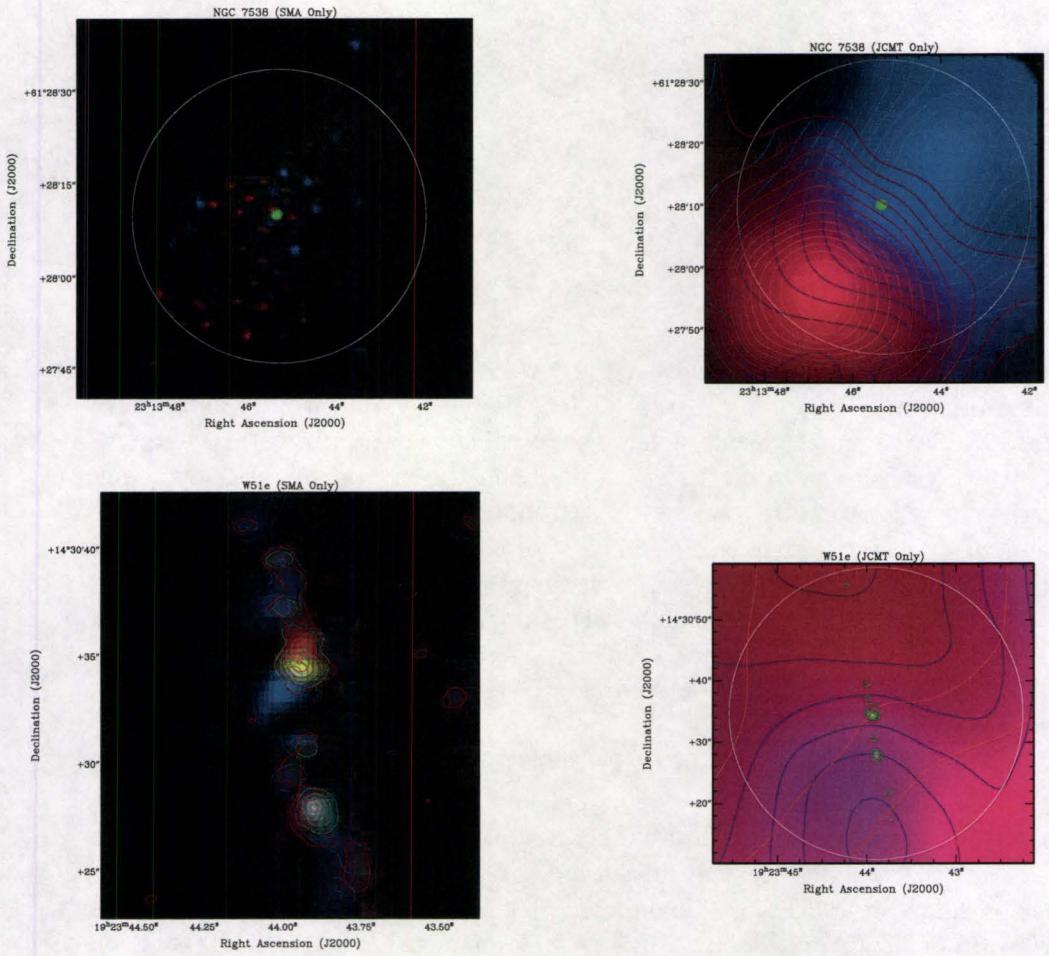

Figure 5.8: Interferometer and Single dish only maps of NGC7538 IRS1 and the two sources observed in the W51e region. The same velocity cutoffs were used in the maps for the same source, and these velocities match the cutoffs listed in the captions of Figures 5.5 and 5.6. The color scales cutoff at 3σ, and the contours start at 5σ, increasing in intervals of 5σ. When present, the white circle represents the primary beam of the SMA observations (where the gain is 50% of the maximum).

Chapter 6

Conclusions

As stated earlier (see Section 1.2.3), an evolutionary sequence for high mass star formation is beginning to take shape. We understand that as a massive protostar heats up, it forms a hot core, which, as the protostar continues to evolve, transitions into an HII region when the protostar burns hydrogen brightly enough to start ionizing its surroundings. What is not clear is how the dynamical processes involved in star formation change once the protostar transitions from intermediate mass (hot core) to a massive (HII region) star. Does accretion continue onto the massive protostar after the formation of an HII region despite the large outward thermal and radiation pressures (i.e. Keto, 2007)? Or are the outward pressures strong enough to halt accretion (i.e. Klaassen et al., 2006)?

As the protostellar region began to collapse, there was some intrinsic angular momentum present in the cloud. This angular momentum causes the gas to rotate and flatten (into a disk like structure) as the collapse progresses. The release of this angular momentum is what is responsible for the bipolar molecular outflows observed from star forming regions as well. While detections of disks around high mass protostars are still somewhat controversial, rotation of the gas surrounding the HII regions would suggest that there may be a disk within the HII region itself. The fairly ubiquitous presence of outflows in regions forming stars of all sizes not only suggests a common formation mechanism for low and high mass stars (Pudritz et al., 2007, see, for instance,), but through characterizing their kinematics and morphologies, we can begin to constrain how they are being powered, and what source is responsible for these outflows.

In what follows, we discuss the conclusions reached in the last few chapters, and the broader implications of this work for understanding the processes responsible for the formation of massive stars.

In Chapter 2 we showed single pointing spectra towards 23 massive star forming regions in both an outflow tracer (SiO) and a molecular species which

can often be used as an infall tracer (HCO^+ and $H^{13}CO^+$).

From these observations, we found that half of the sources which showed evidence for outflow activity also showed evidence for ongoing infall activity. For those sources which did not show evidence of outflows (nine out of our 23 sources), we suggest it was because the outflows stopped shocking their environments at least 10^4 years ago, and the SiO produced in protostellar outflows has evolved into the unobservable SiO_2. Our HCO^+ observations showed line wing emission towards every source, suggesting that while we may not always observe SiO, there is outflow activity in each source. It is quite possible that the sources with outflow detections in HCO^+ and not in SiO are regions in which the observable outflows are, indeed, remnants of previous accretion and outflow.

This suggests that perhaps there is a stage of ionized accretion after the HII region forms, but it also appears that the conditions indicative of halted accretion (i.e. remnant outflows) can also be observed, and that outflows can be continued to be observed after their powering sources have turned off.

In Chapter 3 we presented maps of seven massive star forming regions in the same molecular tracers as those used to observe 23 sources in Chapter 2. These observations were undertaken in order to understand the larger scale structures involved in star formation, and determine whether single pointing observations are sufficient for determining whether infall and outflow are ongoing in massive star forming regions.

From mapping a number of regions, we note that we do not need to modify the conclusions from Chapter 2, except for the detection of infall in one more source. That we do detect infall in one more source than was expected suggests that we can obtain better statistics on the kinematics of the gas surrounding massive protostars by producing small maps of this emission.

From our maps, we also find that infall, when detected, is extended on the sky. This suggests that where large scale infall onto a massive protostar exists, it should be detectable with a single dish telescope. Since with these observations we have now observed the entire infall region, we can quantify how much mass is falling in onto each region.

From mapping the outflowing gas, we find that the shocked regions are not, in general, very extended. But, from these observations, we can determine how much energy is required to accelerate the ambient gas to velocities high enough to shock its surroundings. From these energy estimates, we can place constraints on the properties of the powering source. We find that the energies required to accelerate the gas in these regions are consistent with a massive star; lower mass stars would not have enough energy to shock as much ambient material.

With single dish data, we can constrain properties such as energy and large scale infall masses, but we cannot determine which source within the large

single dish beam the material is falling onto, and which source is powering the the outflows observed on large scales.

In order to determine whether the large scale infall is onto the source which is powering the large scale outflow, or which individual source each process can be traced to, we need high resolution maps of the gas towards a number of high mass star forming regions.

In Chapters 4 and 5, we present high resolution, interferometer maps of the gas surrounding five massive star forming regions. In Chapter 4 we present interferometer only images of infall onto the HII regions (as traced by ^{13}CO) as well as rotation of the warm molecular gas around each HII region (as traced by SO_2).

We find infall signatures in four out of the five sources, and note that the fifth source, G10.6, has been previously confirmed as a source which is undergoing infall, in both ionized gas (Keto & Wood, 2006) and molecular gas (Sollins et al., 2005, and in Chapter 3). This suggests that molecular gas is still falling in towards each of these HII regions. Presumably, this small scale molecular infall transitions into ionized accretion once the gas passes the ionization boundary of the HII region. That ionized infall is seen by us and other authors towards each of these sources suggests that there is a period of continued accretion beyond the formation of an HII region with a statistically significantly long lifetime.

We also detect rotation of the warm gas surrounding each HII region. Since there is no expectation that these sources are uncommon in their rotation properties (i.e. the observed sources were not selected based on previous observations of rotation), these observations suggest that rotation of the gas directly outside the HII region is a common occurrence. If this rotation continues in, and the ionized gas in the HII region is also undergoing bulk rotation, this would suggest that the cloud from which the protostar is forming underwent a single collapse phase, and that the massive protostar is not due to the competitive accretion of a number of smaller protostellar fragments with random spin orientations. This would also suggest that there may be embedded disks within these HII regions which we cannot yet resolve with current interferometers.

The continuation of infall, once the protostar is already massive enough to form an HII region, and the bulk rotation of the gas around the HII region suggest that these massive protostars are forming in a manner similar to (but scaled up from) the way in which lower mass stars form.

In Chapter 5, we find that when we have been able to determine outflow morphology, we only see one outflow, and that outflow is a coherent outflow (i.e. not patchy) with only two lobes. This suggests that there is only one source responsible for each observed outflow. If multiple sources were responsible for these outflows, they could quite as easily be multipolar, since the powering sources would have random orientations with respect to each other.

For the outflows with clearly defined structures, we also find that we can trace the molecular emission onto the surface of the HII region. This suggests that the powering source for each outflow is within the HII region, and that the outflow is not originating from one of the surrounding hot cores or other, lower mass protostars in the region.

From these outflow observations, we conclude that there is a single HII region responsible for the observable large scale outflows seen in massive star forming regions, and that this source is within the HII region itself. That the SO_2 observed around W51e1 appears to have an outflow component in the PV diagram of Figure 4.5 indicates that the outflow in this region is emanating from within the shell of warm gas.

In each source observed with an interferometer (SMA), we are seeing infall beyond the formation of the HII region, and on the larger scales, in the sources we observed with a single dish telescope (JCMT), we are seeing large scale infall onto about half of our sources (although, some infall signatures could be diluted out of observability by velocity gradients across the source).

These observations lead us to conclude that infall continues well beyond the formation of an HII region for a statistically significant period of time, implying that there must be some method for overcoming the outward radiation pressures produced by the forming massive stars. We have also shown that the small scale gas kinematics (i.e. rotation and infall) we observe point towards accretion of material onto one central source, and that the large scale structures observed with single dish telescopes (like infall in HCO^+, and outflows in CO) can be traced back to the location of the largest member of the star forming cluster.

6.1 Future Work

6.1.1 High Resolution Observations of a Cluster of Massive Stars

K3-50A is a massive star forming region located at distance of 8.7 kpc in which there appear to be three massive stars powering the observed HII region. We have obtained VLA observations of ionized (H66α) and molecular (NH_3) gas in this region at a resolution of 0.3″. With these observations, we will be able to determine the gas kinematics within and surrounding this HII region on size scales comparable to the separation of the individual massive stars responsible for this HII region. Constraining the dynamics on these small size scales will help us to understand the interaction between infall and radiation pressure. In the 22 GHz continuum emission simultaneously observed with the H66α line, we see a flattened structure in the HII region in which two of the massive stars

are located and which is perpendicular to the position angle of the ionized outflow observed by Depree et al. (1994)

We are also in the process of obtaining SMA observations of SiO in this region at a resolution of $\sim 2.5''$. SiO, as shown in Chapters 2 and 3, is an excellent tracer of shocked gas, and with high resolution observations of shocked gas, we can determine whether the ionized outflow in this region is being collimated by the ambient gas. Previous SiO observations of this region (Howard et al., 1997) had a very low signal to noise ratio (7σ at line peak), and so it was unclear whether the detected SiO was tracing the edges of the ionized outflow, or associated with the flattened structure we see in the continuum images obtained at the VLA (see Figure 6.1).

6.1.2 Radiative Transfer Simulations of Outflows from Massive Stars

With high resolution observations of the outflowing gas from a number of massive star forming regions (as determined in Chapter 5), we can begin to constrain models of outflow generation in massive star forming regions.

We have modified the 3D radiative transfer code described in Keto (2007); Keto & Caselli (2008) in order to incorporate the velocity structures observed from different kinds of outflow generating mechanisms. We are in the process of modeling outflows which fall into three general categories: power law velocity fields (like those described in Keto, 1991; Cabrit & Bertout, 1986), turbulent jet entrainment (like those described in Lizano & Giovanardi, 1995), bow shock models (like those described in Masson & Chernin, 1993; Hatchell et al., 1999), and finally, wide angle winds (like those described in Lee et al., 2000; Canto et al., 1988).

6.1.3 Molecular Gas in Southern Massive Star Forming Regions

The dense conditions required to form massive stars mean that they must form within a few scale heights the galactic plane. Despite most of the galactic plane being observable from the southern hemisphere, we have not yet been able to quantify the gas dynamics or analyze the hot astrochemistry of southern massive star forming regions because of the lack of submillimeter telescopes in the southern hemisphere. Surveys of low energy molecular line transitions are possible with telescopes such as MOPRA, but in order to study the hot core chemistry in regions forming massive stars, we need to observe higher energy transitions. The ALMA pathfinding experiment (APEX) telescope can be used to observe higher energy transitions of CN, CS, CO, SiO and HCO^+ towards the massive star forming regions in the southern hemisphere.

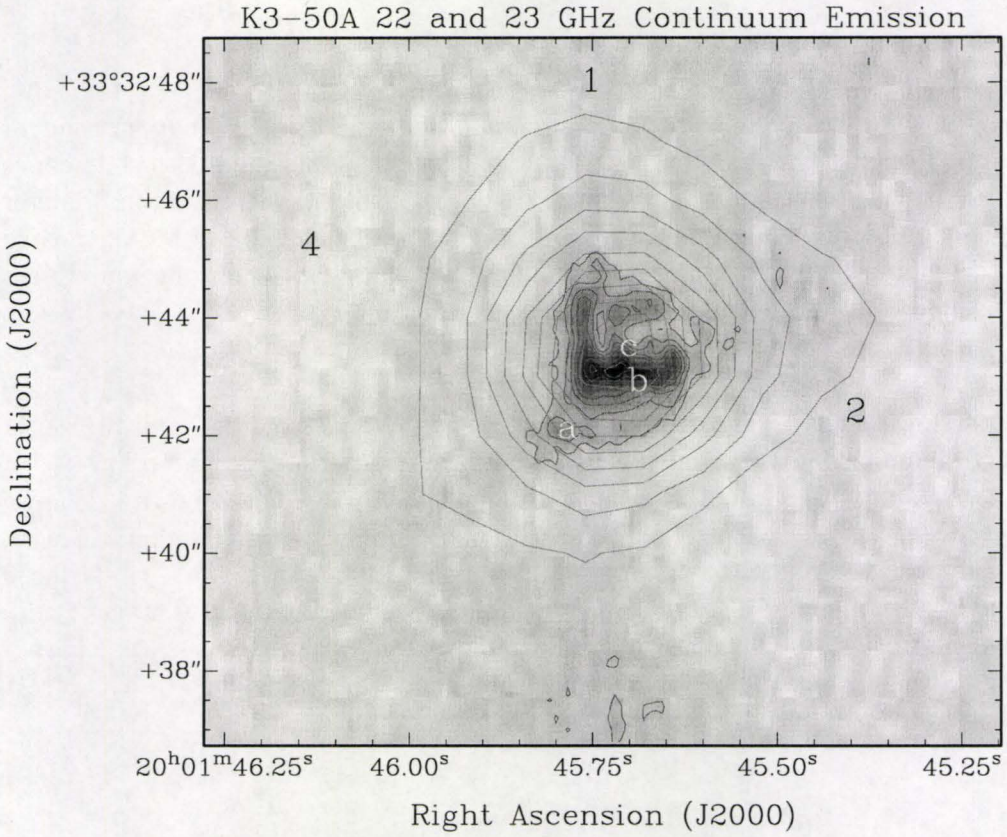

Figure 6.1: The black contours (and grayscale) represent the 22 GHz continuum emission observed at a resolution of 0.3″, while the gray contours represent the 23 GHz continuum emission observed at a resolution of 3″. The letters represent the three massive stars identified in the mid-infrared by Okamoto et al. (2003), while the numbers represent the features described in Howard et al. (1997), where the region labeled 2 was a strong source of SiO emission.

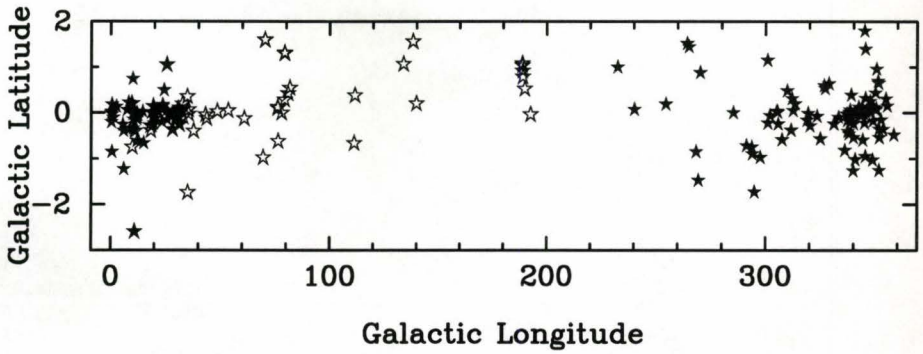

Figure 6.2: Massive star forming regions observable from the northern hemisphere (open stars) have been well studied since most submillimeter telescopes are currently in the northern hemisphere. Now that there is a submillimeter telescope in the southern hemisphere, we can begin to explore the chemistry and dynamics of a much larger set of sources, thus improving our constraints on the formation mechanisms of massive stars.

Using the IRAS color criteria described in Wood & Churchwell (1989), a large number of HII regions observable in the northern hemisphere have been well studied, but those in the southern hemisphere have not. Figure 6.2 shows the distribution of IRAS sources with colors indicative of HII regions, with those observable in the northern hemisphere shown as open stars, while those only observable in the southern hemisphere are labeled with filled stars. There appear to be a lot of massive star forming regions that are as yet uncharacterized in the submillimeter, and are thus good objects against which to test theories of massive star formation.

Bibliography

Ables, J. G. 1974, A&AS, 15, 383

Andre, P., Ward-Thompson, D., & Barsony, M. 1993, ApJ, 406, 122

Andre, P., Ward-Thompson, D., & Barsony, M. 2000, Protostars and Planets IV, 59

Arce, H. G., Shepherd, D., Gueth, F., Lee, C.-F., Bachiller, R., Rosen, A., &Beuther, H. 2007, Protostars and Planets V, 245

Bachiller, R. 1996, ARAA, 34, 111

Bally, J., & Reipurth, B. 2002, Revista Mexicana de Astronomia y Astrofisica Conference Series, 13, 1

Banerjee, R., & Pudritz, R. E. 2007, ApJ, 660, 479

Basu, S., Johnstone, D., & Martin, P. G. 1999, ApJ, 516, 843

Bate, M. R., & Bonnell, I. A. 2005,MNRAS, 356, 1201

Behrend, R., & Maeder, A. 2001, A&A, 373, 190

Beltrán, M. T., Cesaroni, R., Neri, R., Codella, C., Furuya, R. S., Testi, L., & Olmi, L. 2004, ApJL, 601, L187

Beltrán, M. T., Cesaroni, R., Codella, C., Testi, L., Furuya, R. S., & Olmi, L. 2006, Nature, 443, 427

Bergin, E. A., Neufeld, D. A., & Melnick, G. J. 1998, ApJ, 499, 777

Beuther, H., & Shepherd, D. 2005, Cores to Clusters: Star Formation with Next Generation Telescopes, 105

Beuther, H., & Walsh, A. J. 2008, ApJL, 673, L55

Beuther, H., Schilke, P., Sridharan, T. K., Menten, K. M., Walmsley, C. M., & Wyrowski, F. 2002, A&A, 383, 892

Beuther, H., et al. 2004, ApJL, 616, L23

Beuther, H., Schilke, P., & Gueth, F. 2004, ApJ, 608, 330

Beuther, H., Sridharan, T. K., & Saito, M. 2005, ApJL, 634, L185

Beuther, H., Churchwell, E. B., McKee, C. F., & Tan, J. C. 2007, Protostars and Planets V, 165

Bonnell, I. A., Bate, M. R., & Vine, S. G. 2003, MNRAS, 343, 413

Bonnell, I. A., Bate, M. R., & Zinnecker, H. 1998, MNRAS, 298, 93

Bonnell, I. A., Bate, M. R., Clarke, C. J., & Pringle, J. E. 1997, MNRAS, 285, 201

Cabrit, S., & Bertout, C. 1986, ApJ, 307, 313

Canto, J., Tenorio-Tagle, G., & Rozyczka, M. 1988, A&A, 192, 287

Caselli, P., Hartquist, T. W., & Havnes, O. 1997, A&A, 322, 296

Castor, J., McCray, R., & Weaver, R. 1975, ApJL, 200, L107

Cesaroni, R., Neri, R., Olmi, L., Testi, L., Walmsley, C. M., & Hofner, P. 2005, A&A, 434, 1039

Chandler, C. J., Brogan, C. L., Shirley, Y. L., & Loinard, L. 2005, ApJ, 632, 371

Charnley, S. B. 1997, ApJ, 481, 396

Chernin, L. M., & Masson, C. R. 1991, ApJL, 382, L93

Chini, R., Hoffmeister, V., Kimeswenger, S., Nielbock, M., Nürnberger, D., Schmidtobreick, L., & Sterzik, M. 2004, Nature, 429, 155

Chiosi, C., Bertelli, G., & Bressan, A. 1992, ARAA, 30, 235

Choi, M., Evans, N. J., II, & Jaffe, D. T. 1993, ApJ, 417, 624

Churchwell, E., Walmsley, C. M., & Cesaroni, R. 1990, A&AS, 83, 119

Cornwell, T. J. 1988, A&A, 202, 316

Cox, M. J., Scott, P. F., Russell, A. P. G., & Andersson, M. 1987, MNRAS, 226, 703

Davis, C. J., Moriarty-Schieven, G., Eislöffel, J., Hoare, M. G., & Ray, T. P. 1998, AJ, 115, 1118

De Buizer, J. M., Radomski, J. T., Telesco, C. M., & Piña, R. K. 2003, ApJ, 598, 1127

De Buizer, J. M., Osorio, M., & Calvet, N. 2005, ApJ, 635, 452

Depree, C. G., Goss, W. M., Palmer, P., & Rubin, R. H. 1994, ApJ, 428, 670

De Vries, C. H., & Myers, P. C. 2005, ApJ, 620, 800

Di Francesco, J., Myers, P. C., Wilner, D. J., Ohashi, N., & Mardones, D. 2001, ApJ, 562, 770

Di Francesco, J., Johnstone, D., Kirk, H., MacKenzie, T., & Ledwosinska, E. 2008, ArXiv e-prints, 801, arXiv:0801.2595

Dobbs, C. L., Bonnell, I. A., & Clark, P. C. 2005, MNRAS, 360, 2

Doty, S. D., van Dishoeck, E. F., van der Tak, F. F. S., & Boonman, A. M. S. 2002, A&A, 389, 446

Dutrey, A., Guilloteau, S., & Guelin, M. 1997, A&A, 317, L55

Dyson, J. E., & Williams, D. A. 1997, The physics of the interstellar medium. Edition: 2nd ed. Publisher: Bristol: Institute of Physics Publishing, 1997. Edited by J. E. Dyson and D. A. Williams. Series: The graduate series in astronomy. ISBN: 0750303069,

Edgar, R., & Clarke, C. 2003, MNRAS, 338, 962

Egan, M. P., Shipman, R. F., Price, S. D., Carey, S. J., Clark, F. O., & Cohen, M. 1998, ApJL, 494, L199

Eisloffel, J., Mundt, R., Ray, T. P., & Rodriguez, L. F. 2000, Protostars and Planets IV, 815

Eisner, J. A., Plambeck, R. L., Carpenter, J. M., Corder, S. A., Qi, C., & Wilner, D. 2008, ArXiv e-prints, 803, arXiv:0803.3217

Evans, N. J., II 1999, ARAA, 37, 311

Evans, N. J., II, et al. 1981, ApJ, 244, 115

Evans, N. J., Shirley, Y. L., Mueller, K. E., & Knez, C. 2002, Hot Star Workshop III: The Earliest Phases of Massive Star Birth, 267, 17

Field, G. B., Goldsmith, D. W., & Habing, H. J. 1969, ApJL, 155, L149

Fontani, F., Cesaroni, R., Caselli, P., & Olmi, L. 2002, A&A, 389, 603

Fuller, G. A., Williams, S. J., & Sridharan, T. K. 2005, A&A, 442, 949

Garay, G., & Lizano, S. 1999, PASP, 111, 1049

Gibb, A. G., Wyrowski, F., & Mundy, L. G. 2004, ApJ, 616, 301

Girart, J. M., Ho, P. T. P., Rudolph, A. L., Estalella, R., Wilner, D. J., & Chernin, L. M. 1999, ApJ, 522, 921

Goldsmith, P. F., Li, D., & Krčo, M. 2007, ApJ, 654, 273

Gregersen, E. M., Evans, N. J., II, Zhou, S., & Choi, M. 1997, ApJ, 484, 256

Hanson, M. M., Luhman, K. L., & Rieke, G. H. 2002, ApJS, 138, 35

Harju, J., Lehtinen, K., Booth, R. S., & Zinchenko, I. 1998, A&AS, 132, 211

Hartmann, L., & MacGregor, K. B. 1982, ApJ, 259, 180

Hatchell, J., Fuller, G. A., & Ladd, E. F. 1999, A&A, 344, 687

Henning, T., Michel, B., & Stognienko, R. 1995, P&SS, 43, 1333

Hildebrand, R. H. 1983, QJRAS, 24, 267

Hofner, P., Wyrowski, F., Walmsley, C. M., & Churchwell, E. 2000, ApJ, 536, 393

Hogerheijde, M. R., van Dishoeck, E. F., Blake, G. A., & van Langevelde, H. J. 1997, ApJ, 489, 293

Hollenbach, D. J., & Tielens, A. G. G. M. 1997, ARAA, 35, 179

Howard, E. M., Koerner, D. W., & Pipher, J. L. 1997, ApJ, 477, 738

Hunter, T. R., Brogan, C. L., Indebetouw, R., & Cyganowski, C. J. 2008, ArXiv e-prints, 803, arXiv:0803.0587

Hunter, T. R. 1997, Ph.D. Thesis,

Iben, I. J. 1967, ARAA, 5, 571

Jaschek, C., & Valbousquet, A. 1993, A&A, 275, 472

Jørgensen, J. K., Schöier, F. L., & van Dishoeck, E. F. 2004, A&A, 416, 603

Jiménez-Serra, I., Martín-Pintado, J., Viti, S., Martín, S., Rodríguez-Franco, A., Faure, A., & Tennyson, J. 2006, ApJL, 650, L135

Kameya, O., Hasegawa, T. I., Hirano, N., Takakubo, K., & Seki, M. 1989, ApJ, 339, 222

Keane, J. V., Boonman, A. M. S., Tielens, A. G. G. M., & van Dishoeck, E. F. 2001, A&A, 376, L5

Keto, E. R. 1991, ApJ, 371, 163

Keto, E., & Wood, K. 2006, ApJ, 637, 850

Keto, E. 2003, ApJ, 599, 1196

Keto, E. 2007, ApJ, 666, 976

Keto, E., Zhang, Q., & Kurtz, S. 2008, ApJ, 672, 423

Keto, E., & Klaassen, P. 2008, ApJL, 678, L109

Keto, E., & Caselli, P. 2008, ArXiv e-prints, 804, arXiv:0804.0822

Klaassen, P. D., & Wilson, C. D. 2007, ApJ, 663, 1092

Klaassen, P. D., & Wilson, C. D. 2008, ApJin press

Klaassen, P. D., & Wilson, C. D. 2008, Astronomical Society of the Pacific Conference Series, 387, 170

Klaassen, P. D., Wilson, C. D., Keto, E.R., & Zhang, Q., 2008, in prep

Klaassen, P. D., Wilson, C. D., Keto, E.R., & Zhang, Q., 2008, in prep

Klaassen, P. D., Plume, R., Ouyed, R., von Benda-Beckmann, A. M., & Di Francesco, J. 2006, ApJ, 648, 1079

Klaassen, P. D., Plume, R., Gibson, S. J., Taylor, A. R., & Brunt, C. M. 2005, ApJ, 631, 1001

Konigl, A. 1982, ApJ, 261, 115

Kraus, S., et al. 2006, A&A, 455, 521

Kroupa, P. 2001, MNRAS, 322, 231

Krumholz, M. R., McKee, C. F., & Klein, R. I. 2005, ApJL, 618, L33

Krumholz, M. R., McKee, C. F., & Klein, R. I. 2005, Nature, 438, 332

Krumholz, M. R., & Bonnell, I. A. 2007, ArXiv e-prints, 712, arXiv:0712.0828

Kumar, M. S. N., Fernandes, A. J. L., Hunter, T. R., Davis, C. J., & Kurtz, S. 2003, A&A, 412, 175

Kurtz, S., Churchwell, E., & Wood, D. O. S. 1994, ApJS, 91, 659

Kurtz, S., Cesaroni, R., Churchwell, E., Hofner, P., & Walmsley, C. M. 2000, Protostars and Planets IV, 299

Lada, C. J. 1999, NATO ASIC Proc. 540: The Origin of Stars and Planetary Systems, 143

Lada, C. J. 1985, ARAA, 23, 267

Larson, R. B. 1972, MNRAS, 156, 437

Lee, J.-E., Di Francesco,J., Bourke, T. L., Evans, N. J., II, & Wu, J. 2007, ApJ, 671, 1748

Lee, C.-F., Mundy, L. G., Reipurth, B., Ostriker, E. C., & Stone, J. M. 2000, ApJ, 542, 925

Lizano, S., & Giovanardi, C. 1995, ApJ, 447, 742

Loinard, L., Torres, R. M., Mioduszewski, A. J., Rodríguez, L. F., González-Lópezlira, R. A., Lachaume, R., Vázquez, V., & González, E. 2007, ApJ, 671, 546

Mamajek, E. E. 2008, Astronomische Nachrichten, 329, 10

Mardones, D., Myers, P. C., Tafalla, M., Wilner, D. J., Bachiller, R.,& Garay, G. 1997, ApJ, 489, 719

Masson, C. R., & Chernin, L. M. 1993, ApJ, 414, 230

Matzner, C. D., & McKee, C. F. 1999, Star Formation 1999, Proceedings of Star Formation 1999, held in Nagoya, Japan, June 21 - 25, 1999, Editor: T. Nakamoto, Nobeyama Radio Observatory, p. 353-357, 353

McKee, C. F., & Ostriker, E. C. 2007, ARAA, 45, 565

McKee, C. F., & Tan, J. C. 2003, ApJ, 585, 850

McKee, C. F., & Tan, J. C. 2002, Nature, 416, 59

Megeath, S. T., Wilson, T. L., & Corbin, M. R. 2005, ApJL, 622, L141

Mehringer, D. M. 1994, ApJS, 91, 713

Menten, K. M., Reid, M. J., Forbrich, J., & Brunthaler, A. 2007, A&A, 474, 515

Muzerolle, J., Calvet, N., Hartmann, L., & D'Alessio, P. 2003, ApJL, 597, L149

Myers, P. C., Mardones, D., Tafalla, M., Williams, J. P., & Wilner, D. J. 1996, ApJL, 465, L133

Nakamura, F. 2000, ApJ, 543, 291

Narayan, R., & Nityananda, R. 1986, ARAA, 24, 127

Okamoto, Y. K., Kataza, H., Yamashita, T., Miyata, T., Sako, S., Takubo, S., Honda, M., & Onaka, T. 2003, ApJ, 584, 368

Olmi, L., Cesaroni, R., & Walmsley, C. M. 1996, A&A, 307, 599

Pascucci, I., Apai, D., Henning, T., Stecklum, B., & Brandl, B. 2004, A&A, 426, 523

Pelletier, G., & Pudritz, R. E. 1992, ApJ, 394, 117

Penston, M. V. 1969, MNRAS,145, 457

Pillai, T., Wyrowski, F., Carey, S. J., & Menten, K. M. 2006, A&A, 450, 569

Pineau des Forets, G., Flower, D. R., & Chieze, J.-P. 1997, Herbig-Haro Flows and the Birth of Stars, 182, 199

Plume, R., Jaffe, D. T., & Evans, N. J., II 1992, ApJS, 78, 505

Plume, R., Jaffe, D. T., Evans, N. J., II, Martin-Pintado, J., & Gomez-Gonzalez, J. 1997, ApJ, 476, 730

Pratap, P., Batrla, W., & Snyder, L. E. 1990, ApJ, 351, 530

Pudritz, R. E., & Norman, C. A. 1986, ApJ, 301, 571

Pudritz, R. E., Ouyed, R., Fendt, C., & Brandenburg, A. 2007, Protostars and Planets V, 277

Purcell, C. R., et al. 2006, MNRAS, 367, 553

Rawlings, J. M. C., Redman, M. P., Keto, E., & Williams, D. A. 2004, MNRAS, 351, 1054

Ray, T., Dougados, C., Bacciotti, F., Eislöffel, J., & Chrysostomou, A. 2007, Protostars and Planets V, 231

Rholfs, K., Wilson, T. L. 2004, Tools of Radio Astronomy (4th ed; Berlin; Springer)

Riddick, F. C., Roche, P. F., & Lucas, P. W. 2007, MNRAS, 381, 1077

Robitaille, T. P. 2008, Astronomical Society of the Pacific Conference Series, 387, 290

Rudolph, A., Welch, W. J., Palmer, P., & Dubrulle, B. 1990, ApJ, 363, 528

Schilke, P., Walmsley, C. M., Pineau des Forets, G., & Flower, D. R. 1997, A&A, 321, 293

Schilke, P., Pineau des Forêts, G., Walmsley, C. M., & Martín-Pintado, J. 2001, A&A, 372, 291

Sewilo, M., Churchwell, E., Kurtz, S., Goss, W. M., & Hofner, P. 2004, ApJ, 605, 285

Shepherd, D. S., & Churchwell, E. 1996, ApJ, 472, 225

Shepherd, D. 2003, Galactic Star Formation Across the Stellar Mass Spectrum, 287, 333

Shepherd, D. S., Kurtz, S. E., & Testi, L. 2004, ApJ, 601, 952

Shepherd, D. 2005, Massive Star Birth: A Crossroads of Astrophysics, 227, 237

Shirley, Y. L., Evans, N. J., II, Rawlings, J. M. C., & Gregersen, E. M. 2000, ApJS, 131, 249

Shirley, Y. L., Evans, N. J., II, Young, K. E., Knez, C., & Jaffe, D. T. 2003, ApJS, 149, 375

Shirley, Y. L. 2007, Molecules in Space and Laboratory,

Shu, F. H. 1977, ApJ, 214, 488

Shu, F. H., Adams, F. C., & Lizano, S. 1987, ARAA, 25, 23

Shu, F., Najita, J., Ostriker, E., Wilkin, F., Ruden, S., & Lizano, S. 1994, ApJ, 429, 781

Snell, R. L., Loren, R. B., & Plambeck, R. L. 1980, ApJL, 239, L17

Sollins, P. K., et al. 2004a, ApJL, 616, L35

Sollins, P. K., Zhang, Q., & Ho, P. T. P. 2004b, ApJ, 606, 943

Sollins, P. K., Zhang, Q., Keto, E., & Ho, P. T. P. 2005, ApJL, 624, L49

Spergel, D. N., et al. 2007, ApJS, 170, 377

Spitzer, L. 1998, Physical Processes in the Interstellar Medium, by Lyman Spitzer, pp. 335. ISBN 0-471-29335-0. Wiley-VCH , May 1998.,

Sridharan, T. K., Beuther, H., Schilke, P., Menten, K. M., & Wyrowski, F. 2002, ApJ, 566, 931

Stahler, S. W., & Palla, F. 2005, The Formation of Stars, by Steven W. Stahler, Francesco Palla, pp. 865. ISBN 3-527-40559-3. Wiley-VCH , January 2005.,

Stahler, S. W., Palla, F., & Ho, P. T. P. 2000, Protostars and Planets IV, 327

Stanimirovic, S. 2002, Single-Dish Radio Astronomy: Techniques and Applications, 278, 375

Terebey, S., Shu, F. H., & Cassen, P. 1984, ApJ, 286, 529

Thompson, A. R., Moran, J. M., & Swenson, G. W. 1986, New York, Wiley-Interscience, 1986, 554 p.,

Tielens, A. G. G. M. 2005, The Physics and Chemistry of the Interstellar Medium (Cambridge University Press)

Townes, C. H., & Schawlow, A. L. 1975, Microwave Spectroscopy (Dover Publications, Inc.)

van der Tak, F. F. S. 2005, Massive Star Birth: A Crossroads of Astrophysics, 227, 70

van Dishoeck, E. F., & Blake, G. A. 1998, ARAA, 36, 317

Viti, S., & Williams, D. A. 1999, MNRAS, 310, 517

Viti, S., & Williams, D. A. 1999, MNRAS, 305, 755

Vogel, S. N., Wright, M. C. H., Plambeck, R. L., & Welch, W. J. 1984, ApJ, 283, 655

Wang, Y., Jaffe, D. T., Evans, N. J., II, Hayashi, M., Tatematsu, K., & Zhou, S. 1993, ApJ, 419, 707

Ward-Thompson, D., André, P., & Kirk, J. M. 2002, MNRAS, 329, 257

Wilson, T. L., & Rood, R. 1994, ARAA, 32, 191

Wolfire, M. G., & Cassinelli, J. P. 1987, ApJ, 319, 850

Wolfire, M. G., & Koenigl, A. 1993, ApJ, 415, 204

Wood, D. O. S., & Churchwell, E. 1989, ApJS, 69, 831

Wu, Y., Wei, Y., Zhao, M., Shi, Y., Yu, W., Qin, S., & Huang, M. 2004, A&A, 426, 503

Yorke, H. W. 2002, ASP Conf. Ser. 267: Hot Star Workshop III: The Earliest Phases of Massive Star Birth, 267, 165

Zhang, Q., & Ho, P. T. P. 1997, ApJ, 488, 241

Zhang, Q., Ho, P. T. P., & Ohashi, N. 1998, ApJ, 494, 636

Zinnecker, H., & Yorke, H. W. 2007, ARA&A, 45, 481

Appendix A

Glossary

Arcsecond ($''$) A unit of angular separation. A degree ($^\circ$) on the sky can be subdivided into 60 arcminutes ($'$), each of which is then subdivided into 60 arcseconds ($''$).
($1'' = 4.85\times10^{-6}$ rad)

Astronomical Unit (AU) The mean distance between the Sun and Earth.
(1 AU = 1.5×10^{13} cm)

Column Density (N) The amount of material along the line of sight within a resolution element. Column density generally has units of cm^{-2}, and can be expressed in terms of the more familiar volume density as $n = \int N ds$ where n is the volume density, and ds is a length element (along the line of sight).

Declination (DEC) Using the equatorial coordinate system, DEC is the measure of how far north or south an object is from the Celestial Equator. It is perpendicular to Right Ascension.

Galactic Latitude (b) Using the galactic coordinate system, it is a measure of how far north or south an object is from the galactic plane.

Galactic Longitude (ℓ) Using the galactic coordinate system, it is a measure of the angular distance from the line connecting the Sun and the Galactic center along the galactic plane.

GMC Giant Molecular Cloud

Hertzprung-Russell (HR) Diagram A plot of stellar color (or surface temperature) vs. luminosity (or absolute magnitude). As a star evolves towards, through, and beyond core hydrogen burning, its position on an HR diagram changes

HII region A region of hot (ionized) material around a forming, or newly formed massive star.

IMF Initial Mass Function

IRDC Infrared Dark Cloud

ISM Interstellar Medium

Jansky (Jy) A unit flux measure used in Radio Astronomy.
($1\ \mathrm{Jy} = 1 \times 10^{-23}\ \mathrm{erg\ sec^{-1}\ cm^{-2}\ Hz^{-1}}$)

JCMT James Clerk Maxwell Telescope

LTE Local Thermodynamic Equilibrium

Main Beam Temperature (T_{MB}) Temperature scale in which single dish telescope intensities are measured once the data has been corrected for main beam efficiency.

Main Sequence The stage of a stellar lifetime in which it is undergoing stable core hydrogen burning. This is the longest stage of a stars lifetime, and stars of all masses form a strip of points along a fairly diagonal line through the middle of the HR diagram.

Optical Depth A measure of the opacity of a gas cloud. Having an optical depth (τ) of unity means that the cloud is opaque. Values less than one mean that the cloud is somewhat translucent, and we can see deeper into the cloud.

Parsec Parallax Second; The distance to an object who's paralactic shift due to the Earth's motion about the sun is 1 arcsecond ($''$).
($1\ \mathrm{pc} = 3.086 \times 10^{18}\ \mathrm{cm}$)

PDR Photo dissociation Region

PV Diagram A slice through a data cube in which there is one spatial axis (offset from some central position along a given line) and one velocity axis.

Right Ascension (RA) Using the equatorial coordinate system, RA is the measure of the distance along the celestial equator (a projection of the Earth's equator onto the Celestial Sphere) from the intersection of the ecliptic (the Sun's apparent path through the sky over the course of a year) and the celestial equator (this point is known as the Vernal Equinox). It is perpendicular to Declination.

SMA Submillimeter Array

Solar Mass ($M_\odot$) A unit mass often used in astronomy. It is the mass of the Sun.
($1\ M_\odot = 1.99\times10^{33}$ g)

Solar Luminosity ($L_\odot$) A unit of power often used in Astronomy. It is the total energy output of the Sun per unit time.
($1\ L_\odot = 3.839\times10^{33}$ erg s^{-1})

Spectral Energy Distribution (SED) Plank Black Body function used to determine the evolutionary stage of a low mass protostar. The slope of the SED between 2 and 20 μm changes as a low mass protostar heats up and ages.

ZAMS Zero Age Main Sequence; When a protostar (or pre-main sequence star) begins stable core hydrogen fusion, and arrives on the main sequence.

Appendix B

Column Density Derivations

B.1 Determining the Column Density from an Observed Linear Molecule in the ISM

The equation of radiative transfer is

$$\frac{dI_\nu}{ds} = -\kappa_\nu I_\nu + j_\nu \tag{B.1}$$

where I_ν is the intensity at the given frequency (ν), κ_ν is the absorption coefficient at ν, j_ν is the emission coefficient at ν and ds is a line of sight distance element. Expressing the opacity (τ) as the integral of the absorption along the line of sight ($\tau = \int \kappa_\nu ds \rightarrow d\tau = \kappa_\nu ds$), then this can be re-expressed as

$$\frac{dI_\nu}{d\tau} = -I_\nu + \frac{j_\nu}{\kappa_\nu} \tag{B.2}$$

$$I_\nu = I_0 e^{-\tau} + \int_o^{\tau_\nu} (j_\nu/\kappa_\nu) e^{-\tau} d\tau \tag{B.3}$$

where j_ν/κ_ν is the source function (S_ν), and I_0 is the background intensity (which can be 'chopped' out of the observation, and can safely be dropped from this equation). Thus,

$$I_\nu = \int S_\nu e^{-\tau} d\tau \tag{B.4}$$

In local thermodynamic equilibrium (LTE), I_ν and S_ν are both equivalent to blackbodies (of the object emitting, and the ambient medium). They can thus both be expressed as Planck functions ($B_\nu(T)$) which has the general form

$$B_\nu(T) = \frac{2h\nu^2}{c^3}\frac{1}{e^{E/kT}-1}, \quad \text{where} \quad B(T) = \int B_\nu(T)d\nu \tag{B.5}$$

Equation B.4 can then be expressed as

$$\begin{aligned} B_\nu(T_B) &= \int B_\nu(T_K)e^{-\tau}d\tau & \text{(B.6)} \\ &= B_\nu(T_K)(1-e^{-\tau}) & \text{(B.7)} \end{aligned}$$

where T_B is the brightness temperature of the source, and T_K is the ambient temperature of the region. In the optically thin limit ($\tau < 1$), $(1-e^{-\tau})$ can be simplified (via Taylor expansion) to simply τ, resulting in

$$\begin{aligned} B_\nu(T_B) &= B_\nu(T_K)\tau & \text{(B.8)} \\ &= B_\nu(T_K)\int \kappa_\nu ds \quad \text{since} \quad \tau = \int \kappa_\nu ds & \text{(B.9)} \end{aligned}$$

The absorption coefficient can be determined by considering the total energy absorbed ($\kappa_\nu I_\nu d\nu$). This is the difference between the stimulated absorption into and stimulated emission out of this transition in the region (see Spitzer p 35).

$$\kappa_\nu = \frac{h\nu_{u\ell}}{c}(n_\ell B_{\ell u} - n_u B_{u\ell})\phi(\nu) \tag{B.10}$$

where n_i is the density of molecules in level i, B_ij is the Einstein B coefficient (either up or down) and $\phi(\nu)$ is a normalized constant ($\int \phi(\nu)d\nu = 1$)introduced to describe the line shape and width. The two Einstein coefficients are related through

$$g_u B_{u\ell} = g_\ell B_{\ell u} \rightarrow B_{\ell u} = \frac{g_u}{g_\ell}B_{u\ell} \tag{B.11}$$

In LTE, the ratio of the populations in two levels can be expressed as

$$\frac{n_u}{n_\ell} = \frac{g_u}{g_l}e^{-E_{u\ell}/kT} \tag{B.12}$$

So, Equation B.10 can be re-expressed as

$$\begin{aligned} \kappa_\nu &= \frac{h\nu_{u\ell}}{c}\left[\left(\frac{n_u g_\ell}{g_u}e^{E_{u\ell}/kT}\right)\left(\frac{g_u}{g_\ell}B_{u\ell}\right) - n_u B_{u\ell}\right]\phi(\nu) & \text{(B.13)} \\ &= \frac{h\nu_{u\ell}}{c}n_u B_{u\ell}\left(e^{E_{u\ell}/kT}-1\right)\phi(\nu) & \text{(B.14)} \end{aligned}$$

The Einstein B coefficient is related to the Einstein A coefficient via

$$A_{u\ell} = \frac{8\pi h\nu_{u\ell}^3}{c^3} B_{u\ell} \rightarrow B_{u\ell} = \frac{c^3 A_{u\ell}}{8\pi h\nu_{u\ell}^3} \tag{B.15}$$

thus

$$\kappa_\nu = \frac{c^2}{8\pi\nu_{u\ell}^2} n_u A_{u\ell} \left(e^{E_{u\ell}/kT} - 1\right) \phi(\nu) \tag{B.16}$$

This value for κ_ν can now be put back into Equation B.9

$$B_\nu(T_B) = \int B_\nu(T_K)\kappa_\nu ds \tag{B.17}$$

$$= \int B_\nu(T_K) \frac{c^2}{8\pi\nu_{u\ell}^2} n_u A_{u\ell} \left(e^{E_{u\ell}/kT} - 1\right) \phi(\nu) ds \tag{B.18}$$

Since $\int n_u ds = N_u$, this can be written in terms of column density. Then, integrating over the frequency range of the observed line,

$$\int B_\nu(T_B) d\nu = \frac{c^2}{8\pi\nu_{u\ell}^2} N_u A_{u\ell} \left(e^{E_{u\ell}/kT} - 1\right) \int \phi(\nu) B_\nu(T_K) d\nu \tag{B.19}$$

where $B_\nu(T_B)$ can be assumed to be in the Rayleigh-Jeans tail, and $B_\nu(T_K)$ is left as the general case as

$$\int B_\nu(T_B) d\nu = \frac{2k\nu_{u\ell}^2}{c^2} \int T_B d\nu \quad \text{and} \quad \int \phi(\nu) B_\nu(T_K) d\nu = \frac{2h\nu_{u\ell}^3}{c^2} \frac{1}{e^{E_{u\ell}/kT} - 1} \tag{B.20}$$

This gives

$$\frac{2k\nu_{u\ell}^2}{c^2} \int T_B d\nu = \frac{2h\nu_{u\ell}^3}{c^2} \frac{1}{e^{E_{u\ell}/kT} - 1} \left(\frac{c^2}{8\pi\nu_{u\ell}^2}\right) N_u A_{u\ell} \left(e^{E_{u\ell}/kT} - 1\right) \tag{B.21}$$

$$\int T_B d\nu = \frac{hc^2}{8\pi k\nu_{u\ell}} N_u A_{u\ell} \tag{B.22}$$

Rearranging for N_u, and changing the integration from over the frequency spread of the line to the velocity spread of the line ($d\nu = (\nu/c)dv$) gives the column density of molecules in a given stat u.

$$\boxed{N_u = \frac{8k\pi\nu_{u\ell}^2}{hc^3 A_{u\ell}} \int T_B dv} \tag{B.23}$$

B.2 Determining the Total Column Density for a Given Species in the ISM

The total column density of a given species (i.e. SiO, CO, HCO^+) can be expressed as the sum of the column densities in all levels.

$$N_{\rm TOT} = N_0 + N_1 + N_2 + N_3 + N_4 + ... \quad \text{(B.24)}$$

$$= N_0 \left(1 + \frac{N_1}{N_0} + \frac{N_2}{N_0} + \frac{N_3}{N_0} + ...\right) \quad \text{(B.25)}$$

Assuming the source is a blackbody, and that it is in local thermodynamic equilibrium (LTE) with its surroundings, the ratio between the populations in two levels can be expressed (similarly to equation B.12) as;

$$\frac{N_u}{N_\ell} = \frac{g_u}{g_\ell} \exp\left(\frac{-(E_u - E_\ell)}{kT}\right) \quad \text{(B.26)}$$

where $g_i = 2J + 1$ is the degeneracy of that level, T is the temperature of the thermal bath (the ambient temperature) and k is Boltzmann's constant, and E_i is the energy of that level *above the ground state.* The energy above the ground state can be expressed as $E_i = hB_eJ(J + 1)$ where B_e is the rotation constant (see Equation 14.12 in Rholfs & Wilson, 2004).

For the ground state, $g_0 = 2J + 1 = 1$ and the energy is $E_0 = hB_e(0)(0 + 1) = 0$. Thus, equation B.25 can be expressed as

$$N_{\rm TOT} = N_0 \left(1 + g_1 e^{-E_1/kT} + g_2 e^{-E_2/kT} + g_3 e^{-E_3/kT} + ...\right) \quad \text{(B.27)}$$

Since only states above the ground state can have emission lines, we cannot directly observe N_0. However, given equation B.26, we can re-express N_0 in terms of some higher (N_u) observable level.

$$\frac{N_u}{N_\ell} = \frac{g_u}{g_\ell} \exp\left(\frac{-(E_u - E_\ell)}{kT}\right) \rightarrow N_0 = \frac{N_u}{g_u e^{-E_u/kT}} \quad \text{(B.28)}$$

and

$$\boxed{N_{\rm TOT} = \frac{N_u}{g_u e^{-E_u/kT}} \left(\sum_{i=0}^{\infty} g_i e^{-E_i/kT}\right)} \quad \text{(B.29)}$$

where the last term on the right hand side is simply the partition function.

Appendix C

Combining SMA and JCMT Data Using MOSMEM

In general, visibilities observed with an interferometer are Fourier Transformed into the image plane as a 'dirty image'. The visibility function has the form

$$V'_{\rm int}(u,v) = V(u,v) \times b_{\rm int}(u,v) \tag{C.1}$$

where $V'_{\rm int}(u,v)$ are the set of observed visibilities at points u and v, $V(u,v)$ are the true visibilities and $b_{\rm int}$ is a set of delta functions representing the various baselines (Stanimirovic, 2002). The resultant dirty image has the form

$$I^{\rm D}_{\rm int}(l,m) = I(l,m) * B_{\rm int}(l',m') \tag{C.2}$$

where $I^{\rm D}_{\rm int}(l,m)$ is the set of sky brightnesses at the positions l and m, $I(l,m)$ is the true sky brightness at that position, and $B_{\rm int}(l',m')$ is the dirty beam of the observations.

Similarly, the brightness distribution observed with a single dish telescope can be expressed in the form:

$$I^{\rm D}_{\rm SD}(l,m) = I(l,m) * B_{\rm SD}(l',m') \tag{C.3}$$

where, like in the inteferometer case, $I^{\rm D}_{\rm SD}$ is the observed sky brightness, and $B_{\rm SD}$ is the beam of the observations.

In each case, the observed source can be deconvolved from the observing beam ($I * B$ is a convolution of the source brightness and the beam) to produce an image of the source. For the interferometer only data presented in Chapter 4, this was done using the CLEAN algorithm. When combining datasets, such as the data from an interferometer and a single dish telescope (like the data presented in Chapter 5), there are a number of techniques which can be employed to deconvolve the observed source from the observing beams and combine the datasets.

In the image plane, either linear or non-linear image combination techniques can be used. Generally, linear image combintion techniques (such as the MIRIAD task IMMERGE) are best suited to datasets in which the majority of the source brightness is concentrated on small scales, while the non-linear techniques (such as the MIRIAD task MOSMEM) are better suited to source deconvolution where the majority of the brightness is in large scale structures.

MOSMEM, the image plane deconvolution task in MIRIAD, uses a maxium entropy method for joint deconvolution of multiple maps of the same region. That the task employs a joint deconvolution means that the two images are deconvolved simultaneously instead of separately and then added together. Here, the maps to be combined consist of an interferometer map for small scale structures, and a single dish map for large scale structures.

The term 'entropy' in this context refers to a variable that produces a positive image when maximized, and exists over a 'compressed range in pixel values' to ensure smoothness of the final image (Cornwell, 1988). Maximizing the entropy places the constraint that the jointly deconvolved image is as smooth (i.e. featureless) as possible given the observed data (Narayan & Nityananda, 1986). Maximizing the smoothness of the combined map minimizes the amount of information introduced by extrapolated visibilities (Ables, 1974).

Again using the notation of Stanimirovic (2002), the entropy, given by

$$\aleph = -\sum_i I_i \ln\left(\frac{I_i}{e}\right) \tag{C.4}$$

where I_i is the brightness of the ith pixel, is maximized while simultaneously doing a χ^2 fit to the deconvolution of both datasets, given by

$$\sum_i \{I^{\rm D}_{\rm int} - B_{\rm int} * I\}^2_i \;<\; N\sigma^2_{\rm int} \tag{C.5}$$

$$\sum_i \{I^{\rm D}_{\rm SD} - B_{\rm SD} * I\}^2_i \;<\; M\sigma^2_{\rm SD} \tag{C.6}$$

where $I^{\rm D}_{\rm int}$, $B_{\rm int}$, $I^{\rm D}_{\rm SD}$, and $B_{\rm SD}$ are defined as above, and $\sigma_{\rm int}$ and $\sigma_{\rm SD}$ are the rms noise in the image from the interferometer and single dish telescopes respectively. I is simultaneously solved for in equations C.4, C.5 and C.6.

In order to simultaneously solve these three equations, the flux scales of the two maps must match, as well as the spatial scales of the observations (the sizes of the pixels must be identical).

In order to match the spatial scales of the two maps, the JCMT data presented in Chapter 5 have been regridded to the resolution of the SMA data, using the SMA dirty image as a template. The beam information for the

SMA observations was created when the *uv* plane visbilities were transformed into the image plane, but there is no beam file created with the single dish image. Thus, we created one using the MIRIAD command IMGEN using the size of the JCMT primary beam (20.8″) and assuming that it is gaussian.

The SMA data presented here are expresed in units of Jy/beam, while the native flux units of the JCMT data is in K. Using the Jy/Beam → K conversions listed in Section 4.4, we were able to convert the JCMT data into units of Jy/beam after it was regridded to the resolution of the SMA data.

The MIRIAD script given below shows the steps required to bring the SMA data into the image plane from a set of visibilities which have had the continuum emission removed (using the UVLIN task), and how to prepare the JCMT map for joint deconvolution with the SMA dirty image.

Finally, once the two beam files are present, the images are at the same resolution, and the flux scaling is comparable between the two datasets, the MOSMEM task is run. This provides clean components which must be restored back into the SMA dirty image using the MIRIAD task RESTOR, as is done with individual maps which have been cleaned.

Using `rmsfac` values that were approximately twice those estimated from the JCMT data, we find that greater than 90% of the individual image planes converged to solutions using MOSMEM. `rmsfac` tells the MOSMEM task how well to trust the theoretical noise limits in the header of the two datasets when minimizing equations C.5 and C.6.

Below, we show the commands used to create the combined map for NGC 7538.

```
#subtract continuum from SMA dataset
uvlin   vis=n7538.CO.reduced out=n7538.sub  \
        line=velocity,4500,-1000,0.53 \
        chans=-1600,-200,150,300 order=0

# invert, binned to the JCMT velocity resolution
invert  vis=n7538.sub map=n7538_sma.im \
        beam=n7538_sma.beam \
        imsize=512,512 line=velocity,300,-133.68,0.63497 \
        cell=0.25,0.25 robust=0.5

# put rest frequency info into JCMT header
puthd  in=n7538_jcmt/restfreq value=230.5379944
velsw  in=n7538_jcmt axis=radio

#change the JCMT data to be measured in km/s from frequency
puthd in=n7538_jcmt/ctype3 value=VELO-LSR
```

```
# convert from Ta* to Jy/Beam  Ta*/Jy = 15.6/eta_ap
# (eta_ap = 0.59 according to JCMT website)
maths  exp="<n7538_jcmt>*26.44" out=n7538_jcmt_jy
puthd  in=n7538_jcmt_jy/bunit value=JY/BEAM

# give size & postion angle of JCMT beam
puthd  in=n7538_jcmt_jy/bmaj  value=1.008412457E-04
puthd  in=n7538_jcmt_jy/bmin  value=1.008412457E-04
puthd  in=n7538_jcmt_jy/bpa  value=0.000000000E+00

# get theoretical and real rms values from SMA header & imlist
gethd  in=n7538_sma.im/rms
imstat in=n7538_sma.im region='abspix,box(1,1,128,128)'
# theoretical = 0.03142072, real = 0.106 (rmsfac=3.3736)

# Create JCMT beam file
imgen   in=n7538_sma.beam out=n7538_jcmt.beam \
        factor=0 object=gaussian spar=1,0,0,20.8,20.8,0
#spar -> source parameters, in order of:
#amplitude, xoffset, yoffset, bmaj,bmin,pa


# change the pixel resolution of the JCMT data to that of the SMA
regrid  in=n7538_jcmt_jy \
        out=n7538_jcmt_regrid \
        axes=1,2,3 tin=n7538_sma.im

# correct for JCMT main beam efficiency
maths  exp="<n7538_jcmt_regrid>/0.69" out=n7538_jcmt_regrid_mb

# the rms value (acording to splat) is 0.097 K (Ta* scale)
puthd   in=n7538_jcmt_regrid_mb/rms value=3.7169

mosmem  map=n7538_sma.im,n7538_jcmt_regrid_mb \
        beam=n7538_sma.beam,n7538_jcmt.beam \
        out=NGC7538_mosmem.model \
        rmsfac=3,2 niters=30

restor  map=n7538_sma.im beam=n7538_sma.beam \
        model=NGC7538_mosmem.model out=NGC7538_mosmem.rest
```

Appendix D

Deriving Outflow Kinematics

Below, we describe the procedure used for determining the mass, momentum, energy, luminosity and mass loss rates in the observed outflows.

Mass

1. Shift the rest frequency of the MOSMEM map to match the Vlsr of the source (by changing `CRVAL3` in the header)

2. Create a zeroth moment map over the required (and Vlsr corrected) velocity range (using `MOMENT`)

3. Determine the rms in that image in an emission free region (using `HISTO`)

4. Mask the zeroth moment map to be only within the half power beam of the SMA observations, and mask off the emission lower than 3 sigma (using `MATHS`)

5. Use IMLIST to determine the total flux in the masked zeroth moment map.

6. Determine the number of pixels with emission (from `IMSTAT`)

7. Determine the lower limits of the CO column density (since 12CO is probably optically thick and the integrated intensity map will be a lower limit to the real integrated intensity) using the equations given in Appendix B.

8. Divide by 1×10^{-4} to scale to the H_2 column density

9. From the number of pixels, and the distance to source (1 pixel=0.3x0.3"), determine the area over which the integrated intensity was determined

10. Multiply the derived H_2 column density by the area and mass of a hydrogen molecule to determine the mass of the gas emitting within that velocity range.

Momentum

1. Create a first moment map from the MOSMEMed emission map which has already been clipped to the half power beam of the SMA, making sure that `rngmsk=true` (using `MOMENT`)

2. Multiply the integrated intensity from the previously created zeroth moment map with the integrated intensity of the first moment map (using `MATHS`).

3. Determine the total flux in the velocity weighted integated intensity map (using `IMLIST`)

4. Multiply by the same scaling factor as the MASS map in order to determine the momentum in the outflow lobe. (mom1 = $[\sum$ (I*v)]/$[\sum$(I)] and mom0 = [I*km/s])

Energy

1. Since E=P^2/2M, divide the square of the momentum in the outflow lobe by 2 times the mass in the same lobe. No data input is required for the energy calculation.

Luminosity

1. Determine the kinematic age of the outflow, either from published sources, or estimating from the velocity of the gas in our CO observations and distance the outflow has travelled.

2. Divide the outflow energy by the age of the outflow, and scale to recognizable units (from J/yr)

Mass Loss Rate

1. Divide the derived mass by the age of the outflow